SUBSTRATE FABRICATION AND CHARACTERIZATION FOR PHOTOVOLTAICS AND BIOMATERIALS APPLICATIONS

By

Morgan L. Krim

Dissertation

Submitted to the Faculty of the

Graduate School of Vanderbilt University

In partial fulfillment of the requirements

For the degree of

DOCTOR OF PHILOSOPHY

In

Chemistry

May, 2010

Nashville, Tennessee

Approved:	Date:
Prof. David E. Cliffel	03/26/2010
Prof. Richard Haglund	03/26/2010
Prof. Sandra Rosenthal	03/26/2010
Prof Michael P. Stone	03/26/2010

To my wife, Mădălina, I could search the world for a million lifetimes and I would never find a better partner.

To my parents, Mead and Jerry, for believing in me endlessly, constantly encouraging me, and setting a cheerful example to live by.

And for my brood, Jerry Stirling Ciobanu Krim and Carl Fyodor Ciobanu Krim, Jaden Marie Sutherland, Maria Arvemia Wilburn Ciobanu, and Leslie Marcel Ciobanu Wilburn. The effortless course is not a satisfying path to stroll, always seek out opportunities to challenge yourself because those are the most gratifying trails to saunter. Performing to your best and failing is more rewarding than besting an undemanding challenge.

ACKNOWLEDGEMENTS

First, I have the utmost gratitude for my graduate advisor, Prof. David E. Cliffel, without his hard work and his dedication to interdisciplinary science I would never have had the opportunity for my projects. Even when the realities of life distracted, and detracted, from the science, he knew that the genuine prospect of accomplishment was present. I am grateful for the fact that he possesses incredible patience and kindness that allowed him to never entirely give up on me, without these attributes in Dave I would have never produced this dissertation.

I sincerely appreciate the time, criticisms and advice I was privileged to receive from the members of my Graduate Committee, Prof. Sandra J. Rosenthal, Prof. Michael P. Stone, and Prof. Richard Haglund. I would also like to thank Prof. David Wright for serving on my committee. He was also instrumental in recruiting me to this university and chemistry department.

I would also like to thank Prof. G. Kane Jennings and Prof. Bridget R. Rogers from the Department of Chemical Engineering at Vanderbilt University for allowing me to use their labs and equipment.

Discussions with Andrzej Balinski and S. Reese Harry produced some of very useful ideas for advances in my capillary electrophoresis research. Dr. Jeremy P. Wilburn illustrated for me the techniques required for the construction of ultramicroelectrodes. Dr. Aren Gerdon assisted with the synthesis of analytes for the capillary electrophoresis experiments. Dr. Yibin Zhang and I collaborated on the RSV project.

Dr. Madalina Ciobanu helped with devising the requirements that the LabVIEW SECM program needed to fulfill, worked with me on perfecting the Photosystem I extraction, and provided extensive help with editing and formatting.

I would like to thank the Vanderbilt Institute of Nanoscale Science and Engineering for supporting this work. This project was supported in part by the National Research Initiative of the USDA Cooperative State Research, Education and Extension Service, Grant number 2005-35603-15303. Also, acknowledgement of financial sustainment for the QCM project goes to: Core C of SERCEB supported by NIAID # U54-AI057157, NIGMS # R01 GM076479, and Vanderbilt Institute of Nanoscale Science and Engineering (VINSE).

Finally, I would like to mention Lonnie, Rich, Phil, Bubba, Terry and Kenny, the guys I played foosball with, and Harold Stirling Vanderbilt for duplicate bridge.

TABLE OF CONTENTS

PAGE

DEDICATION ……ii

ACKNOWLEDGEMENTS ……iii

LIST OF TABLES ……viii

LIST OF FIGURES ……ix

LIST OF ABBREVIATIONS ……xi

Chapter

I. INTRODUCTION ……1

1. Scanning Electrochemical Microscope……3
2. Atomic Force Microscope……7
3. Quartz Crystal Microbalance……9
4. Capillary Electrophoresis……11
5. References……13

II. SURFACE CHARACTERIZATION OF PLATINIZED PHOTOSYSTEM I ORIENTED AND BOUND TO A AU-MODIFIED SUBSTRATE……16

1. Introduction……16
2. Experimental……21
    - A. Materials……21
    - B. Extraction and Characterization of Photosystem I……22
    - C. Platinization of Photosystem I……22
    - D. Atomic Force Microscopy……24
    - E. X-ray Photoelectron Spectroscopy……24
3. Results and Discussion……25
4. Conclusions……30
5. References……31

III. IMMUNOSENSOR DEVELOPMENT FOR THE DETECTION OF RESPIRATORY SYNCYTIAL VIRUS ON THE QUARTZ CRYSTAL MICROBALANCE PLATFORM……34

1. Introduction……34

2. Materials and Methods………...39
   - A. Reagents………..39
   - B. Atomic Force Microscopy………………………...................39
   - C. Ellipsometry………...40
   - D. Quartz Crystal Microbalance……….................................40
   - E. Immunosensor for RSV Detection………….......................41
   - F. ELISA for RSV Detection…………….................................41

3. Results and Discussion……………………………….…....................43
4. Conclusions……...59
5. Supporting Information………..61
6. References……………………..…………………………………….62

IV. SCANNING ELECTROCHEMICAL MICROSCOPE SOFTWARE SUITE WITH REAL-TIME THREE-DIMENSIONAL GRAPHICS USING THE LabVIEW ENVIRONMENT……...66

1. Introduction………..66
2. User Interface…...71
3. Cyclic Voltametry and Approach Curve……….............................73
4. Real-Time Performance, Real-Time Image…….….........................76
5. Conclusions………...76
6. References………………………………………………………………77

V. CAPILLARY ELECTORPHORESIS FOUNTAIN PEN …….......................78

1. Introduction………...78
   - A. Surface Patterning…...78
   - B. Capillary Electrophoresis……………….……........................84
   - C. Capillary Electrophoresis Fountain Pen...........................86
   - D. Inks for CEFP……...88
2. Materials and Methods………...90
   - A. Chemicals……...90
   - B. Synthesis of Au Nanocrystals……………….....................91
   - C. Capillary Electrophoresis ………...91
3. Results and Discussion…………………………………….................92
   - A. Multipurpose Stage and Tip Holder…….............................92
   - B. Capillary Electrophoresis Fountain Pen………………….....93
   - C. Computer Interface ……...93
   - D. Capillary Electrophoresis Separation………….……………95
   - E. Monolayer Protected Cluster Deposition…………..……95

4. Conclusions………...96
5. References…………………………..…………………………………….98

APPENDIX……………………………………………………………...…………..101

VITAE…………………………………………………………………...…………..150

LIST OF TABLES

Table Page

III.1. Timeline and sequence for assembling and testing the QCM immunosensor for RSV detection…………………………..…42

III.2. The roughness and thickness of the layers required for the assembly and testing of the RSV immunosensor…………………...47

LIST OF FIGURES

Figure Page

I.1 Scanning electrochemical microscopy theory and approach curves…....….4

I.2 Scanning electrochemical microscope schematic…………………………......5

I.3 Schematic of the atomic force microscope……………………………………8

I.4 Capillary electrophoresis schematic…………………………………...…..11

II.1 Platinization of PSI……………………………………………………......…23

II.2 AFM images of the surfaces used and created in the steps for the photoreduction of Pt onto the active acceptor site of oriented PSI……..…26

II.3 AFM images for platinization on control surfaces…………………….…28

II.4 XPS of platinized PSI (Pt/PSI/HOC$_{11}$S/Au) and control surface (Pt/HOC$_{11}$S/Au)…………………………………………………………..……29

III.1 Immunosensor for RSV detection built on a QCM crystal……………..…44

III.2 QCM run displaying the steps required for the assembling and testing of the RSV immunosensor………………………...………………………...45

III.3 QCM run displaying the steps in the assembling and testing of a control of the RSV immunosensor………………………………………………......49

III.4 Mass change for control experiments compared to RSV binding………...53

III.5 Evaluation of the RSV immunosensor performance with infected cells…54

III.6 RSV concentration dependence experiments…………………………..…56

III.7 RSV detection in nasal wash samples from healthy patients.……….….…57

III.8 RSV detection in nasal wash samples prepared by adding a concentration gradient of RSV from cell culture……………………………………..…58

III.S.1 QCM run displaying the steps in the assembling and testing of a control of the RSV immunosensor, based on protein A……………….…………….…61

III.S.2 RSV detection in nasal wash samples prepared by adding a concentration gradient of RSV from a cell culture to a nasal wash sample from a healthy patient………………………………………………………………………..…62

IV.1 Scanning electrochemical microscope schematic showing the basic equipment requirements for electrochemical imaging using the described LabVIEW programs……………………………………...……………..…70

IV.2 The user interface of the SECM imaging program…………………….…71

IV.3 Flow chart for cyclic voltammogram program…………………………...…72

IV.4 CV and approach curve examples……………………………...……..…74

IV.5 A completed electrochemical micrograph of an interdigitated array.....…75

V.1 Schematic procedures for microcontact printing………………………………...82

V.2 Octadecanethiol dots applied with poly(dimethyl-siloxane) tip…………………83

V.3 Schematic of the system used for cell lysis……………………………………...85

V.4 Schematic of the capillary electrophoresis fountain pen………………………...87

V.5 Electropherograms of gold clusters……………………………………………...88

V.6 UV-vis adsorption of gold monolayer protected clusters………………….90

V.7. Photograph of the capillary electrophoresis instrumentation……………………91

V.8 SECM stage……………………………………………………………………...…92

V.9 Front panel of the program that controls the bipotentiostat………...……………93

V.10 Front panel of the program that moves the tip in a pattern “VU”……………….94

V.11 Electropherogram of the separation of Au MPCs……………………………..…94

V.12 Optical images of the deposition of Au protected MPCs……………………..…96

LIST OF ABBREVIATIONS

a	Radius of the UME
A	Active area
AC-SECM	Alternating current SECM
AFM	Atomic force microscope\microscopy
anti-HA	anti-hemagglutinin
anti-PA	anti-*Bacillus anthracis* protective antigen
BSA	Bovine serum albumin
C	Concentration
CE	Capillary electrophoresis
CEFP	Capillary electrophoresis fountain pen
CTR	Counter electrode
CV	Cyclic voltammetry
D	Diffusion coefficient
DPN	Dip-pen nanolithography
E	Field strength
ELISA	Enzyme linked immunosorbant assay
F	Faraday's constant
F_o	Fundamental resonant frequency
ΔF	Change in frequency
i_{ss}	Steady state current
I_T	Normalized tip current
i_{tip}	Tip current

L	(a) Full length of the capillary (b) Ratio of the distance of the UME tip from the substrate to the radius of the UME tip
L_d	Distance to the detector
Δm	Change in mass
MEAV	N-(methyl)-N-(ethylamine)-viologen dinitrate
MDCK	Madin-Darby canine kidney
MPC	Monolayer protected cluster
MPV	Metapneumovirus
n	Number of electrons
Ox	Oxidized mediator
PDMS	Polydimethylsiloxane
PBS	Phosphate buffer saline
PSI	Photosystem I
q	Charge
QCM	Quartz crystal microbalance
r	Stokes-Einstein radius
RE	Reference electrode
RSV	Respiratory syncytial virus
RT-PCR	Reverse transcription-polymerase chain reaction
SAM	Self-assembled monolayer
SE	Substrate electrode
SECM	Scanning electrochemical microscope\microscopy
t_r	Time to the detector

UME	Ultramicroelectrode
V	Voltage
N	velocity
VI	Virtual instrument
WE	Working electrode
XPS	X-ray photoelectron spectroscopy
ϵ_r	Relative permittivity
η	viscosity of the solution
η_1	Solution viscosity
μ	total mobility
μ_{ep}	Electrophoretic mobility
μ_{eo}	Electroosmotic flow
μ_q	Shear modulus of quartz
ρ_q	Density of quartz
ρ_1	Density solution
ζ	Zeta potential

CHAPTER I

Introduction

The application of advances in nanotechnology has the potential, possibly the destiny, to revolutionize the way we live our lives. Half a century ago it was suggested that machines will be built many orders of magnitude smaller and increasingly more precise; once scientists and engineers were given the opportunity to achieve what was at that time only theoretically proven to be possible, that suggestion became our reality.[1] Molecular machines, known to be produced and to be productive in nature, were forecast to be applied for our advantage in the construction of devices with atomic precision, due to their natural prevalence and millennia of development.[2-4] We are only 25 years from the publication of the synthesis of the buckminsterfullerene, C_{60}, that led to Smalley being awarded the Nobel prize in 1996,[5] and nanomaterials have already found their way into many commercially available products currently available at any mall. Companies have put nanoscale materials in our stain resistant pants, people apply them to their skin in make-up; they strengthen our epoxy, bikes, and golf clubs and are incorporated in over 800 other products.[6,7] After the explosion of research into fullerenes, the discovery that carbon nanotubes were a side product of the fullerene synthesis led to a second spurt into nanotechnology research covering nanoscale carbon molecules. Iijima *et al.* is often given credit[8] for the first published synthesis of carbon nanotubes.[9-11] These elongated buckyballs have been the subject of extensive research due to their outstanding physical properties.[12] Even with such an abundant amount of progress already achieved, the products that truly may benefit society have not yet been produced for global utilization. Nanomaterials have broad applications for solar energy collection and in the health sciences. Having stain-resistant pants is a minor extra convenience for inhabitants of developed countries, but nanotechnology could really have a profound impact on humanity if photovoltaics would be made readily available for all villages lacking sources of electrical power. Energy storage[13-18] and power transmission[19,20] advances and/or healthcare[21-23] improvements for the least well off could radically evolve the lives of the majority of the world's population, along with other promising areas of research including environmental remediation and water treatment. In order for these far-reaching imaginings to become reality, much work is required at the basic scientific level.

Themes for "nano" research that are playing an important role in scientific progress in many disciplines include nanoparticles, substrate patterning, and microscopy. Nanoparticles show great promise to produce advances with their tunable properties. When nanoparticles and nanoscale materials are combined for manufacturing, control of the location and morphology of these parts is of great importance. For these applications, the recent advances in printing[24] and lithography[25] are of great consequence. Advances in microscopy have greatly aided the study of the morphology and activity of materials produced in basic science. Three critical developments for the study of nanomaterials were the construction of the scanning tunneling microscope,[26] which earned Binnig and Rohrer the Nobel Prize in 1986,[27] atomic force microscope (AFM), which Binnig also had a hand in developing,[28] and the scanning electrochemical microscope (SECM), which was developed by Bard *et al.*[29] beginning in 1989 as a novel type of scanning probe microscopy.

The research presented in this dissertation utilizes microscopy, microgravimetry and electrophoresis techniques for the study and characterization of nanomaterials. The following is a brief overview of the working principles of the applied techniques.

1. Scanning Electrochemical Microscope

The SECM is an extremely versatile technique for studying substrate morphology and electrochemical activity near a surface.[30,31] SECM is an electrochemical technique involving a four-electrode system (Figure I.1), as opposed to the more common three-electrode electrochemical cells. SECM involves a reference electrode (RE), a counter electrode (CTR), and two working electrodes (WEs): (i) a conductive substrate electrode (SE) and (ii) a tip (probe) electrode, which is in all cases an ultramicroelectrode (UME) (diameter < 25 μm); the dimensions for unconventional UMEs can be as small as 10 nm,[30] permitting a 5 nm imaging resolution. For studies that can use an electrically conductive substrate, such as a gold layer, the SE is the fourth electrode (Figure I.1a); in the

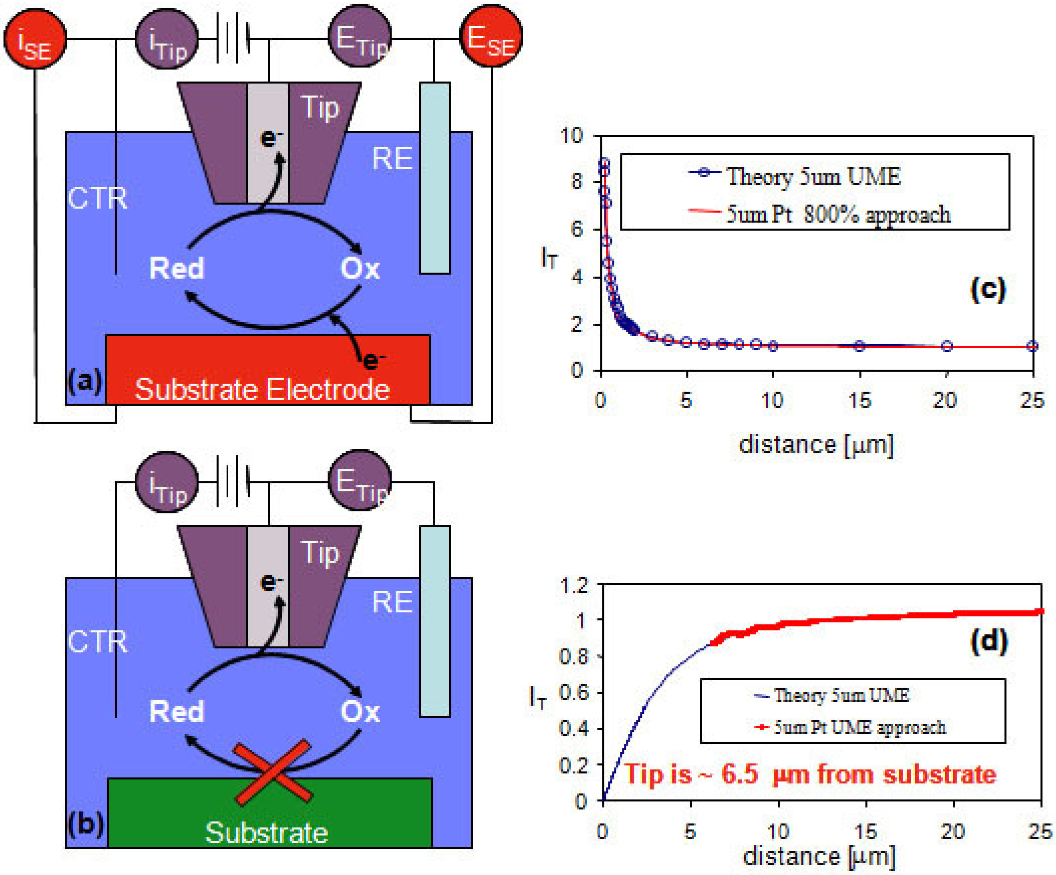

i_SE
i_Tip
E_Tip
E_SE
Tip
e-
RE
CTR
Red
Ox
e-
(a)
Substrate Electrode
10
8
6
4
2
0
I_T
Theory 5um UME
5um Pt 800% approach
(c)
0
5
10
15
20
25
distance [μm]
i_Tip
E_Tip
Tip
e-
RE
CTR
Red
Ox
(b)
Substrate
1.2
1
0.8
0.6
0.4
0.2
0
I_T
(d)
Theory 5um UME
5um Pt UME approach
Tip is ~ 6.5 μm from substrate
0
5
10
15
20
25
distance [μm]

Figure I.1: SECM principle, for conductive substrate electrode (a) and for insulating substrate (b); reduced species (Red) oxidized at the tip yield oxidized species (Ox); if regeneration of Red occurs, then (c) positive feed-back is observed; if not, then (d) negative feed-back approach curves are recorded.(a) has been adapted from Ciobanu, M.; Kincaid, H. A.; Jennings, G. K.; Cliffel, D. E., *Langmuir* **2005,** *21*, 692-698. (c) and (d) are unpublished data courtesy of Dr. M. Ciobanu.

case of an insulating substrate (Figure I.1b), the electrochemical cell has only three electrodes that allow current flow, but the substrate is still physically present in the system, although it is not connected to the circuit. The UME and SE are both immersed in the same solution that normally contains supporting electrolyte and a redox couple (electrochemical mediator, *e.g.*, ferrocene, Fc). The microscope operates by moving an UME to a close proximity of the SE and monitoring the electroactivity of an area as the tip is rastered across; the instrumentation can be seen in Figure I.2. Normally the output of the instrument is the tip current (i_{tip}) *vs.* distance traveled by tip. The UME can travel vertically, when recording approach curves, or horizontally, as in the case of imaging or lateral scanning. For a conductive substrate and a perfectly reversible redox couple, the potentials would be set such that the mediator would undergo oxidation at one of the electrodes and reduction at the other one (*e.g.*, oxidation at the UME and reduction at the SE). When the two electrodes are far from each other, the oxidation reaction occurs at the UME, and the depleted mediator, in its reduced state (Red), is replenished by diffusion. The current recorded at the tip will maintain an almost constant value,

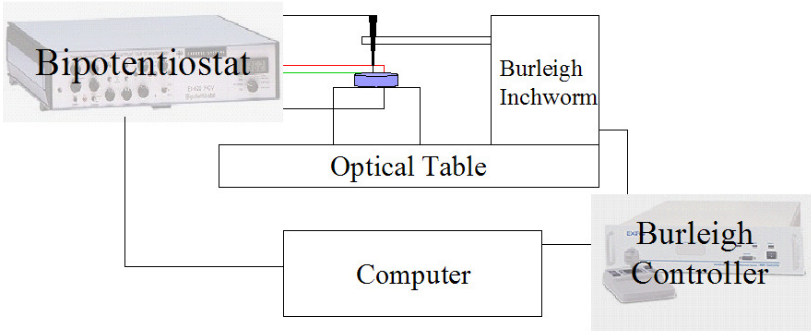

Figure I.2. SECM schematic.

the steady state current, i_{ss}, until the distance between the two electrodes is less than a few µm:

$$i_{ss} = 4nFDCa \tag{1}$$

For Equation (1), n is the number of electrons, F [96,485 C $mole^{-1}$] is Faraday's constant, D [$cm^2\ s^{-1}$] is the diffusion coefficient, C [mole cm^{-3}] is the concentration and a [cm] is the radius of the UME. A positive feedback loop is created, wherein the oxidized mediator (Ox) produced at the tip will quickly diffuse to the SE, where it will undergo the reduction reaction, and Red will diffuse back to the UME. As the distance between electrodes decreases, this electrochemical cycling will increase, and the tip current will exhibit a sharp increase (Figure I.1c) and hence provide a positive feedback signal, with a few hundred percent increase for the final approach of the UME to within a few hundred nm of the SE.

$$I_T(L) = 0.68 + \frac{0.78377}{L} + 0.3315e^{\frac{-1.0672}{L}} \tag{2}$$

Equation (2) is a mathematical expression of the positive feedback current, where L is the ratio of the distance of the tip from the substrate to the radius of the UME tip and I_T is the normalized current tip, $I_T = i_{tip}/i_{ss}$. For the case of an insulating substrate, the substrate cannot perform the reduction reaction. As the two electrodes come within microns of each other, the tip current will decrease (Figure I.1d) as the proximity of the two electrodes blocks diffusion to the tip, providing a negative feedback signal.

$$I_T(L) = [0.292 + \frac{1.5151}{L} + 0.6553e^{\frac{-2.4035}{L}})]^{-1} \qquad [3]$$

Equation (3) is a negative feedback current expression, and is also encountered for the case of a conductive SE with an irreversible mediator.[32,33] For each of the cases described above the UME functions as an amperometric tip, monitoring the faradaic current of a given electrode reaction, by having its own potential set for this purpose. SECM applications have been described for potentiometric tips as well, where the concentration of a certain analyte is recorded as a function of the potential difference between the tip and a reference electrode (*e.g.*, pH monitoring).[34] SECM images can be obtained by holding the tip in the vertical direction at a constant position of a few hundred nm from the substrate and rastering it across the horizontal area of interest. This way the tip can map the electrochemistry of the studied surface. Alternatively, if the tip current is maintained at a constant value while probing the area, the topography of the surface will be recorded directly in distance units, providing a method for profilimetry.

2. Atomic Force Microscopy

AFM is a powerful tool for surface studies with resolution down to a single atom within the molecule that is adsorbed onto a substrate.[35] The piezoelectric scanner is used to position the tip and the sample in close proximity with each other and raster the tip across the substrate. The laser and photodiode array are used for the measurement of the deflection of the cantilever due to interactions between the tip and sample. This technique is operable in multiple modes. For extremely smooth surfaces the AFM may operate using a constant height in contact mode where the topograph is produced by tip deflection. In tapping mode AFM the tip is oscillated in large amplitudes, between 10 and 200 nm, and comes in intermittent contact with the substrate. Non-contact mode also uses the oscillation of the tip, with smaller amplitudes, typically less than 10 nm, while monitoring tip-surface forces in ambient conditions. It is also possible to operate the AFM in a liquid cell or within a liquid droplet allowing the monitoring of in situ electrochemical studies, studies of the dissolution and deposition of crystals and in situ studies of DNA,[36] membranes[37] and cells.[38] One significant advantage that the AFM benefits from over the STM is that it does not require the substrate to be

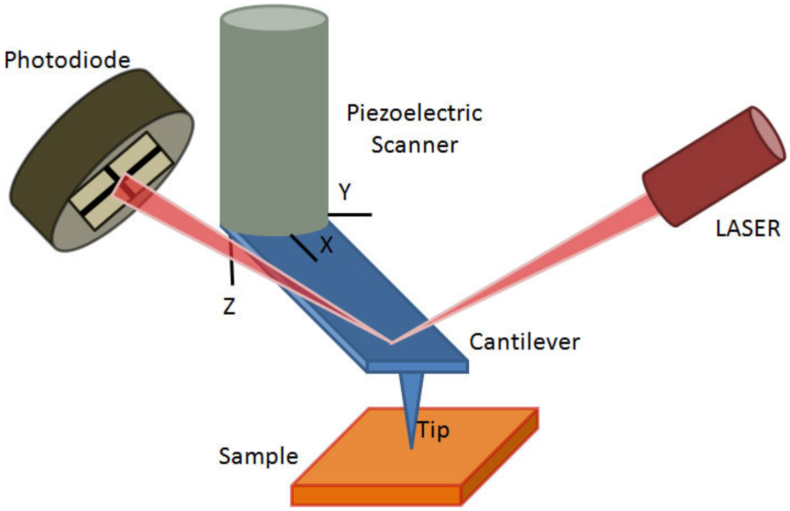

Figure I.3. AFM schematic. Laser positioning system where the reflection off of the back of cantilever onto the photodiode is used to position the tip above the sample. Piezoelectric scanner(s) control the xyz axes and position of the tip relative to the sample.

conductive. Nor is a vacuum apparatus required for the resolution to reach sub-nanometer or atomic scale.[39] This microscopy technique has been applied to proteomic research; with the application of modified tips, the binding forces of surface proteins on cells as well as the hydrophobicity of the cell may be determined.[40]

3. Quartz Crystal Microbalance

Quartz crystal microbalance (QCM) is a fast and portable method applying a piezoelectric transducer for microgravimetry. The QCM is based on the measurement of frequency changes of a piezoelectric crystal caused by the variations in mass due to specifically bound molecules. The QCM platform has the capability to detect nanogram changes in mass.[41]

The relationship between the change in frequency, ΔF [Hz], resulting from a change in mass, Δm [ng], was originally developed for the gas phase, and is given by the Sauerbrey equation:[42]

$$\Delta F=-2F_o^2\Delta m/\ [A\ (\mu_q\rho_q)^{1/2}] \qquad [4]$$

where F_o [Hz], is the fundamental resonant frequency, μ_q [kg m^{-1} s^{-2}], is the shear modulus of quartz (2.947×10^{10} kg m^{-1} s^{-2}), ρ_q [kg m^{-3}] is the density of quartz (2648 kg m^{-3}) and A [m^2] is the active area. In liquids, the frequency change of the crystal depends heavily on the density and viscosity of the solution. The relationship between the oscillation frequency change of a quartz resonator in contact with a liquid and the accumulated mass was first described by Kanazawa and Gordon who derived Equation (5).[43] Thompson *et al.* also reviewed the details of the characteristics of QCM in the liquid phase.[44]

$$\Delta F = -F_o^{3/2}[\rho_1 \eta_1 / (\pi \rho_q \mu_q)]^{1/2} \qquad [5]$$

where ρ_1 [kg m^{-3}] is the density solution, and η_1 [kg m^{-1} s^{-1}] is the viscosity of solution. Due to the difficulty in acquiring the change of density and viscosity at the interface between the solution and the quartz crystal during an experiment, the quantification of the mass change in solution is still not a straightforward process. Gerdon *et al.* have reported a method to calibrate the change in frequency as a function of the change in resistance based on the fact that the interface resistance change is proportional to the change of viscosity and density at the interface of quartz.[45]

The high sensitivity of the technique and the relationship between mass and frequency make the QCM ideal for sensing applications through changes in absorbed mass. QCM has lead to a wide range of research and applications in gas phase detection,[46,47] immunosensors,[48-52] DNA biosensors[53,54] and drug analysis.[55] Gerdon *et al.* have recently demonstrated that QCM can be used for the detection of a peptide using a specific epitope presentation on monolayer protected nanoclusters and have presented the corresponding kinetic studies for different peptides, including anthrax bacterium, Ebola virus and the flu virus.[56,57]

4. Capillary Electrophoresis

Capillary electrophoresis (CE) is a technique for the separation of ionic species based on their charge to size ratio. An electric field is created that moves a buffer solution from the source vial to the destination vial, through a small diameter capillary. The capillary, source vial, destination vial and sample vials all contain the buffer solution (Figure I.4). In order to introduce a sample into the capillary, the source end of the capillary is introduced into the sample vial, which contains the sample in addition to the buffer solution. Once the sample is introduced into the source end, the capillary is returned to the source vial for the separation procedure. The electric field then moves the buffer solution through the capillary at the rate of the electroosmotic flow, μ_{eo} [$m^2\ V^{-1}\ s^{-1}$]:

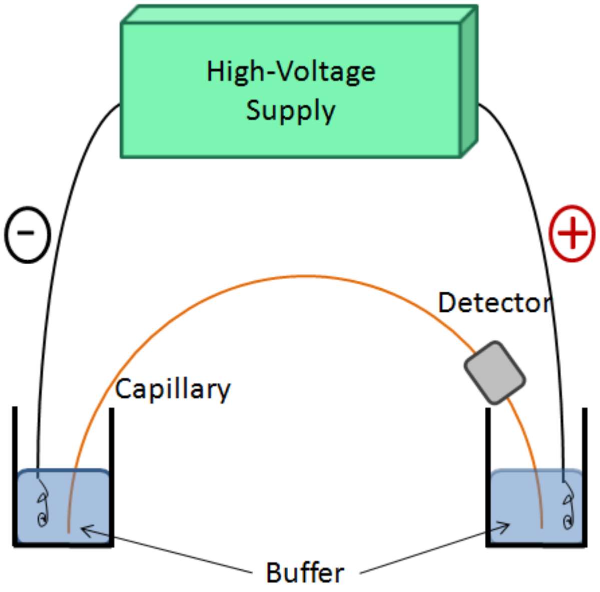

Figure I.4. Capillary electrophoresis schematic showing source and destination buffer vials, capillary, and high-voltage supply.

$$\mu_{eo} = \frac{\epsilon_r \zeta}{\eta_1} \qquad [6]$$

where ϵ_r is the relative permittivity of the buffer solution, ζ [V] is the zeta potential of the capillary wall and η_1 [kg s^{-1} m^{-1}] is the solution viscosity. The components of the sample are brought toward the detector at a different migration rate based on the different mobilities for each component. The electrophoretic mobility, μ_{ep} [m^2 V^{-1} s^{-1}] given by Equation (7) is a function of the ratio of component charge q [C] to size, r [m]. Here r is the Stokes-Einstein radius of the analyte.

$$\mu_{ep} = \frac{q}{6\pi\eta r} \qquad [7]$$

The electrophoretic mobility is determined experimentally from the time, t_r [s], required for the analyte to reach the detector.

$$\mu_{ep} = \frac{L_d}{t_r}\frac{L}{V} \qquad [8]$$

Here V [V] is the voltage, L_d [m] is the distance to the detector and L [m] is the full length of the capillary. Even the smallest highly charged anions will be forced from the source vial to the destination vial by the electroosmotic flow.

The study of nanotechnology is critical in the development of devices that will become ubiquitous in the future. The results of studying nanomaterials are just emerging as viable products for everyday application. Further development of the substrates and characterization tools in the subjects of biomaterials and photovoltaics will assuredly lead to technological advances that have the prospect of beneficially impacting the lives of countless people.

5. References

1. Feynman, R. P. In *There's Plenty of Room at the Bottom*, American Physical Society, California Institute of Technology, California Institute of Technology: California Institute of Technology, 1959.

2. Drexler, K. E., *Proc. Natl. Acad. Sci. U. S. A.* **1981,** *78* (9), 5275-8.

3. Drexler, K. E., *Annu. Rev. Biophys. Biomol. Struct.* **1994,** *23*, 377-405.

4. Drexler, K. E., *Nature (London)* **2003,** *422* (6929), 257.

5. Kroto, H. W.; Heath, J. R.; O'Brien, S. C.; Curl, R. F.; Smalley, R. E., *Nature (London)* **1985,** *318* (6042), 162-3.

6. Kahn, J., *National Geographic* **2006,** *209* (6), 98 - 110.

7. Marquis, B. J.; Love, S. A.; Braun, K. L.; Haynes, C. L., *Analyst (Cambridge, U. K.)* **2009,** *134* (3), 425-439.

8. Monthioux, M.; Kuznetsov, V. L., *Carbon* **2006,** *44* (9), 1621-1623.

9. Iijima, S., *Nature* **1991,** *354* (6248), 56.

10. Iijima, S.; Ichihashi, T., *Nature (London)* **1993,** *363* (6430), 603-5.

11. Bethune, D. S.; Kiang, C. H.; de Vries, M. S.; Gorman, G.; Savoy, R.; Vazquez, J.; Beyers, R., *Nature (London)* **1993,** *363* (6430), 605-7.

12. See, C. H.; Harris, A. T., *Industrial & Engineering Chemistry Research* **2007,** *46* (4), 997-1012.

13. Hu, L.; Choi, J. W.; Yang, Y.; Jeong, S.; La Mantia, F.; Cui, L.-F.; Cui, Y., *Proc. Natl. Acad. Sci. U. S. A.* **2009,** *106* (51), 21490-21494, S21490/1-S21490/13.

14. Chen, X.; Mao, S. S., *Chem. Rev. (Washington, DC, U. S.)* **2007,** *107* (7), 2891-2959.

15. Chen, J.; Cheng, F., *Acc Chem Res* **2009,** *42* (6), 713-23.

16. Bruce, P. G.; Scrosati, B.; Tarascon, J.-M., *Angew. Chem., Int. Ed.* **2008,** *47* (16), 2930-2946.

17. Arico, A. S.; Bruce, P.; Scrosati, B.; Tarascon, J.-M.; van Schalkwijk, W., *Nat. Mater.* **2005,** *4* (5), 366-377.

18. Sunandana, C. S., *Resonance* **2007,** *12* (5), 31-36.

19. Shanenko, A. A.; Croitoru, M. D.; Peeters, F. M., *Phys. C (Amsterdam, Neth.)* **2008,** *468* (7-10), 593-598.

20. Rao, C. N. R.; Sood, A. K.; Subrahmanyam, K. S.; Govindaraj, A., *Angew. Chem., Int. Ed.* **2009,** *48* (42), 7752-7777.

21. He, B.; Morrow, T. J.; Keating, C. D., *Curr. Opin. Chem. Biol.* **2008,** *12* (5), 522-528.

22. Bharali, D. J.; Khalil, M.; Gurbuz, M.; Simone, T. M.; Mousa, S. A., *Int. J. Nanomed.* **2009,** *4*, 1-7.

23. Wei, D.; Bailey, M. J. A.; Andrew, P.; Ryhaenen, T., *Lab Chip* **2009,** *9* (15), 2123-2131.

24. Braunschweig, A. B.; Huo, F.; Mirkin, C. A., *Nature Chemistry* **2009,** *1*, 353-358.

25. Wolfe, D. B.; Qin, D.; Whitesides, G. M., *Methods in Molecular Biology* **2010,** *583*, 81-107.

26. Binning, G.; Rohrer, H., *IBM Journal of Research and Development* **1986,** *30* (4), 355.

27. Binning, G.; Rohrer, H., Scanning Tunneling Microscopy - from Birth to Adolescence. In *Nobel Lecture*, Royal Swedish Academy of Sciences: Stockholm, Sweden, 1986.

28. Giessibl, F. J., *Reviews of Modern Physics* **2003,** *75* (3), 949-983.

29. Bard, A. J.; Fan, F. R. F.; Kwak, J.; Lev, O., *Anal. Chem.* **1989,** *61(2)*, 132-138.

30. Amemiya, S.; Bard, A. J.; Fan, F.-R. F.; Mirkin, M. V.; Unwin, P. R., *Annu. Rev. Anal. Chem.* **2008,** *1*, 95-131.

31. Sun, P.; Laforge, F. O.; Mirkin, M. V., *Phys. Chem. Chem. Phys.* **2007,** *9* (7), 802-823.

32. Bard, A. J.; Fan, F. R. F.; Mirkin, M. V., Scanning Electrochemical Microscopy. In *Electroanalytical Chemistry*, Marcel Dekker, Inc.: New York, 1994; Vol. 18, pp 243-373.

33. Bard, A. J.; Mirkin, M. V., *Scanning Electrochemical Microscopy*. Marcel Dekker, Inc.: New York, 2001; p 650 pp.

34. Wei, C.; Bard, A. J.; Kapui, I.; Nagy, G.; Toth, K., *Anal. Chem.* **1996,** *68*, 2651-2655.

35. Gross, L.; Mohn, F.; Moll, N.; Liljeroth, P.; Meyer, G., *Science* **2009,** *325* (5944), 1110-1114.

36. Pastre, D.; Hamon, L.; Mechulam, A.; Sorel, I.; Baconnais, S.; Curmi, P. A.; Le Cam, E.; Pietrement, O., *Biomacromolecules* **2007,** *8* (12), 3712-3717.

37. Frederix, P. L. T. M.; Bosshart, P. D.; Engel, A., *Biophysical journal* **2009,** *96*, 329-338.

38. Drake, B.; Prater, C. B.; Weisenhorn, A. L.; Gould, S. A. C.; Albrecht, T. R.; Quate, C. F.; Cannell, D. S.; Hansma, H. G.; Hansma, P. K., *Science* **1989,** *v243* (n4898), p1586(4).

39. Gan, Y., *Surface Science Reports* **2009,** *64*, 99-121.

40. Dufrêne, Y. F., *Proteomics* **2009,** *9*, 5400-5405.

41. Cacacem, M. G.; Landau, E. M.; Ramsden, J. J., *Q. Rev. Biophys.* **1997,** *30* (3), 37.

42. Sauerbrey, G., *Physics* **1959,** *155*, 7.

43. Kanazawa, K. K.; Gordon, J. G., *Anal. Chem.* **1985,** *57* (8), 2.

44. Thompson, M.; Kipling, A. L.; Duncan-Hewitt, W. C.; Rajakovic, L. V.; Cavic-Vlasak, B. A., *The analyts* **1991,** *116* (9), 10.

45. Gerdon, A. E.; Wright, D. W.; Cliffel, D. E., *Anal. Chem.* **2005,** *77* (1), 7.

46. Guilbault, G. G., *Analytical Chemistry Symposia Series* **1983,** *17*, 7.

47. Guilbault, G. G.; Luong, J. H., *J. Biotechnol.* **1988,** *9* (1), 10.

48. Carrigan, S. D.; Scott, G.; Tabrizian, M., *Langmuir* **2005,** *21* (13), 8.

49. Koenig, B.; Graetzel, M., *Anal. Chem.* **1994,** *66* (3), 4.

50. Lee, Y.-G.; Liu, S.-S.; Chang, K.-S., *Anal. Lett.* **2005,** *38* (2), 9.

51. Su, C.-C.; Wu, T.-Z.; Chen, L.-K.; Yang, H.-H.; Tai, D.-F., *Anal. Chim. Acta* **2003,** *479* (2), 7.

52. Zuo, B.; Li, S.; Guo, Z.; Zhang, J.; Chen, C., *Anal. Chem.* **2004,** *76* (13), 5.

53. Aslanoglu, M.; Houlton, A.; Horrocks, B. R., *The Analyst* **1998,** *123* (4), 10.

54. Caruso, F.; Rodda, E.; Furlong, D. N.; Niikura, K.; Okahata, Y., *Anal. Chem.* **1997,** *69* (11), 7.

55. Attili, B. S.; Suleiman, A. A. In *Development of piezoelectric biosensors for the determination of cocaine and cortisol*, Proceedings of the Annual Meeting of the Adhesion Society, Adhesion Society: 1996; p 4.

56. Gerdon, A. E.; Wright, D. W.; Cliffel, D. E., *Biomacromolecules* **2005,** *6* (6), 6.

57. Gerdon, A. E.; Wright, D. W.; Cliffel, D. E., *Angewandte Chemie, International Edition* **2006,** *45* (4), 5.

Chapter II

Surface Characterization of Platinized Photosystem I Oriented and Bound to a Au-Modified Substrate[*]

1. Introduction

The products of photosynthetic organisms comprise in one form or another most of the food and energy sources our civilization utilizes.[1] These organisms capture and convert the photons that they absorb from the sun to facilitate the synthesis of organic compounds. The photosynthetic organisms utilize electron transfer proteins that have been optimized through the selective process of evolution. The membrane proteins that perform this crucial function in higher plants are photosystem I (PSI) and photosystem II. Although the annual production of material through the photosynthetic process by photosynthetic organisms is enormous, only 1/20 of 1% of the sunlight that reaches the Earth is utilized.[2] However, sunlight is exploited with an outstanding photosynthetic efficiency, of 85% for the complete process from a photon combining with CO_2 to the production of an oxygen molecule and sugar, without consideration for the quality of light or location of the organism.[3] The efficiency of photosynthetic organisms (85%) compares favorably to the current standard in photovoltaic generation, the Si thin film solar cell, which can reach efficiencies of

---

[*] This Chapter has been formatted for submission to Thin Solid Films. The authors of the paper are: M.L. Krim, M. Ciobanu, B.W. Schmidt, C.J. Faulkner, G.K. Jennings, D.E. Cliffel.

18% in production and have a theoretical maximum of 33%.[4-6] Thus, there is an enormous percentage of untapped energy from the sun and a very efficient system for conversion of this energy to be exploited. PSI catalyzes photoinduced electron transfer across the photosynthetic membrane in cyanobacteria, green algae, and plants.[7] PSI is a reaction center core antenna complex located in the chloroplast thylakoid membrane of plants, which captures sunlight and converts it into energy.[7] In this study we have used the protein complex PSI that produces a voltage drop of 1 V on the picosecond timescale.[3] Extracting, purifying and applying this protein complex in applications for the direct capture of the solar radiation would result in utilizing billions of years of evolution for the purpose of directly producing electrical power for society.

In photosynthetic organisms, an electron is transferred from cytochrome f to plastocyanin, and then further to the P700 reaction center located near the oxidizing (donor) side of PSI; the P700 center becomes excited by the native photosynthetic energy received in the form of sunlight.[8] After being transferred through the PSI complex, the electron is picked up by ferredoxin at the reducing (acceptor) side of PSI and transferred to $NADP^+$, which is further converted into NADPH.[8] NADPH is the form of chemical energy used by plants to sustain their life and synthesize organic compounds. Extraction of PSI out of the thylakoid membrane into a stabilizing detergent containing solution and purified with a hydroxylapatite column[9] allows for the selective manipulation of either the acceptor or the donor side of the PSI complex.[10] Therefore the electron is made readily available for further applications.

Upon extracting and characterizing PSI, a naturally evolved photodiode, by established methods,[11-13] this protein complex can be oriented preferentially on a gold substrate modified with X-terminated ω-alkanethiol, according to methods described by Lee *et al*.[14,15] X is a terminal group ranging from methyl to hydroxyl, rendering the surface different energy characteristics, from low-energy to high-energy, respectively.[16] Lee *et al*.[17] also showed that the oriented PSI retains the ability to convert the energy of the sun into utilizable electrical energy since the kinetics of the electron transfer intrinsic to the PSI protein complex are not materially altered through the processes required to bind the complex. PSI is able to reduce Hill reagents, such as dyes and metal complexes that are artificial electron acceptors in the Hill reaction. Designer surfactants have been synthesized in order to impart PSI with increased stability, reducing the blue shift in peak absorbance and increasing the length of time the PSI remains active after drying.[18,19]

For the work presented in this paper we use PSI to convert a metal ion, *i.e.*, Pt^{2+}, into its neutral state, in the form of a nanoparticle at the reducing (acceptor) side of the PSI complex.[20] In the experiments described in Lee *et al.*'s[20] paper, a configuration where the PSI is sandwiched between the two metals is illustrated, but there is no individual connectivity to the single PSI molecules as the protein complexes are used as part of thylakoid membranes.

A consequence of using PSI to reduce a Hill reagent is the production of a potential fuel (H_2) by the splitting of water.[21,22] PSI may be used for the recovery of solar energy directly or indirectly through the production of H_2.[22-25] It was also shown by Lee *et al.*[26] that the platinization reaction of isolated PSI protein complexes can be used to "weld" the PSI to a Au substrate with the possibility of creating 2D spatial arrays of PSI protein complexes. This creates a PSI-M^0-Au conformation where the two metals are short circuited together.

It is also possible to attach PSI via a molecular wire to a nanoparticle for the production of H_2.[27,28] Terasaki *et al*. extracted vitamin K_1 from PSI and immersed a surface terminated in a naphthoquinone-viologen linked compound in a PSI solution where the protein complex lacked the extracted segment. The naphthoquinone-viologen compound inserts into the PSI thereby attaching the protein to the substrate.[27] Another strategy for linking a PSI protein complex to a Pt nanoparticle for the production of H_2 is the use of a conjugated dithiol.[25,29,30]

Alternately, it is possible to predeposit Au nanoparticles on a flat Au substrate to create a 3D platform for the attachment of PSI. Terasaki *et al.*[31] deposited Au nanoparticles on flat Au and adsorbed a sulfonic acid thiol for the further adsorption of PSI. In this arrangement a nanoparticle multistructure is created on top of a flat Au surface for the attachment of PSI in order to increase the photocurrent density generated; the light is absorbed by PSI and transferred through the Au electrode.

In addition to the orientation of PSI, control of the location on the substrate that the protein complex occupies is important for applications utilizing PSI. We have previously demonstrated the ability to both pattern and orient individual PSI molecules on conductive surfaces,[32] while retaining the electron transfer properties of the protein complex.[33] We have shown that it is possible to modify a substrate with a pattern of adsorbed chemical monolayer that preferentially orients PSI in the chosen direction during the adsorption, thus allowing for selected regions to be designed to contain the photodiode in the orientation that is beneficial for a specific application.[32] We have also performed studies examining the types of surface composition that inhibit the adsorption of PSI, providing an additional tool for the design of electronic devices with PSI.[16] Continuing in this vane of research is the isolation of adsorbed PSI photodiodes. After investigating the preferential adsorption/orientation of PSI protein complexes onto different substrates, we isolated individual PSI protein complexes from one another other through the backfilling of the surface.[34] We accomplished this using longer and differently terminated n-alkane thiols to intercalate between the PSI groups through a backfilling process.[34] We were also able to form a critically dense monolayer of oriented PSI protein complexes by performing the PSI adsorption onto the self-assembled monolayers (SAMs) under vacuum; this dense monolayer of oriented PSI is capable of achieving optimal photocurrents.[35] It would be beneficial for future applications to establish connectivity to the exposed end of the patterned protein complex.

While the work presented here does not deal with PSI patterning, we ascertain the ability of establishing connectivity at the exposed end of oriented PSI protein complexes on mercaptoundecanol-modified Au substrates. We are using a SAM of 11-mercapto-1-undecanol ($HOC_{11}SH$) to connect the PSI protein complex in the preferred orientation, with the reducing (acceptor) side up.[10,16,32,33] The Pt is then photoreduced on the exposed side of the PSI protein complex, which retains activity upon adsorption onto hydroxyl-terminated SAMs.[33]

In order to characterize the system that we have built, we performed atomic force microscopy (AFM) measurements for each step in the assembly process. We have examined by AFM the roughness of the Au substrate, the 11-mercapto-1-undecanol SAM and the adsorbed PSI layer in an analogous style to the one used by Fotiadis *et al.*[36] for the analysis of two-dimensional PSI crystals and finally the roughness of the photoreduced Pt nanoparticles on the top of the natural photodiode with a similar method to Frolov *et al.*[37] In order to confirm that we succeeded in producing the entire complex, namely the presence of Pt atop of the PSI protein complex, we employed X-ray photoelectron spectroscopy (XPS). The XPS technique was applied to confirm the presence of Pt in a similar manner to Gao *et al.*,[38] Hills *et al.*,[39] and Fu *et al.*[40]

2. Experimental

A. Materials. EDTA, Na_2PtCl_6 x $6H_2O$, Na_2HPO_4 x $7H_2O$, acetone, sodium ascorbate, 11-mercapto-1-undecanol and DL-dithiothreitol were purchased from Sigma Aldrich. NaH_2PO_4 x H_2O, HCl, $MnCl_2$ x $4H_2O$, $MgCl_2$ x $6H_2O$, $Na_4P_2O_7$ x $10H_2O$, $K_3Fe(CN)_6$ and NaCl were purchased from ThermoFisher. Triton X-100, 4-(2-hydroyethyl)-1-piperazineethane sulfonic acid (HEPES), D-sorbitol, ascorbic acid and Tricine were purchased from Acros. NaOH was purchased from EM Science. Ethanol (200 proof) was purchased from Aaper. Hydroxylapatite was purchased from Calbiochem. ASTM type I (~18 MΩ) analytical grade water was acquired from Modulab Water Systems unit. Freshest available baby spinach was purchased from local groceries.

B. Extraction and Characterization of PSI. Commercial bagged spinach leaves were used for the isolation of active spinach thylakoid membranes according to methods described by Reeves and Hall.[13] An hydroxylapatite column was used to further separate native PSI according to Shiozawa *et al.*[9] and Lee *et al.*[41] The elutant containing active PSI suspended by 1 mM Triton X-100 in 200 mM phosphate buffer at pH 7 was stored in a –80 ^oC freezer. Characterization for P700 content was performed by monitoring the chemically induced absorbance change (difference between oxidized and reduced spectra), as described by Baba *et al.*[42] For chlorophyll content, the measurements were in 80% acetone, as indicated by Arnon.[11] These two procedures revealed 22 chlorophyll molecules per P700 reaction center for the PSI used in the experiments described here.

C. Platinization of PSI. Au substrates were prepared by evaporating 1250 Å Au onto (100) silicon wafers pretreated by evaporation to 100 Å with Cr.

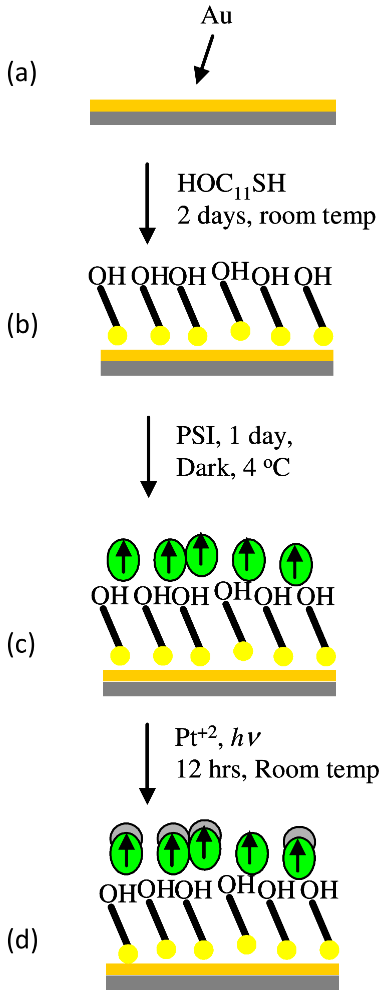

Figure II.1. Platinization of PSI: (a) evaporated Au substrate on a silicon wafer; (b) alkane thiol SAM on Au ($HOC_{11}S/Au$) prepared by immersion of Au in 2 mM $HOC_{11}SH$ in ethanol for 2 days at room temperature; (c) oriented protein on hydroxyl terminated SAM ($PSI/HOC_{11}S/Au$) prepared by immersion of $HOC_{11}S/Au$ in a PSI solution for 1 day at 4° C in the dark; (d) red light was shone directly on the $PSI/HOC_{11}S/Au$ substrates for 12 hours in a solution of 2 mM Na_2PtCl_6 x 6 H_2O for the photoreduction of Pt onto the PSI active acceptor site ($Pt/PSI/ HOC_{11}S/Au$).

Figure II.1 describes the strategy used for platinizing oriented PSI protein complexes immobilized on solid substrates. The Au (Figure II.1a) substrates were cut into 1 cm^2 sections. SAMs were prepared by immersion of the gold substrates in 2 mM 11-mercapto-1-undecanol in ethanol for 2 days. These substrates were rinsed in ethanol followed by water. The $HOC_{11}S/Au$ substrates (Figure II.1b) were then immersed in the protein solutions of 5 x 10^{-6} M PSI in 1 mM Triton X-100 in 200 mM phosphate buffer, pH 7 in a refrigerator at 4 °C for 1 day. The PSI films on $HOC_{11}S/Au$ were rinsed in water. The

PSI/HOC$_{11}$S/Au substrates (Figure II.1c) were immersed in a solution of 2 mM $Na_2PtCl_6 \times 6H_2O$ in 1 mM Triton X-100 in 200 mM phosphate buffer, pH 7, and light was shone directly on the PSI/HOC$_{11}$S/Au substrates for 12 hours using a 250 W cold light source (Leica KL 2500 LCD) equipped with a red filter. The resulting Pt/PSI/HOC$_{11}$S/Au assemblies (Figure II.1d) were rinsed with water and allowed to air dry before their characterization.

D. Atomic Force Microscopy. AFM analysis of all of the samples was performed on a Digital Instruments (division of Veeco Instruments Incorporated) multimode AFM. The Nanoscope IIIa scanning probe microscope controller was used in cooperation with the proprietary Nanoscope III, version 4.43R8, software for control of the AFM tip and imaging parameters. Silicon tips were purchased from Budget Sensors (Sofia, Bulgaria). Double sided tape was used to adhere the sample to be imaged. All imaged areas were 1 μm side squares with a z-axis range of 100 nm. The imaging speed was 1 μm s^{-1}.

E. X-ray Photoelectron Spectroscopy. XPS was performed on a home-built instrument assembled in Prof. Bridget R. Rogers' laboratory, in the Department of Chemical Engineering at Vanderbilt University. Mg was the anodic X-ray source with a radiation of 1253.6 eV. The samples were analyzed with an incident angle of 60 degrees and a 150 eV band pass.

3. Results and Discussion

We have photoreduced Pt onto a PSI/HOC$_{11}$S/Au substrate (Figure II.1). The substrate surface preparation was performed by using a HOC$_{11}$SH SAM that preferentially orients the adsorption of PSI in the desired arrangement, with the donor side of the PSI near the SAM. The PSI protein complex is adsorbed onto the HOC$_{11}$S/Au surface in such a manner that the stromal (reducing) side of the natural photodiode is exposed to the Pt^{2+} containing solution.

The surface covered with photodeposited platinum on PSI and the precursory steps were investigated by AFM (Figure II.2). We have analyzed the topology in the order of the layer loading, following the sequence shown in Figure II.1, to confirm that the system was produced as designed. The initial substrate, evaporated Au on Si wafers, prior to any modification, is shown in Figure II.2a; the Au layer is produced with a root mean squared (RMS) roughness of 1.53 nm. This roughness is the result of the evaporation process where small isolated groups of Au atoms are on the surface and discernable in the AFM image. The next step to be examined was the formation of the SAM on Au. The HOC$_{11}$S/Au layer shown in Figure II.2b achieved an average roughness of 1.28 nm. This slight decrease in the RMS amplitude from 1.53 nm for Au to 1.28 nm for HOC$_{11}$S/Au indicates that the SAM is able to cover the Au substrate in a manner that reduces the apparent roughness by filling in the imperfections seen on the bare Au surface, which are due to the evaporative process. The penultimate substrate in this series was PSI adsorbed to the hydroxyl terminus of the monolayer. The PSI/$HOC_{11}S$/Au layer represented in Figure II.2c displays a

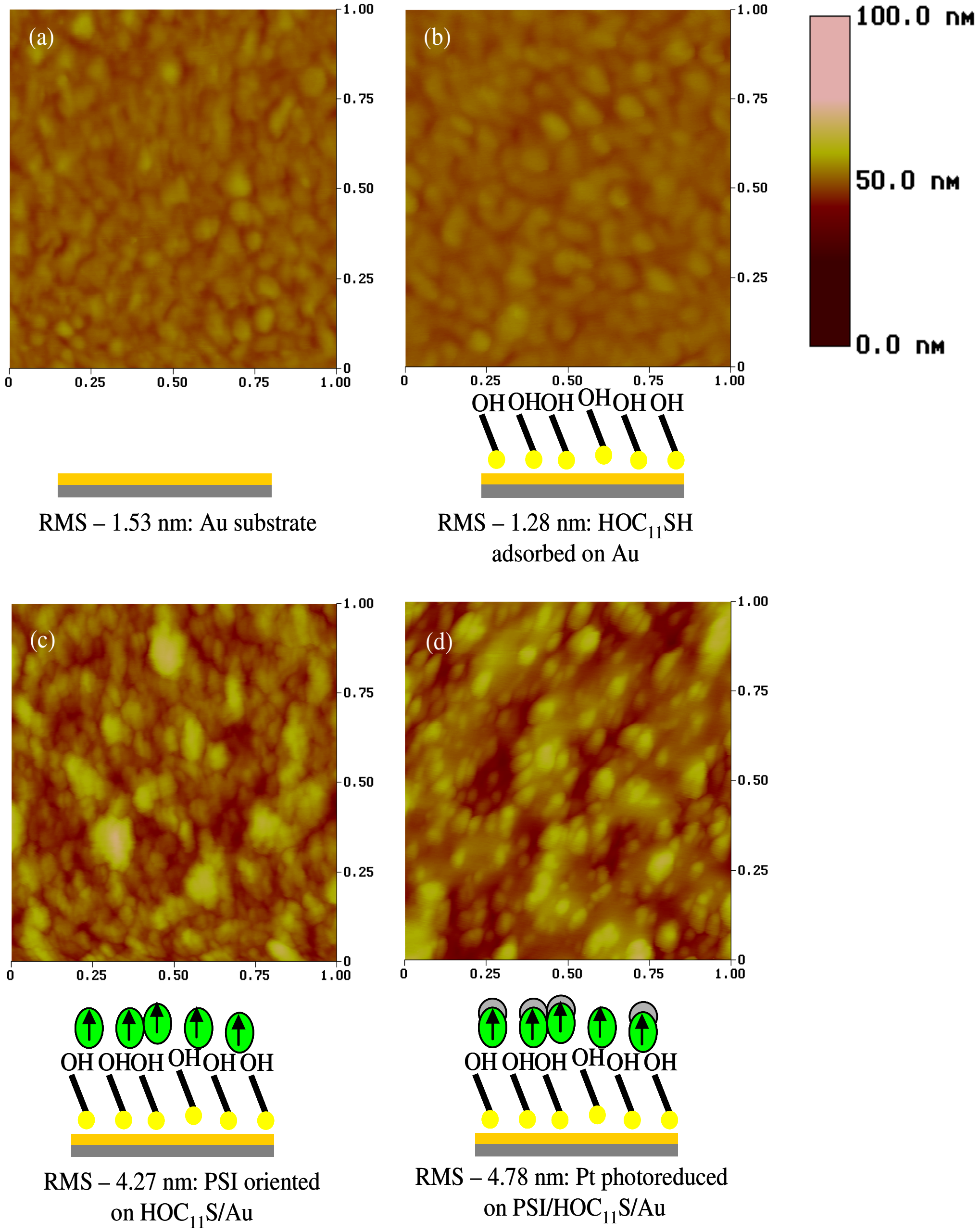

RMS – 1.53 nm: Au substrate

RMS – 1.28 nm: $HOC_{11}SH$ adsorbed on Au

RMS – 4.27 nm: PSI oriented on $HOC_{11}S$/Au

RMS – 4.78 nm: Pt photoreduced on PSI/$HOC_{11}S$/Au

Figure II.2. AFM images of the surfaces used and created in the steps for the photoreduction of Pt onto the active acceptor site of oriented PSI: (a) bare Au substrate produces a RMS amplitude of 1.53 nm; (b) $HOC_{11}S$/Au substrate displays a RMS amplitude of 1.28 nm; (c) PSI/$HOC_{11}S$/Au shows a RMS amplitude of 4.27 nm; (d) Pt photoreduced on PSI/$HOC_{11}S$/Au exhibits a RMS amplitude of 4.78 nm.

roughness of 4.27 nm. This is a reasonable increase in average roughness because the PSI adsorption gives clearly distinguishable units and the PSI is reported to be ~ 6 nm in size.[8] During the last step, we photoreduced Pt^{2+} from solution onto the adsorbed PSI layer as Pt^0, and thus completed the construction of the proposed assembly. The topography of the photoreduced Pt on PSI/$HOC_{11}S$/Au is presented in Figure II.2d and the final structure shows an average roughness of 4.78 nm. This AFM study of the topography for each individual step in the formation of photoreduced Pt on PSI/$HOC_{11}S$/Au substrates presents evidence that the proposed structure was achieved.

We have investigated by AFM a series of control surfaces in order to validate the AFM images displayed in Figure II.2 for the Pt/PSI/$HOC_{11}S$/Au assembly. Figure II.3a displays PSI directly adsorbed to Au in the absence of the orienting hydroxyl-terminated SAM. For a PSI/Au substrate fewer PSI protein complexes are apparent than in the case of the PSI/$HOC_{11}S$/Au structure. This is reflected in the lower RMS amplitude of 3.13 nm for PSI/Au, as compared to the RMS amplitude of 4.27 nm for PSI/$HOC_{11}S$/Au (Figure II.2c). We have also photoreduced Pt directly on Au, and the data is shown in Figure II.3b. A limited number of areas where Pt was able to deposit can be identified and a roughness of 1.48 nm was determined. For another control we have platinized the $HOC_{11}S$/Au substrate in the absence of the PSI protein complex. There is little visual evidence of Pt on the surface of $HOC_{11}S$/Au and the recorded RMS amplitude was 1.76 nm. Figure II.3d presents the data for PSI randomly adsorbed

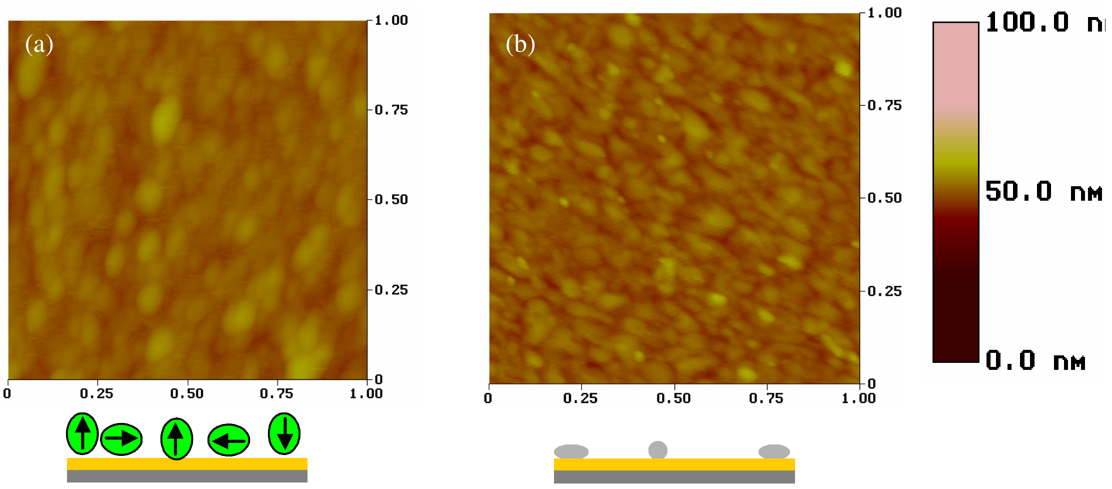

RMS – 3.13 nm: PSI adsorbed on Au

RMS – 1.48 nm: Pt photoreduced on Au

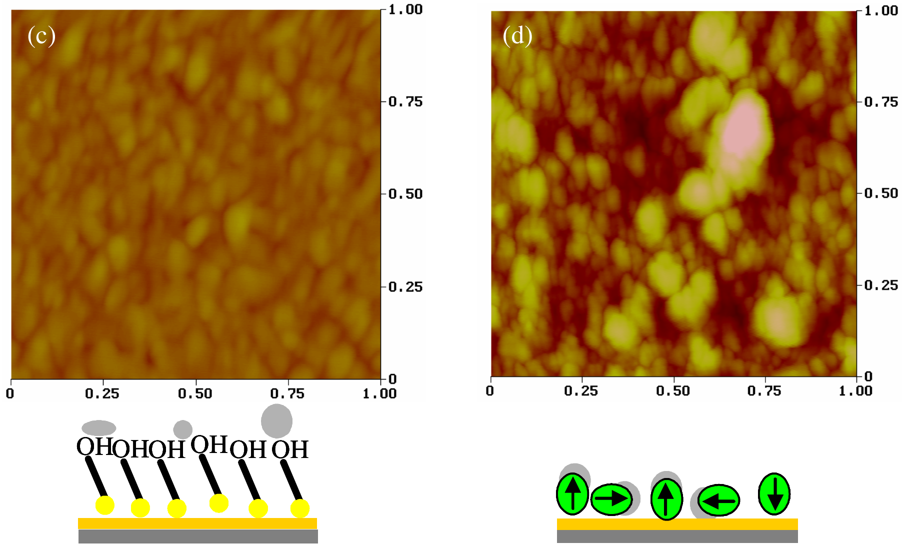

RMS – 1.76 nm: Pt photoreduced on HOC11S/Au

RMS – 7.15 nm: Pt photoreduced on PSI/Au

Figure II.3. AFM images for platinization on control surfaces contrast the AFM data recorded for the photoreduction of Pt onto the stromal side of PSI on $HOC_{11}S/Au$: (a) PSI adsorption on bare Au (PSI/Au) without a SAM for orientation exhibits a RMS amplitude of 3.13 nm; (b) Pt/Au substrate without PSI or $HOC_{11}SH$ results in a RMS amplitude of 1.48 nm; (c) platinization of $HOC_{11}S/Au$ without PSI for photoinitiated reduction yields a RMS amplitude of 1.76 nm; (d) Pt photoreduced onto PSI/Au without a SAM displays a RMS amplitude of 7.15 nm

onto the Au substrate followed by platinization. In this case, there is no SAM that would orient the PSI protein complex or help with the roughness reduction (as it was shown in Figure II.2b). The Pt/PSI/Au substrate results in a RMS amplitude of 7.15 nm. All four controls presented in Figure II.3 strengthen our claim that we have the ability to build the Pt/PSI/HOC$_{11}$S/Au structure, with the benefit of having metal connections on both active sides of the natural photodiode PSI.

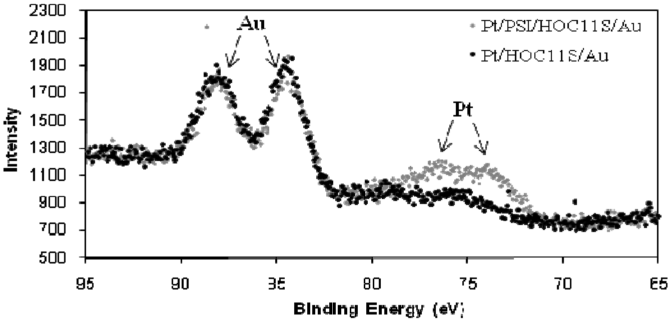

Figure II.4. XPS of platinized PSI (Pt/PSI/HOC$_{11}$S/Au in Fig. 2d) and control (Pt/HOC$_{11}$S/Au in Fig. 3c) was performed with an in-house built instrument using a Mg anode with a 60° emission angle and an 150 eV band width. The peaks at binding energies 88 eV and 84 eV are due to the Au substrate. The binding energy peaks at 76 eV and 74 eV result from the presence of Pt and they are very strong for the Pt/PSI/HOC$_{11}$S/Au structure (grey data points). XPS for Pt/HOC$_{11}$S/Au surface is denoted by black data points.

The AFM results were confirmed through XPS examination of two key substrates. The two spectroscopic scans shown in Figure II.4 are of the platinization of the HOC$_{11}$S/Au substrate with and without oriented PSI to photo-initiate the reduction of Pt. The black scanline in Figure II.4 is the XPS of the HOC$_{11}$S/Au surface platinized directly without the PSI to catalyze the reduction of $PtCl_6^{2-}$, corresponding to the AFM image in Figure II.3. The Pt/HOC$_{11}$S/Au surface shows the Au doublet at binding energies of 88 eV and 84 eV and small inflections where Pt peaks would be predicted, at binding energies of 79 eV and 76 eV. The incorporation of the PSI protein complex in the system in order to catalyze the photoreduction of Pt^{2+} ($Pt/PSI/HOC_{11}S/Au$ corresponding to the AFM image in Figure II.2d) shows an identical Au doublet when compared to the $Pt/HOC_{11}S/Au$ surface. However, the $Pt/PSI/HOC_{11}S/Au$ structure produces a distinguishable Pt doublet resulting from the Pt 4f electrons at binding energies of 76 eV and 74 eV (grey scan line). The results of the XPS study, along with the data obtained for topography by AFM, clearly confirm the photocatalytic properties of PSI oriented preferentially on a substrate to reduce Pt^{2+} ions. We are thus able to build the $Pt/PSI/HOC_{11}S/Au$ structure that has the advantage of presenting metal connections on both active sides of the natural photodiode PSI.

4. Conclusions

We have built a structure enclosing a natural photodiode, the PSI protein complex, establishing metal connections on each of the two active sides of the PSI. We have used AFM to investigate the topography of each layer used in the construction of the $Pt/PSI/HOC_{11}S/Au$ assembly, as well as the topography of control surfaces in order to insure that we have built the correct structure. We have employed XPS to validate the presence of the Pt on the final $Pt/PSI/HOC_{11}S/Au$ structure. This work represents an important step toward incorporating natural photodiodes in nano-circuits, as it establishes a method for connecting both sides of isolated PSI protein complexes that could be integrated into a pattern.

5. References

1. Blankenship, R. E., *Molecular Mechanisms of Photosynthesis*. Blackwell Science: Oxford, UK, 2002.

2. Wheeler, R. A., *Molecular Bioenergetics: Simulations of Electron, Proton and Energy Transfer*. The American Chemical Society: Washington, DC, 2004; Vol. 1.

3. Ort, D. R.; Yocum, C. F., *Oxygenic Photosynthesis: The Light Reactions*. Kluwer Academic Publishers: Boston, 1996; Vol. 4.

4. Bruton, T. M., *Renewable Energy* **1995,** *6* (3), 299-302.

5. Green, M. A., *Nanotechnol.* **2000,** *11*, 401-405.

6. Green, M. A., *Prog. Photovolt: Res. Appl* **2001,** *9*, 123-135.

7. Green, B. R.; Parson, W. W., *Light-Harvesting Antennas in Photosynthesis*. Kluwer Academic Publishers: Boston, 2003; Vol. 13, p 253-279.

8. Pessarakli, M., *Handbook of Photosynthesis*. second ed.; CRC Press: Boca Gaton, Fl, 2005.

9. Shiozawa, J. A.; Alberte, R. S.; Thornber, J. P., *Arch. Biochem. Biophys.* **1974,** *165*, 388-397.

10. Lee, I.; Lee, J. W.; Greenbaum, E., *Phys. Rev. Lett.* **1997,** *79* (17), 3294-3297.

11. Arnon, D. I., *Plant Physiol.* **1949,** *24* (1), 1-15.

12. Kranovsky, A. A.; Ni, C. V.; Nikandrov, V. V.; Brin, G. P., *Plant Physiol.* **1980,** *66*, 925-930.

13. Reeves, S. G.; Hall, D. O., *Higher Plant Chloroplasts and Grana: General Preparative Procedures (Excluding High Carbon Dioxide Fixation Ability Chloroplasts)*. Elsevier Inc: New York, 1980; Vol. 69, p 85 - 94.

14. Lee, I.; Lee, J. W.; Warmack, R. J.; Allison, D. P.; Greenbaum, E., *Proc. Natl. Acad. Sci. U. S. A.* **1995,** *92*, 1965-1969.

15. Lee, J. W.; Collins, R. T.; Greenbaum, E., *J. Phys. Chem. B* **1998,** *102(11)*, 2095-2100.

16. Ko, B. S.; Babcock, B.; Jennings, G. K.; Tilden, S. G.; Peterson, R. R.; Cliffel, D., *Langmuir* **2004,** *20* (10), 4033-4038.

17. Lee, J. W.; Lee, I.; Laible, P. D.; Owens, T. G.; Greenbaum, E., *Biophys. J.* **1995,** *69*, 652-659.

18. Kiley, P.; Zhao, X.; Vaughn, M.; Baldo Marc, A.; Bruce Barry, D.; Zhang, S., *PLoS Biol.* **2005,** *3* (7), e230.

19. Matsumoto, K.; Vaughn, M.; Bruce, B. D.; Koutsopoulos, S.; Zhang, S., *Journal of Physical Chemistry B* **2009,** *113* (1), 75-83.

20. Lee, J. W.; Lee, I.; Greenbaum, E., *J. Phys. Chem. B Lett.* **2005,** *109* (12), 5409-5413.

21. Lee, J. W.; Tevault, C. V.; Blankinship, S. L.; Collins, R. T.; Greenbaum, E., *Energy Fuels* **1994,** *8*, 770-773.

22. Allakhverdiev, S. I.; Kreslavski, V. D.; Thavasi, V.; Zharmukhamedov, S. K.; Klimov, V. V.; Nagata, T.; Nishihara, H.; Ramakrishna, S., *Photochem. Photobiol. Sci.* **2009,** *8* (2), 148-156.

23. Evans, B. R.; O'Neill, H. M.; Hutchens, S. A.; Bruce, B. D.; Greenbaum, E., *Nano Lett.* **2004,** *4* (10), 1815-1819.

24. Iwuchukwu Ifeyinwa, J.; Vaughn, M.; Myers, N.; O'Neill, H.; Frymier, P.; Bruce Barry, D., *Nat. Nanotechnol.* **2009,** *5* (1), 73-9.

25. Lubner, C. E.; Grimme, R.; Bryant, D. A.; Golbeck, J. H., *Biochemistry* **2010,** *49* (3), 404-414.

26. Lee, J. W.; Lee, I.; Greenbaum, E., *Biosens. Bioelectron.* **1996,** *11* (4), 375.

27. Terasaki, N.; Yamamoto, N.; Hiraga, T.; Yamanoi, Y.; Yonezawa, T.; Nishihara, H.; Ohmori, T.; Sakai, M.; Fujii, M.; Tohri, A.; Iwai, M.; Inoue, Y.; Yoneyama, S.; Minakata, M.; Enami, I., *Angew. Chem., Int. Ed.* **2009,** *48* (9), 1585-1587.

28. Terasaki, N.; Yamamoto, N.; Tamada, K.; Hattori, M.; Hiraga, T.; Tohri, A.; Sato, I.; Iwai, M.; Iwai, M.; Taguchi, S.; Enami, I.; Inoue, Y.; Yamanoi, Y.; Yonezawa, T.; Mizuno, K.; Murata, M.; Nishihara, H.; Yoneyama, S.; Minakata, M.; Ohmori, T.; Sakai, M.; Fujii, M., *Biochim. Biophys. Acta, Bioenerg.* **2007,** *1767* (6), 653-659.

29. Grimme, R. A.; Lubner, C. E.; Bryant, D. A.; Golbeck, J. H., *J. Am. Chem. Soc.* **2008,** *130* (20), 6308-6309.

30. Grimme, R. A.; Lubner, C. E.; Golbeck, J. H., *Dalton Trans.* **2009,** (45), 10106-10113.

31. Terasaki, N.; Yamamoto, N.; Hiraga, T.; Sato, I.; Inoue, Y.; Yamada, S., *Thin Solid Films* **2006,** *499* (1-2), 153-156.

32. Ciobanu, M.; Kincaid, H. A.; Jennings, G. K.; Cliffel, D. E., *Langmuir* **2005,** *21* (4), 692-698.

33. Ciobanu, M.; Kincaid, H. A.; Lo, V.; Dukes, A. D.; Jennings, G. K.; Cliffel, D. E., *J. Electroanal. Chem.* **2007,** *599*, 72-78.

34. Kincaid, H. A.; Neidringhaus, T.; Ciobanu, M.; Cliffel, D. E.; Jennings, G. K., *Langmuir* **2006,** *22* (19), 8114-8120.

35. Faulkner, C. J.; Lees, S.; Ciesielski, P. N.; Cliffel, D. E.; Jennings, G. K., *Langmuir* **2008,** *24(16)*, 8409-8412.

36. Fotiadis, D.; Muller, D. J.; Tsiotis, G.; Hasler, L.; Tittmann, P.; Mini, T.; Jeno, P.; Gross, H.; Engel, A., *J. Mol. Biol.* **1998,** *283* (283), 83-94.

37. Frolov, L.; Wilner, O.; Carmeli, C.; Carmeli, I., *Adv. Mater.* **2008,** *20*, 263-266.

38. Gao, J.-S.; Arunagiri, T.; Chen, J.-J.; Goodwill, P.; Chyan, O.; Perez, J.; Golden, D., *Chem. Mater.* **2000,** *12* (11), 3495-3500.

39. Hills, C. W.; Mack, N. H.; Nuzzo, R. G., *J. Phys. Chem. B* **2003,** *107* (12), 2626-2636.

40. Fu, X.; Wang, Y.; Wu, N.; Gui, L.; Tang, Y., *J. Colloid Interface Sci.* **2001,** *243*, 326-330.

41. Lee, I.; Lee, J. W.; Stubna, A.; Greenbaum, E., *J. Phys. Chem. B* **2000,** *104* (11), 2439-2443.

42. Baba, K.; Itoh, S.; Hastings, G.; Hoshina, S., *Photosynth. Res.* **1996,** *47* (121-130).

CHAPTER III

Immunosensor Development for the Detection of Respiratory Syncytial Virus on the Quartz Crystal Microbalance Platform[1]

1. Introduction

Respiratory syncytial virus (RSV) is the most common cause of bronchiolitis and pneumonia among infants and children under 1 year of age.[1,2] Communities around the world report annual outbreaks of infection from the late fall until early spring and RSV is estimated to be responsible for 65 million infections of which 1 million result in death annually.[3] In spite of a continuing research effort, there is no vaccine available for the prevention of RSV infection.[1,4,5]

Palivizumab (Synagis®) is the first and only commercialized monoclonal antibody to be approved for prevention of an infectious disease in children to date.[6] It is a humanized monoclonal antibody ($IgG_{1\kappa}$), which is produced by recombinant DNA technology and directed to an epitope in the A antigenic site of the F protein of respiratory syncytial virus (RSV). Palivizumab is a composite of human (95 %) and murine (5 %) antibody sequences. The human heavy-chain sequence was derived from the constant domains of human IgG_1 and the variable framework regions of the V_H genes C_{or} and C_{ess}.[7,8] The human light-chain sequence was derived from the constant domain of C_κ and the variable framework regions of the V_L gene K104 with Jκ-4.[9] The murine sequences were derived from a murine monoclonal antibody, Mab 1129,[4] in a process that involved the grafting of the murine complementarity determining regions into the human antibody frameworks. Palivizumab is composed of two heavy chains and two light chains and has a molecular weight of approximately 148 kD.

---

[1] This Chapter has been formatted for submission to Biosensors and Bioelectronics. The authors of the paper are: Y. Zhang, M.L. Krim, E.L. Bentzen, B. Turner, D. Wright, D.E. Cliffel.

Ribavirin is an antiviral drug that is currently available for the treatment of RSV, but it is effective only when given early in the course of the infection, and is only helpful for a fraction of patients.[10-12] To have the possibility of providing early treatment an accurate and timely assay for the detection of RSV is required.

A number of techniques have been reported for detection and quantification of RSV including enzyme linked immunosorbant assay (ELISA),[13-15] cell culture,[16] immunofluorescence,[17,18] radioimmunoassay,[19] and reverse transcription-polymerase chain reaction (RT-PCR).[20-22] Although these assay techniques are very sensitive, they are often expensive, laborious, and hazardous due to the presence of radiation. They require specific labels for detection purposes making them complex and time-consuming. The standard assays for clinical RSV detection in nasal secretions are cell culture, real-time PCR and rapid ELISA-based assay. Cell culture is a time consuming process which requires training, and takes days to generate results. Real-time PCR requires a few hours to detect the viral nucleic acid; however, this technique requires technical expertise and suffers from a high false positive rate due to DNA contamination.[23-25] Additionally, it requires an expensive instrumentation platform which consists of thermal cycler, computer, optics for fluorescence excitation, and emission collection for data acquisition, all of which inhibit the utilization in a point-of-care clinical setting. ELISA is one of the most common antibody based molecular recognition assays for clinical laboratories, but the requirements of many clinical applications where speed and throughput are critical parameters have exceeded the capability of traditional plate-based ELISA instrumentation. Automated systems have overcome these limitations in large hospital settings and can process hundreds of samples per hour.[26,27] However, large integrated ELISA systems are not practical for point-of-care clinical applications, where cost and space become prohibitive factors.[15]

Quartz crystal microbalance (QCM) is a fast, cheap, safe and portable technique and thus it presents itself as an attractive solution to the problems associated with the RSV detection. The price for the QCM platform ranges between $3000 and $5000. Additionally, QCM immunosensors are highly sensitive transducer devices based on the measurement of frequency changes of the piezoelectric crystal caused by the variations in mass due to specifically bound molecular targets. The QCM platform has the capability to detect nanogram changes in mass.[28] The detection of a virus will occur in minutes due to the fast reaction kinetics and the high affinity for antibody-antigen binding.

The relationship between the change in mass, Δm [ng], and the resulting change in frequency, ΔF [Hz], and was originally developed for the gas phase, and is given by the Sauerbrey equation:[29]

$$\Delta F = -2F_o^2 \Delta m / \left[A\,(\mu_q \rho_q)^{1/2}\right] \qquad [1]$$

where F_o is the fundamental resonant frequency, μ_q is the shear modulus of quartz (2.947×10^{10} kg m^{-1} s^{-2}), ρ_q is the density of quartz (2648 kg m^{-3}) and A [m^2] is the active area. In liquids, the frequency change of the crystal depends heavily on the density and viscosity of the solution. The relationship between the oscillation frequency change of a quartz resonator in contact with a liquid and the accumulated mass was first described by Kanazawa and Gordon who derived Equation (2);[30] Thompson *et al.* also reviewed the details of the characteristics of QCM in the liquid phase.[31]

$$\Delta F = -F_o^{3/2}\left[\rho_1 \eta_1 / (\pi \rho_q \mu_q)\right]^{1/2} \qquad [2]$$

where ρ_1 [kg m^{-3}] is the density solution, and η_1 [kg m^{-1} s^{-1}] is the viscosity of solution. Due to the difficulty in acquiring the change of density and viscosity at the interface between the solution and the quartz crystal during an experiment, the quantification of the mass change in solution is still not straightforward. We have reported a method to calibrate the change in frequency as a function of the change in resistance based on the fact that the interface resistance change is proportional to the change of viscosity and density at the interface of quartz.[32]

The high sensitivity of the technique and the relationship between mass and frequency make the QCM ideal for sensing applications through changes in adsorbed mass. QCM has lead to a wide range of research and applications in gas phase detection,[33,34] immunosensors,[35-39] DNA biosensors,[40,41] and drug analysis.[42] We have recently demonstrated that QCM can be used for the detection of a peptide using a specific epitope presentation on monolayer protected nanoclusters and we have presented the corresponding kinetic studies for different peptides, including anthrax bacterium, Ebola virus and the flu virus.[43,44]

Here we present a flow type QCM immunosensor for real-time detection of RSV, which addresses some of the deficiencies currently associated with the early detection of RSV. QCM exhibits inherent positive attributes, such as high sensitivity, specificity, low cost, near real-time output, and ease of operation. In our study, the continuous operation of the system was employed instead of the dip-and-dry[45] and aerosol[39] methods which are not as reliable because of the complexity in handling samples, sources of errors, and lack of automation or continuous operation.

2. Materials and Methods

A. Reagents. Protein G (23 kDa) was purchased from Southernbiotech (Birmingham, Alabama, Cat#: 7400-01L). RSV monoclonal antibody (palivizumab (Synagis®), 150 kDa) was a gift from the James E. Crowe lab in Vanderbilt Medical Center. Phosphate-buffered saline (PBS) is composed of 150 mM sodium chloride (NaCl, Fisher Scientific) and 50 mM monosodium phosphate (NaH_2PO_4, Fisher Scientific). The pH was adjusted to 7.1 (Denver Instrument, pH meter model 250) by adding concentrated sodium hydroxide (NaOH, EM Science). RSV was harvested using cell culture by infecting Madin-Darby canine kidney (MDCK) cells in the Opti MEM media (Gibco) maintained at 37 ^{o}C in an incubator for 3-4 days. Bovine serum albumin (BSA) was purchased from Sigma-Aldrich. All deionized water was purified using a Modulab Water Systems unit (~18 MΩ). Affinity-purified anti-hemagglutinin (anti-HA) and anti-*Bacillus anthracis* protective antigen (anti-PA) were purchased from Bethyl Labs, metapneumovirus (MPV) was a gift from Professor John William of Vanderbilt University Medical Center.

B. Atomic Force Microscopy (AFM). AFM analysis of all of the samples was performed on a Digital Instruments (a division of Veeco Instruments Inc.) multimode AFM, the Nanoscope IIIa scanning probe microscope controller was used in cooperation with the proprietary Nanoscope III, version 4.43R8, software for control of the AFM tip and imaging parameters. Silicon tips were purchased from Budget Sensors (Sofia, Bulgaria). Double sided tape was used to adhere the sample to be imaged. All imaged areas were 1 μm side squares with a z-axis range of 50 nm. The imaging speed was 1 μm s^{-1}.

C. Ellipsometry. The thickness of each immobilized layer was examined using a J. A. Woollam Co., Inc. ellipsometer M-2000V™, equipped with a 50 W quartz tungsten halogen lamp as light source (in the range of λ = 370-1000 nm with a step size of $\lambda \simeq 1.6$ nm). The Ψ (λ) and $\Delta(\lambda)$ were collected through three angles of incidence, 65°, 70°, and 75°. The fitting process was performed using Wvase32 software.

D. QCM. The QCM instrument and crystals were purchased from MAXTEK (Cypress, CA). QCM crystals consist of an AT cut quartz crystal initially coated with ~80 nm Ti, and subsequently with a 340 nm gold film deposited by physical vapor deposition. The original frequency of the crystal in air is 5 MHz and the active area is 0.3419 cm^2. The crystal was positioned inside a flow cell with a 100 μl volume and a peristaltic pump purchased from MaterFlex forced the solution through the cell over the exposed active area of the crystal. The gold surface was cleaned with piranha solution (3:1 concentrated H_2SO_4 to 30 % H_2O_2; CAUTION – piranha solution is hazardous and should be handled with adequate protective equipment!) at least 5 times for ~ 1 minute each time, followed by rinsing with copious amounts of water and drying under N_2 gas. The crystal was then placed in a Teflon flow cell (100 μl total volume). The crystal was exposed constantly to the reagents through the use of a peristaltic pump. The flow rate used was 20 µl min^{-1}. To initiate every experiment, PBS was flown over the crystal until a stable baseline was produced (the variation in frequency was less than 0.3 Hz min^{-1}). The frequency and resistance changes were recorded simultaneously and continuously during each step. The frequency change was converted to mass change using the method previously described.[32]

E. Immunosensor for RSV Detection. The timeline used for assembling and testing the immunosensor used for RSV detection is presented in Table III.1. The initial concentration of the RSV sample harvested from the cell culture in growth media was 8×10^6 pfu ml^{-1}. PBS was used for dilution to prepare the samples with lower concentrations of RSV. Clinical nasal-wash samples were collected on healthy people in the Vanderbilt University Medical Center. Nasal-wash samples containing RSV were prepared by adding specific aliquots of RSV obtained from cell culture.

F. ELISA for RSV Detection. A standard indirect-sandwich ELISA was conducted on Immulon 2HB microtiter plate. RSV with concentrations of 0 pfu ml^{-1}, 1×10^2 pfu ml^{-1}, 1×10^3 pfu ml^{-1}, 1×10^4 pfu ml^{-1}, 1×10^5 pfu ml^{-1}, 1×10^6 pfu ml^{-1} in PBS buffer were prepared from a stock solution of RSV at 8×10^6 pfu ml^{-1}. Three RSV samples were prepared in parallel for each concentration and the plate was incubated at 37 ^{o}C for 1h. After the 1 hour incubation period, the wells were rinsed 5 × 300 µl with PBS solution and blocked using 2 % BSA 300 µl. The

Table III.1 – Timeline and sequence for assembling and testing the QCM immunosensor for RSV detection.

Sequence #	Solution flown over QCM crystal	Immunosensor type			
		Protein G		Protein A	
		Concentration	Time [min]	Concentration	Time [min]
1	PBS	150 mM NaCl & 50 mM NaH_2PO_4	10	150 mM NaCl & 50 mM NaH_2PO_4	10
2(i)	Protein G	200 µg ml^{-1}	10	-	-
2(ii)	Protein A	-	-	200 µg ml^{-1}	10
3	PBS	150 mM NaCl & 50 mM NaH_2PO_4	10	150 mM NaCl & 50 mM NaH_2PO_4	10
4	BSA	1 mg ml^{-1}	10	1 mg ml^{-1}	10
5	PBS	150 mM NaCl & 50 mM NaH_2PO_4	10	150 mM NaCl & 50 mM NaH_2PO_4	10
6	Palivizumab	40 µg ml^{-1}	10	40 µg ml^{-1}	10
7	RSV	8 x10^{-5} pfu ml^{-1}	10	8 x10^{-5} pfu ml^{-1}	10
8	PBS	150 mM NaCl & 50 mM NaH_2PO_4	10	150 mM NaCl & 50 mM NaH_2PO_4	10

plate was put back in the incubator at 37 ^{o}C for 1h, and then washed 5 × 300 µl with PBS solution. First, 100 µl of the antibody Palivizumab at a concentration of 10 µg/ml was introduced to each well, and the wells were incubated at 37 ^{o}C for 1 h, and then washed 5 × 300 µl with PBS solution. Second, 100 µl of antihuman horseradish peroxidase (HRP) labeled antibody (1:50000) diluted with PBS buffer was added in each well. Then the plate was incubated at 37 ^{o}C for 1 hour. After

1h, it was washed 5 × 300 µl with PBS solution and 100 µl of tetramethylbenzidine solution was added. After 10 minutes, 100 µl 2 M sulfuric acid was added in every well to quench the enzymatic reaction. Finally, the absorbance at 450 nm was measured using a Bio-Tek synergy HT microplate reader.

3. Results and Discussion

We have assembled a quantitative immunosensor for RSV detection on a Au-coated QCM crystal by sequentially layering protein G, BSA and Palivizumab, as outlined in Table III.1 and as can be seen illustrated in Figure III.1. Protein G, a bacterial cell wall protein isolated from group G streptococci, is a good substrate for immobilizing most antibodies including all human immunoglobulin IgG_{1-4} and mouse immunoglobulin IgG_{1-3}.[46-50] Protein G was passed over the quartz crystal and bound to the gold. The binding sites became saturated when a plateau was observed and the excess protein G was washed away with PBS for 10 minutes, step 3 in Table III.1. The free gold sites were then backfilled using BSA (step 4) to avoid nonspecific binding in subsequent steps. PBS was then used to rinse the excess BSA off the crystal for 10 minutes (step 5). Subsequently, the RSV antibody was immobilized by flowing Palivizumab over the protein G layer for 10 minutes (step 6). Any nonspecifically bound Palivizumab was rinsed away with PBS for 10 minutes. The RSV samples in growth media were then introduced to the immunosensor (step 7) followed by a PBS rinse (step 8).

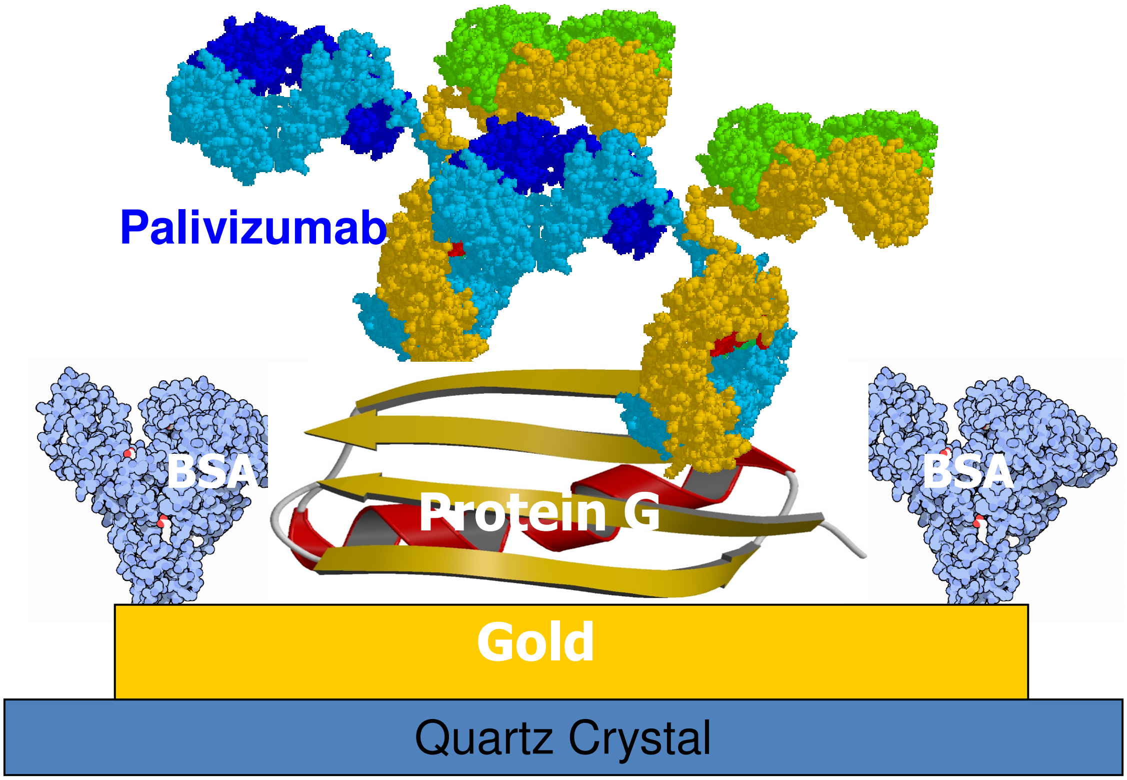
Palivizumab
BSA
Protein G
BSA
Gold
Quartz Crystal

Figure III.1 – Immunosensor for RSV detection built on a QCM crystal with protein G as the initial layer on Au, followed by BSA blocking of bare Au and finally Palivizumab.

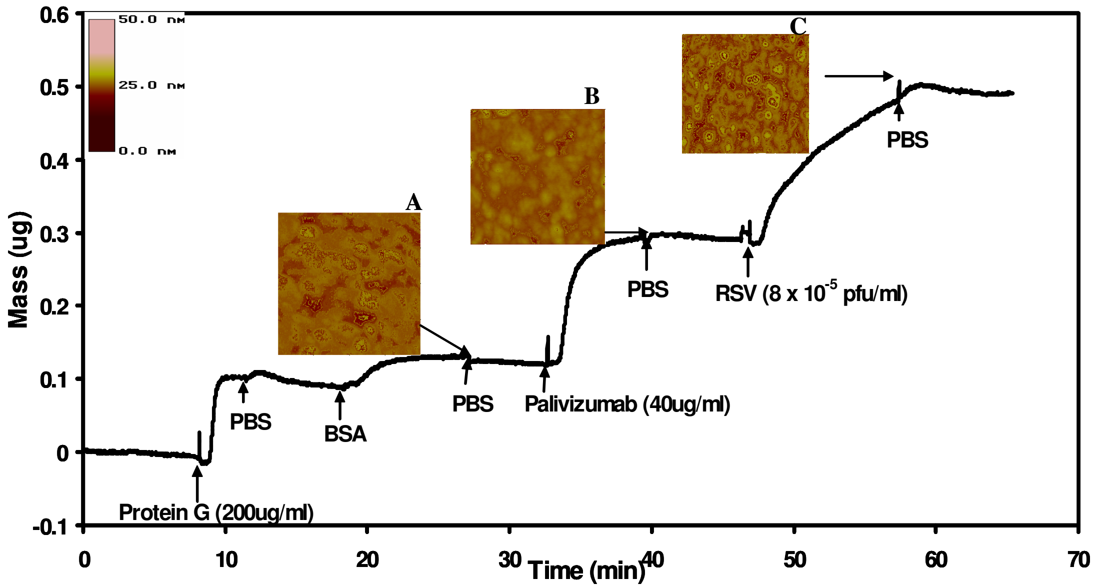

Figure III.2 – QCM run displaying the steps required for the assembling and testing of the RSV immunosensor, with the sequential formation of the following layers: protein G, BSA, Palivizumab (antibody). The last step corresponds to the testing of the immunosensor, displaying the RSV binding. Panels A,B, and C are the AFM images of the QCM crystal during various stages of immunosensor assembly: A) BSA/protein G/Au; B) Palivizumab/BSA/protein G/Au; C) RSV/Palivizumab/BSA/protein G/Au. All AFM images are 1 µm x 1 µm.

Figure III.2 displays a typical example of QCM processed data for assembling the immunosensor and the subsequent testing for RSV detection. There is a delay time of ~ 1 min after the introduction of each solution before a substantial mass change occurs. The switching of the solutions might cause a change in fluid pressure, which results in a temporary spike in the QCM frequency and this is an artifact on the gravimetry curve. The binding of protein G and Palivizumab was rapid; over 75 % of the binding was completed in 2-3 min ($\Delta m = 100 \pm 6$ ng min^{-1} for protein G and $\Delta m = 67 \pm 4$ ng min^{-1} for Palivizumab, average values for 10 binding curves) and the change in mass with time was almost linear indicating a mass transfer-controlled binding process. After a couple of minutes of rapid mass change, the binding rate decreased, and saturation was reached after ~ 10 min of exposure to a particular solution ($\Delta m < 0.3$ ng min^{-1} after 10 min). As the flux of RSV species to the QCM surface was constant during flow, the decrease in binding rate indicated that specific surface processes were occurring.[51] It is possible that the steric hindrance limits the access of the bio-species to the surface and the number of subsequent binding events decreased rapidly with increasing surface coverage. Due to the high affinity constant, $K_a \approx 10^9$ - 10^{10} M^{-1},[47] between binding domains on protein G and the F_c region of Palivizumab, the antibody remains bound and dissociation during subsequent steps is negligible.

The binding of Palivizumab to protein G resulted in a mass gain of 329 ± 22 ng (average of 19 runs). Protein G has 2 binding domains available for the F_c region of the antibody.[52] According to the literature,[53,54] the diameter of protein G is 2.2 nm. The three dimensional parameters for Palivizumab are 14 nm x 9 nm x 5 nm. We used 9 nm as the average diameter of Palivizumab. Assuming spherical shape proteins, the expected mole ratio of protein G to Palivizumab should be 1:0.13. The experimental mole ratio of protein G to Palivizumab was 1:0.17 (protein G: 23 kDa; Palivizumab: 150 kDa). The experimental mole ratio corresponds well to the theoretical mole ratio. The discrepancy between the theoretical and experimental mole ratio can be easily explained by a tighter packing of the oblong shaped Palivizumab.

Experimentally, 299 ± 35 ng of protein G was bound to the crystal and this translates into a packing efficiency of 86 ± 10 %, assuming a spherical protein G shape and accounting for the active area of the quartz crystals that were used (0.3419 cm^2). Theoretically, the most efficient packing in 2D is the hexagonal model for spherical molecules with closely packed spheres at a packing efficiency (PE) of 81 %. While the theoretical PE (81 %) was lower than the experimental PE (86 %) for protein G, it was within the limits of error for the measurement (± 10 %). Both the ellipsometry and the AFM data (Table III.2) support the statement that a full monolayer of protein G is formed. Additionally, the QCM data for blocking free gold sites by BSA upon immobilization of protein G yielded a mass change of 15 ± 10 ng which is consistent with the calculated

Table III.2 – The roughness and thickness of the layers required for the assembly and testing of the RSV immunosensor, as measured by AFM and ellipsometry (SD = standard deviation)

	Diameter [Å]	AFM		Ellipsometry	
		Roughness [nm]	SD [nm]	Thickness [Å]	Relative SD [Å]
Bare gold	1.4	1.91	0.33	-	-
Protein G	22[a]	1.55	0.25	24.1	1.1
Palivizumab	60-140	1.49	0.23	14.0	0.3
RSV	1200-3000[b]	2.93	0.37	22.3	1.2

a) Sauer-Eriksson, Kleywegt et al. 1995; b) CDC 2005 packing efficiency of protein G. If BSA is adsorbed directly onto the gold without protein G first, the mass increase for a full monolayer of BSA becomes 150 ± 16 ng. This indicates that the BSA adsorption onto the protein G/Au substrate covered ~ 10 % of the entire surface, a value consistent with the gold surface that remains uncovered subsequent to protein G adsorption.

We have explored an alternate method for the immobilization of antibodies by using protein A instead of protein G (Figure III.3). The choice of protein G for the immunosensor architecture was based on the fact that protein G, a cell wall component produced by several strains of staphylococcus, has greater affinity than protein A for most mammalian IgGs.[46,47] Figure III.3 displays a typical example of QCM processed data for assembling the immunosensor based on protein A and the subsequent testing for RSV detection. The immunosensor built on protein A did not successfully perform stable detection for RSV, indicating that protein A did not irreversibly bind and beneficially orient the RSV antibody (Palivizumab). When RSV was presented to the surface of the crystal that used protein A in the attachment sequence, the sensor did not behave like the one built on protein G. In the case of protein G, the mass change due to RSV binding continually increased with RSV flowing over the immunosensor in the first 20 minutes (Figure III.2). In the case of protein A (Figure III.3), there was a sharp decrease in mass after the first 2-3 min of exposure to RSV. This was probably due to weaker binding between protein A and Palivizumab compared to the

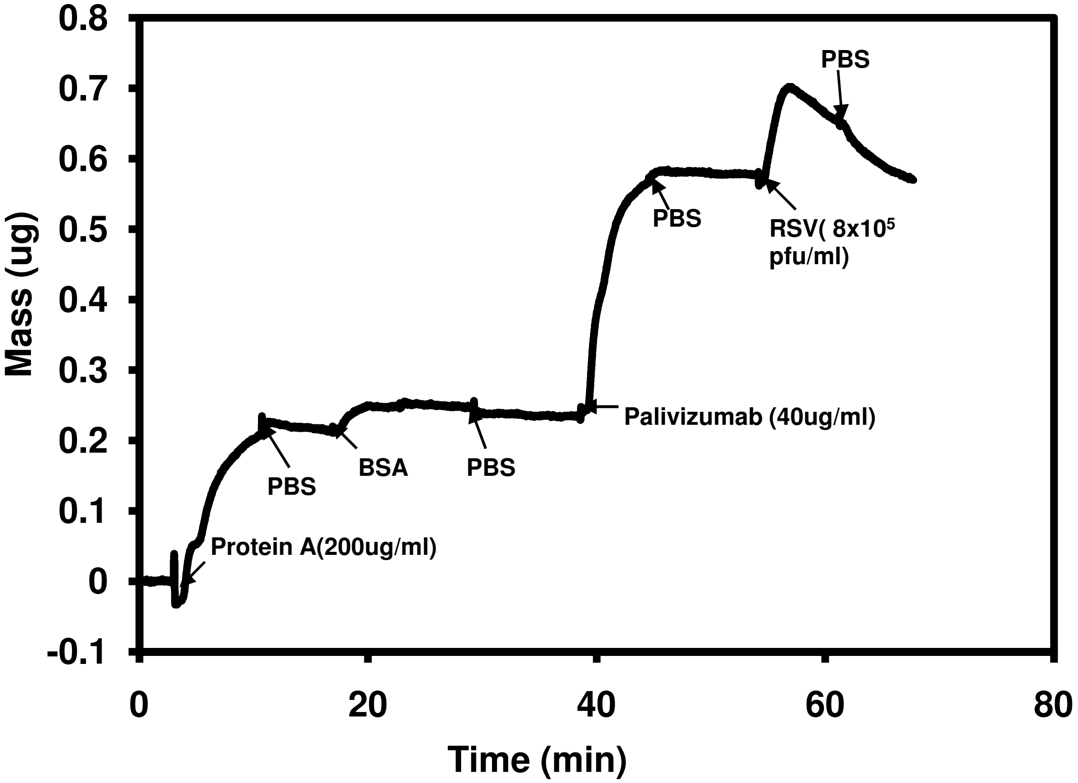

Figure III.3 - QCM run displaying the steps in the assembling and testing of a control of the RSV immunosensor, designed to probe the Palivizumab binding to protein A. This is done with the sequential formation of the following layers: protein A, BSA, and Palivizumab (antibody). The last step corresponds to the testing of the immunosensor, and it indicates that RSV does not bind strong enough to the immunosensor based on protein A in order for the sensor to be suitable for RSV detection.

binding between protein G and Palivizumab. The data in Figure III.3 displays an RSV exposure time of ~ 7 min. However, when the RSV exposure time was extended over 40 min (Supporting Information, Figure III.S.1), a slow and continual decline in mass was observed until the mass gain plot crossed the baseline recorded after antibody binding, indicating that the stripping of the antibody occurred. The difference in binding strength between protein A versus protein G with respect to Palivizumab can be explained by the different mechanisms of attachment for each protein to the Fc region of the antibody. The interface between the Fc region and protein G consists of an intricate network of hydrogen bonds and salt links, involving mainly charged and polar residues and the occasional main-chain atom. The complex between the Fc region of the Palivizumab antibody and protein A consists of mainly hydrophobic interactions, with few polar contacts resulting in a weak and reversible attachment.[54]

The topography of each layer formed during the construction of the immunosensor was examined *ex situ* applying tapping mode AFM, and the corresponding images are shown in Figure III.2. For the AFM data presented in both Figure III.2 and Table III.2 there was no discernable difference between imaging the protein G/Au layer or the BSA/protein G/Au layer. Panel A, from Figure III.2, displays discernable protein G molecules on the Au substrate. Protein G can be observed as an aggregated pattern in a solid-like state, exhibiting a random cloud-like structure, which is in agreement with the literature.[55] Similar patterns were observed for the Palivizumab and RSV layers, as shown in panels B and C in Figure III.2, respectively. Table III.2 summarizes the surface roughness of each layer. The roughness of the Au surface (1.91 ± 0.33 nm) was decreased after protein G immobilization (1.55 ± 0.25 nm), probably because the small protein molecule was able to pack densely and homogeneously onto the gold surface. The topography of the Palivizumab layer (1.49 ± 0.23 nm) was similar to the protein G layer. However, upon RSV binding there was dramatic increase in surface roughness (2.93 ± 0.37 nm), which could be caused by the larger size of RSV and its irregular shape when compared to protein G and Palivizumab: 120-300 nm diameter for RSV, versus 2.2 nm for protein G and ~9 nm for Palivizumab.[3,53,54]

We have measured the thickness of each biolayer (Protein G, Palivizumab and RSV) adsorbed on the quartz crystal via ellipsometry. The results from the ellipsometry measurements of each layer are summarized in Table III.2. The optical ellipsometric characterization yielded film thicknesses of 24.1 ± 1.1 Å for protein G, 14 ± 0.3 Å for Palivizumab , and 22.3 ± 1.2 Å for RSV. The fitting process of the data obtained for each of the three layers was assumed to follow the Cauchy dispersion model, which was used to describe the dispersion of the index of refraction of materials in spectral ranges in which the given material was transparent.[56] The thickness of the protein G layer was 24.1 Å and matched well with the diameter of protein G (22 Å), indicating a single monolayer of protein G uniformly bound to the gold surface. The results obtained for the second layer (Palivizumab) for the third layer (RSV) were different, in that the diameter of the adsorbed biomolecule and the thickness of the adsorbed layer were dissimilar. This apparent discrepancy in surface thickness between the ellipsometry measurements and expected results is not incompatible with the claim, that the biomolecules have indeed adhered to the QCM crystal. This discrepancy is most likely caused by the difference in 2D packing density of protein G, Palivizumab and RSV, 2.20 x 10^{13} molecules cm^{-2} (protein G), 3.86 x 10^{12} molecules cm^{-2} (Palivizumab), 8.04 x 10^{9} molecules cm^{-2} (RSV) (Note: The calculations are based on the above report of 299 ng protein G, 329 ng Palivizumab and 210 ng RSV absorption in a 0.3419 cm^{2} active area). These numbers translate into the following packing efficiencies: 86 % for protein G, 109 % for Palivizumab, and 93 % for RSV. Accounting for the measurement errors, these numbers show that every step of the assembly and/or testing for the immunosensor creates a monolayer of protein G, Palivizumab, and RSV, respectively. Also, the calculations assumed spherical proteins, which introduce errors in the calculated PEs. The larger diameter for the Palivizumab and RSV, compared to protein G, leads to a heterogeneous surface, which might result in the differences between the thickness and size of the Palivizumab and RSV layers, because light scattering and polarization change cannot be modeled and fit properly on a heterogenenous surface using the designed software. Additionally, one can see qualitatively in the AFM images in Figure III.2 that surfaces are not flat.

The specificity of the immunosensor for RSV detection was assessed through a series of control experiments. Anti-HA and anti-PA, which are antibodies of influenza and anthrax, respectively, replaced Palivizumab as the antibody in the

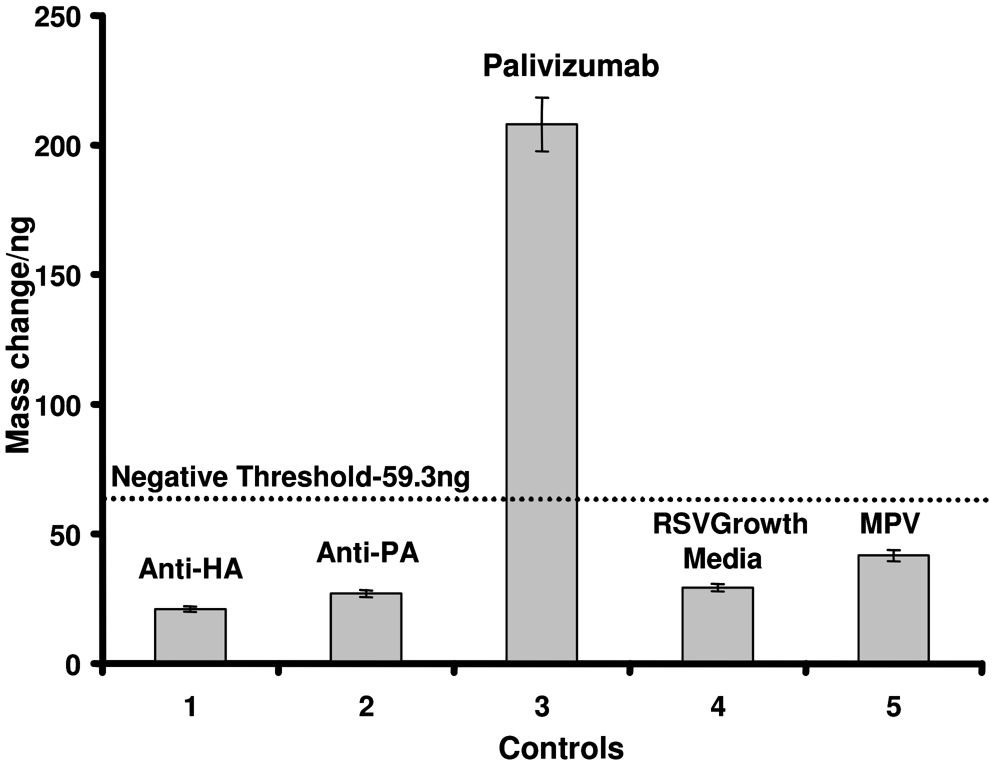

Figure III.4 - Mass change for various control experiments compared to RSV (8 × 10^5 pfu ml^{-1}) binding, x-axis: (1) Anti-HA was substituted for Palivizumab and then RSV (8 × 10^5 pfu ml^{-1}) was flown through; (2) Anti-PA was substituted for Palivizumab and then RSV (8 × 10^5 pfu ml^{-1}) flown through; (3) typical RSV (8 × 10^5 pfu ml^{-1}) binding on Palivizumab (RSV antibody); (4) nonspecific binding of RSV growth media on Palivizumab; (5) nonspecific binding between MPV and Palivizumab.

control experiments. RSV growth media and MPV, a virus that belongs to the same sub-family as RSV, were used as antigen controls. The QCM immunosensor exhibited negative responses in all control experiments as can be observed in Figure III.4. The threshold (59 ng) was defined as the mass change in RSV growth media plus 3 times its standard deviation for the RSV growth media. For the cases when the mass change was less than the defined threshold, the response was considered negative. Consequently, RSV can be specifically detected with the QCM-based immunosensor since the all control experiments provided negative results.

Live RSV-infected MDCK cells were employed on the QCM immunosensor to evaluate the feasibility of RSV detection of cellular infection in the presence of a real biological sample. We have tested uninfected cells (sample 1), infected cells (sample 2), supernatant (sample 3) and ghost membranes of infected cells (sample 4). The supernatant comes from centrifuging the mixture of media and infected MDCK cells. The results are summarized in Figure III.5. The uninfected MDCK cells - sample 1 exhibited the lowest mass gain (70 ± 10 ng) compared to the other three samples, and it was likely that this mass change resulted from nonspecific binding between Palivizumab and the biological tissue. The other

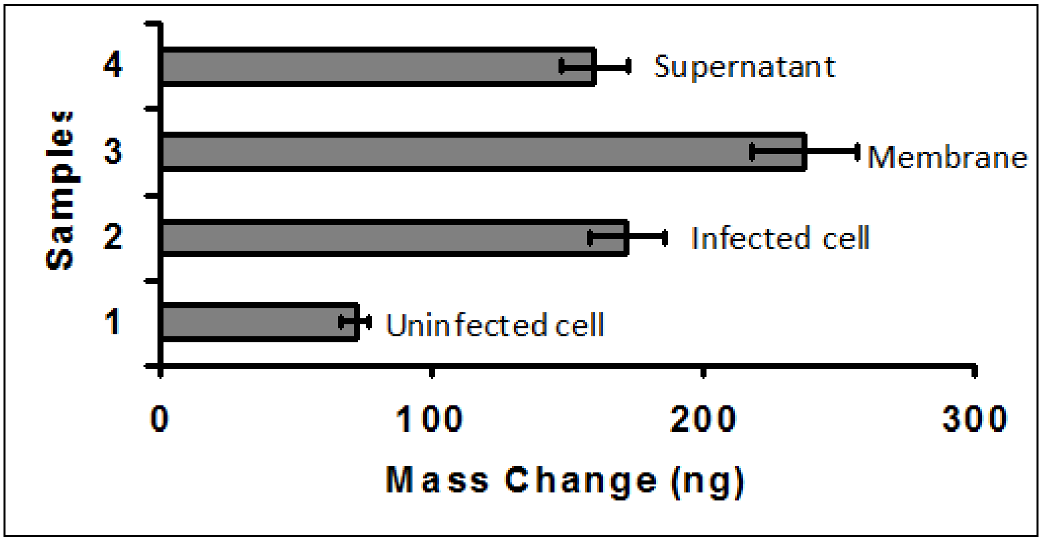

Figure III.5 - Evaluation of the RSV immunosensor performance by using infected cells: (1) uninfected MDCK cells (control); (2) infected MDCK cells; (3) ghost membranes of infected MDCK cells; (4) supernatant from centrifuging mixture of media and infected MDCK cells.

three samples showed specific binding with Palivizumab. According to the replication cycle of RSV,[18,57] there will be some RSVs in the culture medium resulting from completed replication; these RSVs leave the host cell and enter the supernatant. Thus, the supernant showed a specific binding with Palivizumab (160 ± 11 ng). Our immunosensor also showed detection of virions which were assembled by newly produced viral proteins and genomic RNA molecules and budded from the surface (membrane) of the infected cells in samples of infected cells (172 ± 12 ng) and samples of ghost membranes of infected cells (137 ± 14 ng).

A concentration dependence experiment was performed in the range of 8×10^4 - 8×10^5 pfu ml^{-1}. As shown in Figure III.6, Palivizumab becomes saturated with RSV above 5×10^5 pfu ml^{-1} within 10 minutes. Figure III.6 shows the plot of RSV mass change (Δm) versus the concentration (C) in the linear binding region for a 10 min exposure time. Linear correlation of $\Delta m = (31 \pm 4.2)C + (54 \pm 11)$, $R^2 = 0.9643$ was given in the range of 8×10^4 – 5×10^5 pfu ml^{-1} in PBS, with a detection limit of 9×10^3 pfu ml^{-1}, estimated according to the 3σ (standard deviation) rule. This detection limit is in the same range as the detection limit from the ELISA experiments, about 2×10^3 pfu ml^{-1}. There are several possibilities for further improvement of the detection limit. One way would be by increasing the number of interaction sites on the QCM crystal. To achieve this, protein G could be attached onto the gold substrate by covalent binding which in turn

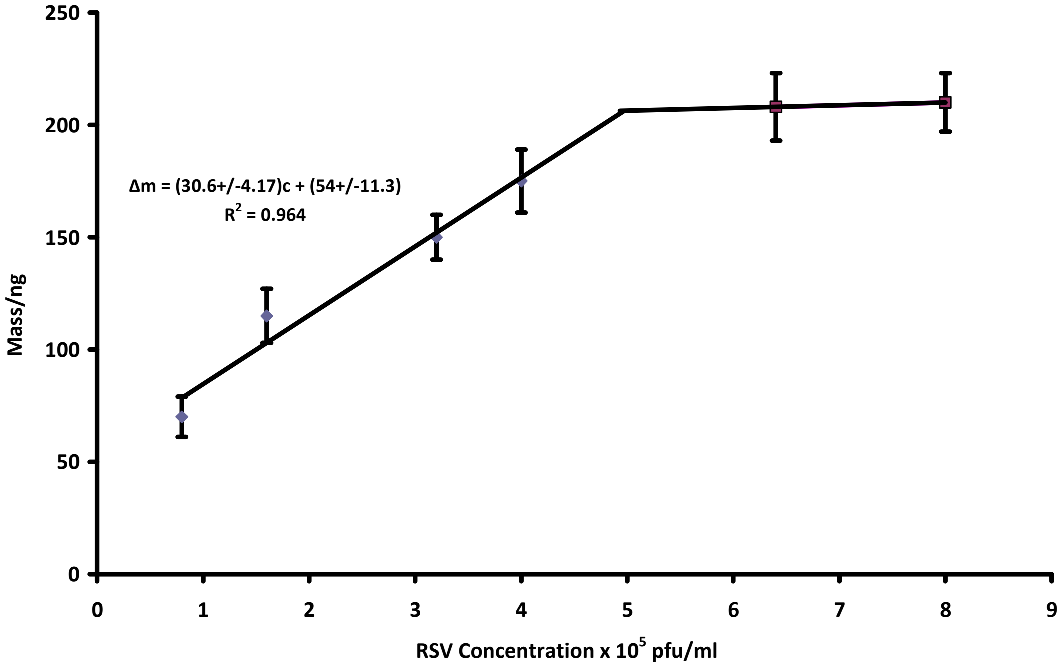

Figure III.6 - RSV concentration dependence experiments, RSV in PBS in the range of 8×10^4 pfu ml^{-1} - 8×10^5 pfu ml^{-1}. The sensor reaches saturation around 5×10^5 pfu ml^{-1}. Three replicates were performed for each concentration.

would increase the binding efficiency, subsequently increasing the amount of antibody binding, thus increasing the binding sites of the antigen. Another possibility would be to increase the mass sensitivity of the QCM. This can be achieved by increasing the resonance frequency of the sensor, since the sensor response to mass loading is directly proportional to the square of the operating frequency.

Figure III.7 displays a graph of 10 clinic nasal washing specimens as collected and same the 10 clinic nasal wash samples with RSV added to a concentration of 6×10^4 pfu ml^{-1}. The average background response of the 10 nasal wash

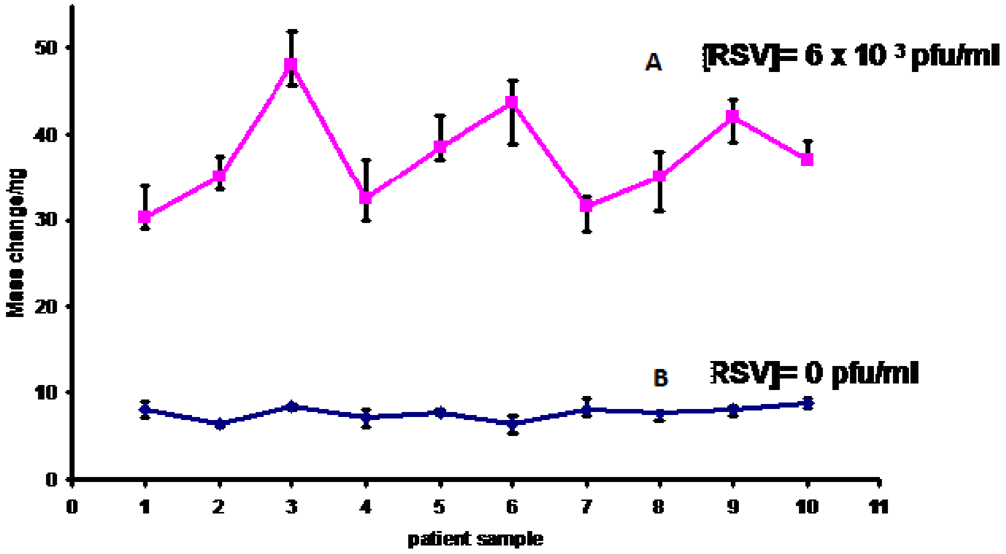

Figure III.7 - Clinic nasal wash samples from 10 healthy patients. A) Measurement of nasal wash samples with RSV (6 × 10^3 pfu ml^{-1}) prepared by adding RSV (cell culture) to blank nasal wash samples on healthy patients; B) measurement of blank nasal wash samples on healthy patients

specimens was 8 ± 2 ng, and average mass response of 10 nasal wash samples with RSV was 30 ± 3 ng. The signal to background noise ratio was greater than 3, confirming further that this immunosensor is able to successfully conduct RSV detection using clinical samples in the 10^4 pfu ml^{-1} range. This was in agreement with the results of the concentration dependant experiment discussed above and presented in Figure III.6. The detection limit is 9 × 10^3 pfu ml^{-1}. Figure III.7 indicates that the biological components in a nasal wash, such as mucus and debris, produce negligible interference with the detection of RSV. The performance of our RSV immunosensor with nasal wash samples shows that the sensor has high specificity for RSV.

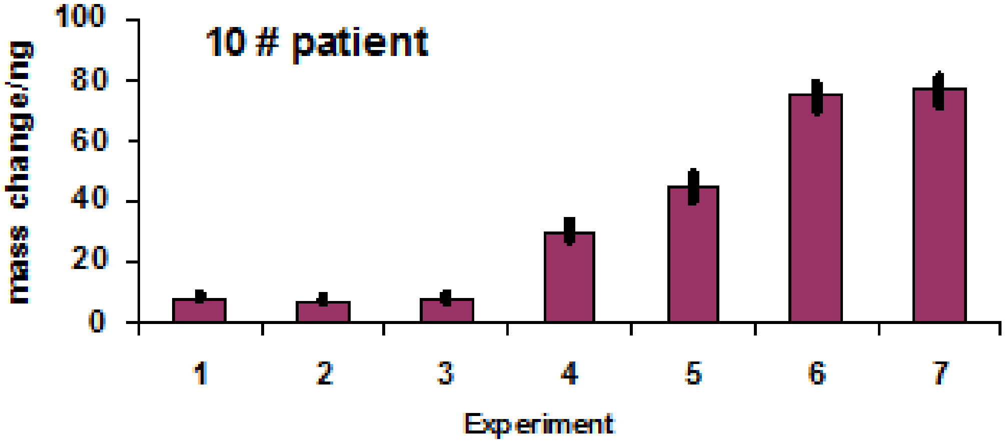

Figure III.8- RSV detection in nasal wash samples prepared by adding a concentration gradient of RSV from cell culture to a nasal wash sample from healthy patient #10 according to the following, x-axis: (1) is the blank; (2) [RSV] = 6.6 $\times 10^{1}$ pfu ml^{-1}; (3) [RSV] = 3.3 $\times 10^{2}$ pfu ml^{-1}; (4) [RSV] = 3.3 $\times 10^{3}$ pfu ml^{-1}; (5) [RSV] = 6.6 $\times 10^{4}$ pfu ml^{-1}; (6) [RSV] = 1.32 $\times 10^{5}$ pfu ml^{-1}; (7) [RSV] = 3.3 $\times 10^{5}$ pfu ml^{-1}.

We have randomly chosen the clinic nasal wash from patient #10 to conduct a RSV concentration dependence experiment. The results are summarized in Figure III.8. Figure III.8 shows the results of a RSV concentration dependence experiment with one of the wash samples (#10). A specific amount of RSV was added to each aliquot of nasal sample from the stock RSV solution (8 × 10^{6} pfu ml^{-1}). In Figure III.8, sample #2 (6.6 × 10^{1} pfu ml^{-1}), sample #3 (3.3 × 10^{2} pfu ml^{-1}) and sample #4 (3.3 × 10^{3} pfu ml^{-1}) show that the mass response remains in the same range as sample #1, the background (nasal wash samples shown in Figure III.7). This indicates that RSV had not reached the detection limit for this imunosensor when the concentration is in the 10^{2} pfu ml^{-1} range. The mass response was the same as the response of the background noise. The mass change, starting from sample #4 (6.6×10^4 pfu ml^{-1}), increases as the concentration of RSV increases; eventually it reaches a plateau indicating the sensor saturation. The RSV saturation concentration seen in Figure III.8 is similar to the saturation concentration obtained from the data displayed in Figure III.6 (5×10^5 pfu ml^{-1}). This is further proof that the performance of our RSV immunosensor is reproducible under a wide variety of conditions. We have conducted a similar experiment to that presented in Figure III.8 by using the nasal wash from a different patient chosen at random (#8). The data (Figure III.S.2 in supporting Information) is very similar to the data obtained for patient #10, stressing on the performance reproducibility of our sensor.

4. Conclusions

We have demonstrated for the first time that the presence of RSV in solution is quantifiable using an immunosensor based on a QCM piezoelectric crystal. We have used protein G to orient and immobilize RSV antibodies (Palivizumab) in the QCM to produce immunochips for RSV detection. Protein G exhibited a high affinity for gold while sustaining the ability to present the antibody with an advantageous orientation for further RSV binding. Palivizumab was immobilized on gold via protein G and the specificity of this sensor was successfully tested by using positive and negative control experiments. We have used AFM and ellipsometry to investigate the topography and thickness of each biolayer on the immunosensor surface. These techniques confirmed the presence of the layers used to build and test the sensor. The QCM crystal based immunosensor constructed with immobilized antibodies can be used to rapidly detect RSV in the liquid phase, with a detection limit of 9×10^3 pfu ml^{-1}. This sensor can detect RSV specifically; the immunosensor discriminates from MPV, a close relative of RSV. Thus, by using QCM, we were able to assemble an inexpensive and effective immunosensor for RSV detection; our method is quick, sensitive and efficient, and it could prove important in finding ways to treat and prevent the spread of RSV. The method we have developed for RSV detection provides a platform that could also be used for other immunological tests. Experimental testing of the immunosensor by using clinic samples of infected patients is ongoing.

5. Supporting Information

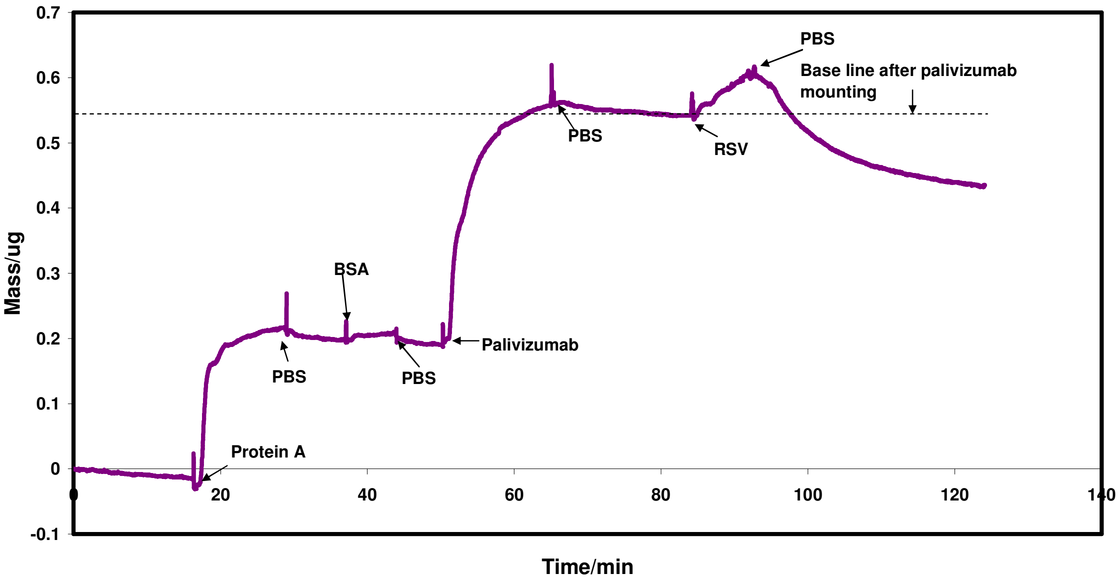

Figure III.S.1 - QCM run displaying the steps in the assembling and testing of a control of the RSV immunosensor, based on protein A, with the sequential formation of the following layers: protein A, BSA, Palivizumab (antibody). The procedure is similar to Figure III.3 in this paper, but the last step, PBS rinse, was prolonged over 40 minutes, and it indicates that this type of immunosensor is unsuitable for reliable RSV detection.

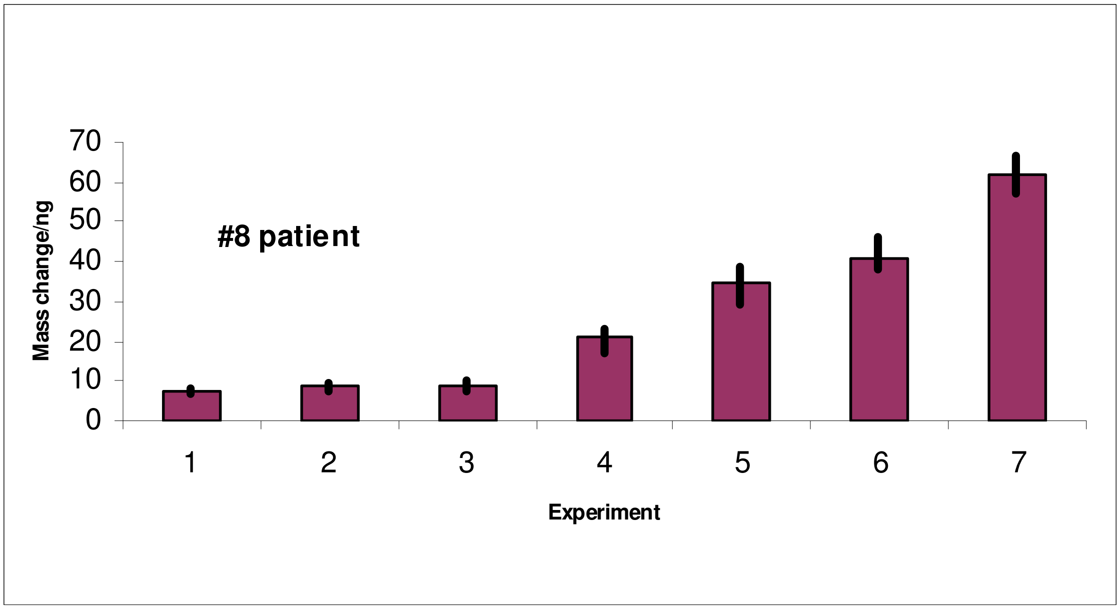

Figure III.S.2- RSV detection in nasal wash samples prepared by adding a concentration gradient of RSV from a cell culture to a nasal wash sample from healthy patient #8, this is, similar to Figure III.8 in this paper which test the nasal wash of healthy patient #10, according to the following, x-axis: (1) is the blank; (2) [RSV] = 6.6 $\times 10^{1}$ pfu ml^{-1}; (3) [RSV] = 3.3 $\times 10^{2}$ pfu ml^{-1}; (4) [RSV] = 3.3 $\times 10^{3}$ pfu ml^{-1}; (5) [RSV] = 6.6 $\times 10^{4}$ pfu ml^{-1}; (6) [RSV] = 1.32 $\times 10^{5}$ pfu ml^{-1}; (7) [RSV] = 3.3 $\times 10^{5}$ pfu ml^{-1}.

6. References

1. Crowe, J. E.; Firestone, C. Y.; Crim, R.; Beeler, J. A.; Coelingh, K. L.; Barbas, C. F.; Burton, D. R.; Chanock, R. M.; Murphy, B. R., *Virology* **1998,** *252* (2), 3.

2. Hall, C. B., *Science* **1994,** *265* (5177), 2.

3. CDC Respiratory syncytial virus. http://www.cdc.gov/ncidod/dvrd/revb/respiratory/rsvfeat.htm

4. Beeler, J. A.; Coelingh, K. v. W., *J. Virol.* **1989,** *63* (7), 10.

5. Chargelegue, D.; Obeid, O. E.; Hsu, S.-C.; Shaw, M. D.; Denbury, A. N.; Taylor, G.; Steward, M. W., *J. Virol.* **1998,** *72* (3), 7.

6. Roskos, L., *Drug Dev. Res.* **2004,** *61*, 13.

7. Takahashi, N.; Noma, T.; Honjo, T., *Proceedings of the National Academy of Sciences* **1984,** *81*, 5.

8. Press, E.; Hogg, N., *Biochemistry (Mosc).* **1970,** *117*, 20.

9. Bentley, D.; Rabbitts, T., *Nature* **1980,** *288*, 4.

10. *Pediatrics* American Academy of Pediatrics Committee on Infectious Diseases **1996,** *97*, 7.

11. *Pediatrics* American Academy of Pediatrics Committee on Infectious Diseases and Committee on Fetus and Newborn **1998,** *102*, 6.

12. Hall, C. B.; McBride, J. T.; Gala, C. L.; Hildreth, S. W.; Schnabel, K. C., *Journal of the American Medical Association* **1985,** *254* (21), 5.

13. Masters, H. B.; Weber, K. O.; Groothuis, J. R.; Wren, C. G.; Lauer, B. A., *Diagn. Microbiol. Infect. Dis.* **1987,** *8* (2), 5.

14. Mendoza, J.; Rojas, A.; Navarro, J. M.; Plata, C.; de la Rosa, M., *European journal of clinical microbiology & infectious diseases : official publication of the European Society of Clinical Microbiology* **1992,** *11* (5), 3.

15. Stone, G. P.; Mernaugh, R.; Haselton, F. R., *Biotechnol. Bioeng.* **2005,** *91* (6), 8.

16. Lipson, S. M.; Krilov, L. R., *Clin. Diagn. Virol.* **1994,** *2* (2), 8.

17. Landry, M. L.; Ferguson, D., **2000,** *38* (2), 4.

18. Bentzen, E. L.; House, F.; Utley, T. J.; Crowe, J. E., Jr.; Wright, D. W., *Nano Letter* **2005,** *5* (4), 5.

19. Meurman, O.; Sarkkinen, H.; Ruuskanen, O.; Hanninen, P.; Halonen, P., *J. Med. Virol.* **1984,** *14* (1), 5.

20. Abels, S.; Nadall, D.; Stroehle, A.; Bossart, W., *J. Clin. Microbiol.* **2001,** *39* (9), 5.

21. Falsey, A. R.; Formica, M. A.; Walsh, E. E., *J. Clin. Microbiol.* **2002,** *40* (3), 4.

22. Hu, A., Melissa Colella, John S. Tam, Ruth Rappaport, and Sheau-Mei Cheng, *J. Clin. Microbiol.* **2003,** *41* (1), 6.

23. Legoff, J.; Kara, R.; Moulin, F.; Si-Mohamed, A.; Krivine, A.; Belec, L.; Lebon, P., *J. Clin. Microbiol.* **2008,** *46* (2), 4.

24. Kox, L. F.; Rhienthong, D.; Miranda, A. M.; Udomsantisuk, N.; Ellis, K.; van Leeuwen, J.; van Heusden, S.; Kuijper, S.; Kolk, A. H., *J. Clin. Microbiol.* **1994,** *32* (3), 7.

25. Barletta, J., *Mol. Aspects Med.* **2006,** *27* (2-3), 20.

26. Stern, P.; Friedecky, B.; Bartos, V.; Bezdickova, D.; Vavrova, J.; Uhrova, J.; Rozprimova, L.; Zima, T.; Palicka, V., *Clin. Chem. Lab. Med.* **2001,** *39* (12), 5.

27. Owen, W.; Roberts, W., *Am. J. Clin. Pathol.* **2003,** *120* (1), 6.

28. Cacacem, M. G.; Landau, E. M.; Ramsden, J. J., *Q. Rev. Biophys.* **1997,** *30* (3), 37.

29. Sauerbrey, G., *Physics* **1959,** *155*, 7.

30. Kanazawa, K. K.; Gordon, J. G., *Anal. Chem.* **1985,** *57* (8), 2.

31. Thompson, M.; Kipling, A. L.; Duncan-Hewitt, W. C.; Rajakovic, L. V.; Cavic-Vlasak, B. A., *The analyts* **1991,** *116* (9), 10.

32. Gerdon, A. E.; Wright, D. W.; Cliffel, D. E., *Anal. Chem.* **2005,** *77* (1), 7.

33. Guilbault, G. G., *Analytical Chemistry Symposia Series* **1983,** *17*, 7.

34. Guilbault, G. G.; Luong, J. H., *J. Biotechnol.* **1988,** *9* (1), 10.

35. Carrigan, S. D.; Scott, G.; Tabrizian, M., *Langmuir* **2005,** *21* (13), 8.

36. Koenig, B.; Graetzel, M., *Anal. Chem.* **1994,** *66* (3), 4.

37. Lee, Y.-G.; Liu, S.-S.; Chang, K.-S., *Anal. Lett.* **2005,** *38* (2), 9.

38. Su, C.-C.; Wu, T.-Z.; Chen, L.-K.; Yang, H.-H.; Tai, D.-F., *Anal. Chim. Acta* **2003,** *479* (2), 7.

39. Zuo, B.; Li, S.; Guo, Z.; Zhang, J.; Chen, C., *Anal. Chem.* **2004,** *76* (13), 5.

40. Aslanoglu, M.; Houlton, A.; Horrocks, B. R., *The Analyst* **1998,** *123* (4), 10.

41. Caruso, F.; Rodda, E.; Furlong, D. N.; Niikura, K.; Okahata, Y., *Anal. Chem.* **1997,** *69* (11), 7.

42. Attili, B. S.; Suleiman, A. A. In *Development of piezoelectric biosensors for the determination of cocaine and cortisol*, Proceedings of the Annual Meeting of the Adhesion Society, Adhesion Society: 1996; p 4.

43. Gerdon, A. E.; Wright, D. W.; Cliffel, D. E., *Biomacromolecules* **2005,** *6* (6), 6.

44. Gerdon, A. E.; Wright, D. W.; Cliffel, D. E., *Angewandte Chemie, International Edition* **2006,** *45* (4), 5.

45. Rickert, J.; Brecht, A.; Gopel, W., *Anal. Chem.* **1997,** *69* (7), 8.

46. Akerstrom, B., *J. Immunol.* **1985,** *135* (4), 4.

47. Akerstrom, B.; Bjorck, L., *J. Biol. Chem.* **1986,** *261* (22), 8.

48. Bjorck, L.; Kronvall, G., *J. Immunol.* **1984,** *133* (2), 6.

49. Eliasson, M., *J. Biol. Chem.* **1988,** *263* (9), 5.

50. Fahnestock, S., *Trends in Biochemical Science***1987,** *5*, 5.

51. Nygen, H.; Werthen, M.; stenberg, M., *J. Immunol. Methods* **1987,** *101*, 9.

52. Goward, C.; Scawen, M., *Trends Biochem. Sci* **1993,** *18*, 5.

53. Dubrovsky, T. B.; Demcheva, M. V.; Savitsky, A. P.; Mantrova, E. Y.; Savransky, V. V.; Belovolova, L. V., *Biosens. Bioelectron.* **1993,** *8* (7-8), 9.

54. Sauer-Eriksson, A. E.; Kleywegt, G. J.; Uhlen, M.; Jones, T. A., *Structure* **1995,** *3* (3), 14.

55. Oh, B.-K.; Chun, B. S.; Park, K.-W.; Lee, W.; Lee, W. H.; Choi, J.-W., *Materials Science & Engineering, C: Biomimetic and Supramolecular Systems* **2004,** *C24* (1-2), 5.

56. Goyal, D.; Pribil, G.; Woollam, J.; Subramanian, a., *Material Science and engineering B* **2008,** *149*, 8.

57. Kallewaard, N. L.; Bowen, A. L.; James E. Crowe, J., *Virology* **2005,** *331* (1), 9.

CHAPTER IV

Scanning Electrochemical Microscope Software Suite with Real-Time Three-Dimensional Graphics Using the LabVIEW Environment

1. Introduction

Scanning electrochemical microscopy (SECM) is an increasingly popular technique. This technique produces electrochemical data with high spatial resolution. An ultramicroelectrode (UME) is rastered within close proximity to a substrate and a detailed map of electrochemical activity is produced. Published papers applying the method have been increasing annually, from 5 published articles on SECM in 1990 to 76 in 2005 to approximately 100 in 2009. The topics examined are also highly varied. This technique is applicable to a wide range of studies, from metal corrosion thermodynamics and analysis of electrochemical activity of prospective bimetallic catalysts[1] to predicting the quality of pancreatic islets for transplant[2] or for use to spatially map the enzymatic activity of a biosensor.[3] The SECM itself is a versatile technique that can be exploited in countless modes from the standard feedback[4] and the two generation-collection modes, tip generation-substrate collection[5] and substrate generation-tip collection,[6] to more complicated alternating current scanning electrochemical microscopy (AC-SECM).[7] These modes are further put into two categories of

SECM, constant height and constant distance, of which constant distance includes alternating current SECM.

The software discussed in this paper was written for constant height mode SECM. The preference to programming for the constant height mode of the SECM was a result of many factors. It is easier to perform experiments in the constant height mode. Troubleshooting the different routines within the program for the production of the micrographs is more readily performed without the addition of tip movement in the case of shear force constant distance SECM and the additional capacitance measurements required for the AC-SECM. The necessary procedures in the constant height mode SECM, cyclic voltammetry (CV), approach curve, and graphing capabilities are also required for production of the constant distance modes, and the presented software could be modified for use in constant distance experiments.

Our system overcomes hysteresis, the chief deficiency that is often encountered in SECM platforms. I have used optical encoders inside each of the three state of the art stepper motor enclosures, consequently providing precision determination of the position for each axes. The enclosed piezoelectric actuators coupled with the optical encoders provide accurate displacement measurements and that are relayed to the software at every equidistant user designated point. This ensures that the sides of the area examined by the electrode are linear and perpendicular to the ends. Also the optical encoders provide the ability to record more precise and more accurate tip positions and electrochemical features present in the scanned area than any available SECM system either in the literature or obtainable through any commercial outlet is able to produce.

Previous experiments have left in doubt the veracity of the image with respect to a poorly attached experimental object drifting in the produced image. If an item drifts during the imaging experiment it would appear elongated in the direction that it drifts. By making a modification in the software we have removed this uncertainty. It is possible to exchange the long and short axis of motion without withdrawal of the tip from the substrate. This rotates the image by 90^0 and allows for confirmation that the details in the observed image are a true representation of what is on the substrate and not an artifact of the UME tip shape or motions within the experimental vessel.

The lack of real-time graphing capability of some SECM software suites often results in significant wasted time if the area of the micrograph is incorrect or another problem presents itself during the scanning process, which may be indistinguishable during the experiment and only detectable after the graphing procedure is complete. The real-time graphing feature drastically reduces time spent on images that are collected erroneously, whether the tip is imperfect, the substrate is not orthogonal to the tip, or the tip is aligned over an area that is not of interest. When the graphing process occurs in a separate spreadsheet-software program in a post-experiment routine, the time required to complete the experiment after the error occurs and the time to run the graphing procedure is wasted.

The commercially available SECM hardware/software combinations are expensive. The cost of purchasing retail SECM systems is very high, while simply acquiring a set of nanopositioners, a computer with LabVIEW software, and a data acquisition board, from National Instruments is relatively inexpensive by comparison.

One of the main goals for the production of this program suite is for the software not only to be of good quality, to produce useful electrochemical micrographs of high-quality efficiently, but also to allow the software to be modified for use in the most possible systems. The application of the LabVIEW programming software to the SECM enables us to achieve versatility in the technique that other SECM available systems do not provide. The integration of additional apparatus into the platform is possible. We incorporated the capillary electrophoresis equipment in to the SECM platform in order to deposit the aliquots of a separation onto the target substrate areas. In an analogous procedure other scientific tools would assuredly expand the possible applications of the SECM and this software package could be used to assist in the development of those systems. Also, our instrument can be interfaced easily with an inverted microscope for various applications where one might want to visually monitor the imaged substrate, such as in the case of imaging live cells.

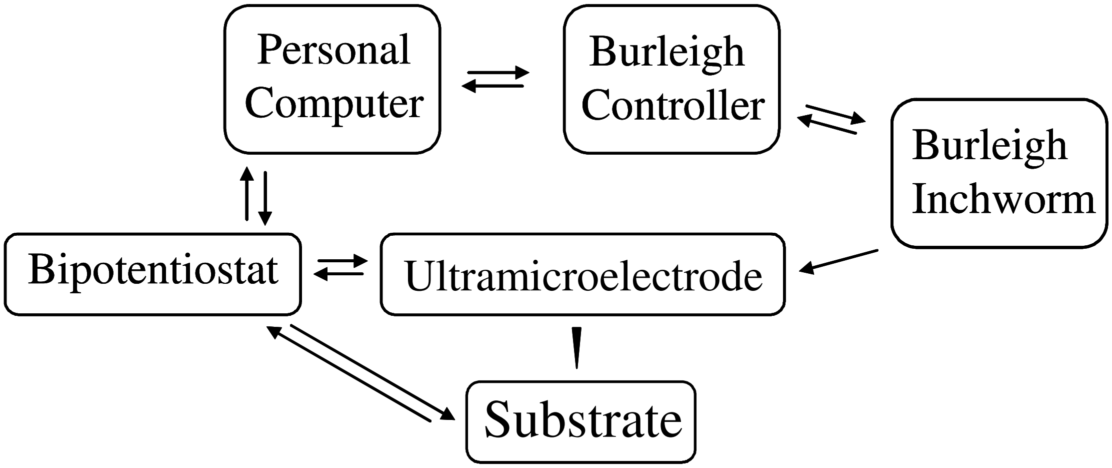

Figure IV.1. Scanning electrochemical microscope schematic shows the basic equipment requirements for electrochemical imaging using the described LabVIEW programs. The computer controls the position of the UME through the Burleigh Inchworm and Inchworm Controller and the electrochemical activity in the cell by affixing the potential of the substrate and UME with the Cypress Systems Bipotentiostat.

Interfacing other techniques may not always be easily possible with commercially available SECM systems.

Figure IV.1 is an SECM schematic. The electrochemical microscope cell, containing four electrodes including the substrate, is secured on an optical table beside the Burleigh 1500 three-axis nanopositioner. Adjacent to the optical table is a personal computer that communicates with the bipotentiostat and Burleigh controller. The Cypress Systems Bipotentiostat Model EI-400 FCV controls the potential of both the substrate and the UME. The bipotentiostat also transmits the output current information from the UME to the computer for graphing in the z-axis. These electrochemical data are routed to the computer through National Instruments BNC-2090, a rack-mounted analog accessory. The Burleigh

Inchworm Controller 8200 relays the position instructions to the Burleigh 1500 three-axis nanopositioner and transmits the position measurements from the inchworm's interferometers to the computer's general purpose interface bus card for x- and y-axes of the graph produced in real time. The Burleigh inchworm rasters the UME across the surface of the substrate in an "E" shaped or "Ш" shaped pattern.

2. User Interface

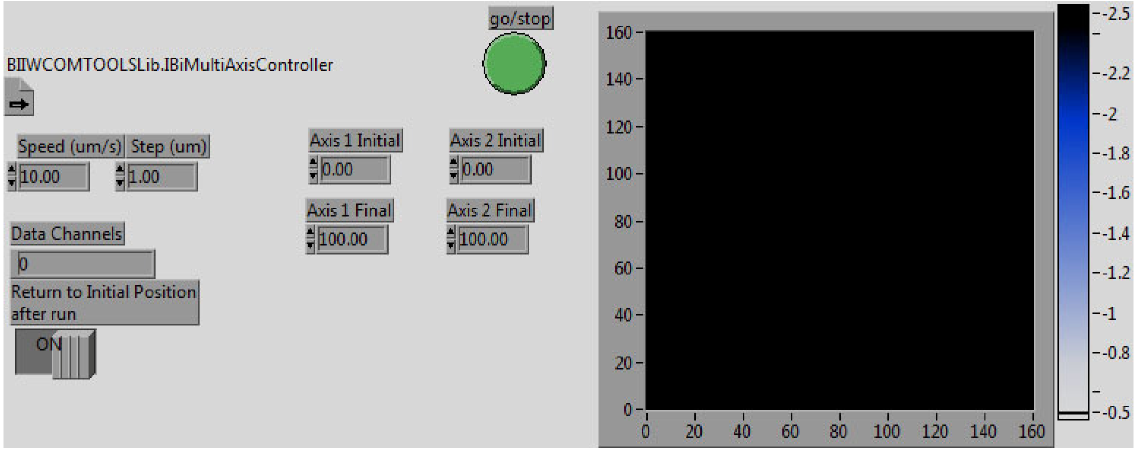
BIIWCOMTOOLSLib.IBiMultiAxisController

Speed (um/s): 10.00
Step (um): 1.00
Axis 1 Initial: 0.00
Axis 2 Initial: 0.00
Axis 1 Final: 100.00
Axis 2 Final: 100.00
Data Channels: 0
Return to Initial Position after run: ON

Figure IV.2. The user interface of the imaging program is employed for the control of the rate of the electrode movement, size of the image, if the electrode is returned to the origin after completion of the scan, detail of the acquisition of the electrochemical micrograph and immediate termination of the run. This panel also shows where the the 3D graph of the electrochemical data is displayed as they are collected in real time.

Figure IV.2 displays the user interface, or the Virtual Instrument (VI) Front Panel of the imaging software. With this panel the user defines the size of the image by selecting initial and final positions in both the x-axis and y-axis, the detail of the graph by choosing a step size used for the graph, the speed at which

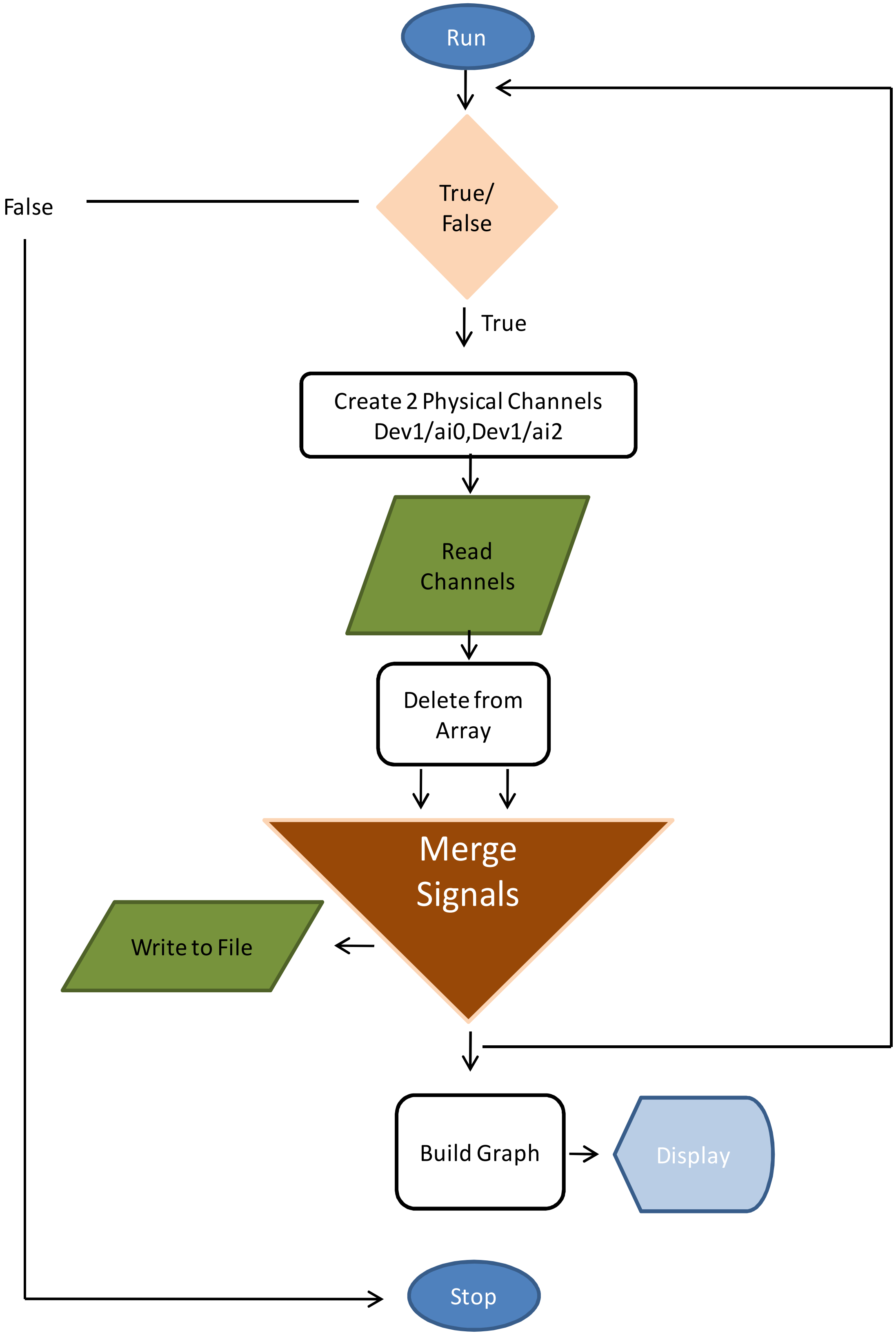
Run
True/
False
False
True
Create 2 Physical Channels
Dev1/ai0,Dev1/ai2
Read
Channels
Delete from
Array
Merge
Signals
Write to File
Build Graph
Display
Stop

Figure IV.3. Flow chart for cyclic voltammetry program

the tip moves and whether or not it is preferable to return the tip to the origin. In case the tip and substrate contact each other there is also a force stop button to prevent further damage to the tip or substrate. As the UME examines the electrochemistry of each point of the user-defined area, the operator is able to monitor the data while it is added to the graph on the right side of the Front Panel as each point is collected. For confirmation of the initially acquired image use of the second “reverse image” program with identical parameters will produce an identical image on the graph if no perturbations are made to the electrochemical system.

3. CV and Approach Curve

In order to approach the UME to the substrate the electrochemical parameters for the cell must be defined. The CV verifies qualitatively the merit of the UME and supplies a minimum potential value for the UME during approach. Figure IV.4A shows a CV that is acquired and saved to file using the first program in the software suite. The software also reproduces the CV on the computer screen in real-time. For the ensuing approach curve attempt in this system a voltage of +0.65 V versus Ag/AgCl, 3 M KCl was applied. This potential value was chosen by examining the CV to ensure that the oxidation of the electrochemical mediator will occur. For this particular electrochemical mediator FcTMA, the substrate potential has to be set below +0.2 V versus Ag/AgCl, 3 M KCl.

The second process necessary for production of an electrochemical micrograph is the approach-curve routine. Using the potential for the substrate and UME working electrodes acquired from the CV, the UME is moved toward the substrate at a user-specified rate while the current and position are monitored with the software. In this software suite a graph is produced in real-time with the data that is concurrently written to a text file.

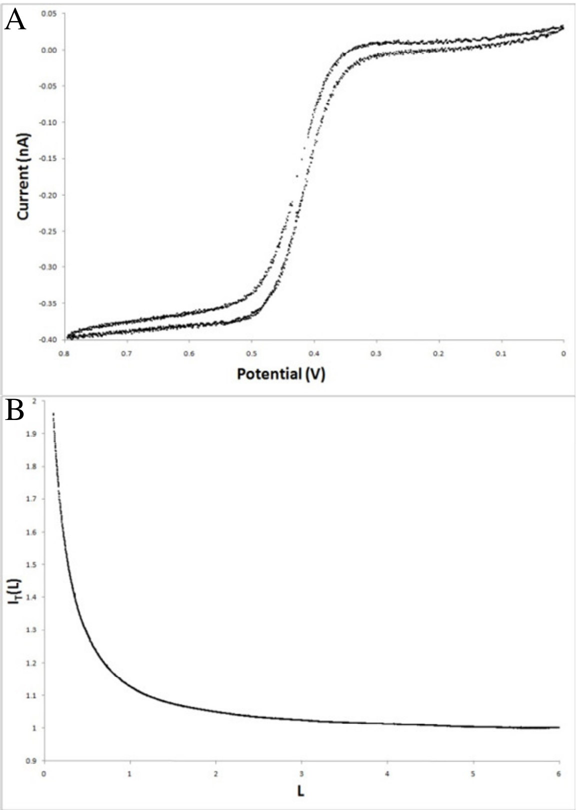

Figure IV.4. A) The graph indicates the successful performance of the first program in the suite. A cyclic voltammogram is used to verify the quality of tip preparation and the parameters for the potential, vs. Ag/AgCl, 3M KCl reference electrode, of the substrate and 25 µm UME for the approach curve and image scan. The entire imaging experiment was performed in 1 mM FcTMA in 100 mM KCl. B) An approach curve of a 25 µm UME to an interdigitated array of 10 µm Au fingers and 10 µm spaces of quartz glass. The current deviates from the theoretical approach curve to a conducting surface because the surface alternates conducting gold and insulating quartz surfaces. i_{ss} = 2.05 nA

Figure IV.4B shows an example of the UME approach to an interdigitated array of Au fingers on quartz. The tip's descent toward the substrate is initiated either through the use of the down button or by use of the "Move to Target" feature, when the target is in the direction of the substrate. The approach routine is terminated either with a cleverly named "stop" button or when the target has been reached if that is the method of approach. The "stop" button will, of course also terminate the movement of the UME if the approach was started with the "Move to Target" option. It is also possible to produce curves of the UME being withdrawn from the surface are easily, with the use of the "up" button. Data is saved and the text file becomes accessible when the "close" button is depressed or the Virtual Instrument is aborted with the National Instrument's stop button.

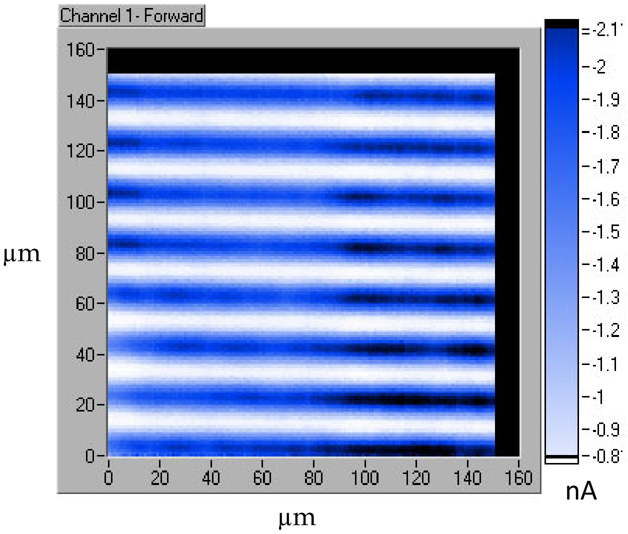

Figure IV.5. A completed electrochemical micrograph of an interdigitated array shows electroactive conducting areas and insulating glass areas. Also, the skew of the substrate relative to the x-y plane that the tip of the UME travels is observable. This graph was produced with the electrochemical data recorded at 1 µm spacing with a tip speed of 10 µm s^{-1} over a 150 µm square.

4. Real-Time Performance, Real-Time Image

Figure IV.5 is a screen shot of the collected data of a 25 μm Pt UME rastered across an interdigitated array of Au on quartz. This is how the graph appeared in the front panel at the completion of the run; each point was rendered on the image as it was collected and the range of the scale was automatically defined as the points of the graph were collected. The fingers and gaps in the array are 10 μm wide. These details are easily observed in the image as well as the tilt of the substrate with respect to the x-y plane traveled by the UME, the right side is clearly higher than the left and bottom of the substrate appears higher than the top.

5. Conclusions

I have programmed an easily amendable software suite and used it for the scanning electrochemical microscope in the LabVIEW graphical programming environment applying state of the art stepper motors with optical encoders for precise and accurate positioning. The four programs that make up the software suite which produces the electrochemical micrographs are a CV program, approach curve program, and two imaging programs with perpendicular major axis. Incorporating optical encoders allows for the user to raster an UME precisely above the desired substrate for the production of an accurate map of the electrochemical activity of the surface. The graphs are produced in real time and the data are saved for postproduction modification. Our software suite performs SECM with the unsurpassed precision and exactness with lower cost, it is also able to be interfaced easily with other techniques and without hysteresis.

6. References

1. Jung, C.; Sanchez-Sanchez, C. M.; Lin, C.-L.; Rodriguez-Lopez, J.; Bard, A. J., *Anal. Chem. (Washington, DC, U. S.) FIELD Full Journal Title:Analytical Chemistry (Washington, DC, United States)* **2009,** *81* (16), 7003-7008.

2. Goto, M.; Abe, H.; Ito-Sasaki, T.; Goto, M.; Inagaki, A.; Ogawa, N.; Fujimori, K.; Kurokawa, Y.; Matsue, T.; Satomi, S., *Transplant Proc FIELD Full Journal Title:Transplantation proceedings* **2009,** *41* (1), 311-3.

3. Schaefer, D.; Maciejewska, M.; Schuhmann, W., *Biosens. Bioelectron. FIELD Full Journal Title:Biosensors & Bioelectronics* **2007,** *22* (9-10), 1887-1895.

4. Kwak, J.; Bard, A. J., *Anal. Chem.* **1989,** *61* (11), 1221-7.

5. Liu, B.; Bard, A. J., *J. Phys. Chem. B* **2002,** *106* (49), 12801-12806.

6. Martin, R. D.; Unwin, P. R., *Anal. Chem.* **1998,** *70* (2), 276-284.

7. Eckhard, K.; Schuhmann, W., *Analyst (Cambridge, U. K.)* **2008,** *133* (11), 1486-1497.

CHAPTER V

Capillary Electrophoresis Fountain Pen

1. Introduction

A. Surface Patterning. The application of active chemicals onto a substrate in a desired pattern has become increasingly important in modern society; this process is critical not only to the electronics industry and for the formation of chemical arrays, but also for more common aspects of cotidian life. In the fall, when the temperatures are low, latex paints that are applied in the cold suffer from reduced life expectancy and increased blotchiness due to the slow film formation which results in brittleness of the dried paint.[1] So, in order to paint when the temperature is low, a different drying mechanism is required; during cold temperatures oxidation is used for the drying of the paint.[2] Research into techniques for applying chemicals onto a surface in desired patterns has expanded dramatically recently. The electronics industry invests extraordinary amounts of time and money into finding different photoresists and photolithographic methods for reducing the size of features that can be produced for integrated circuits. Biotechnology companies are creating protein arrays for the detection of many contaminates within a single sample cotemporaneously.[3]

By creating protein arrays, high, throughput screening of protein-analyte interactions is acheivable.[4]

With electronics influencing almost all facets of life, increasing the number of transistors on a circuit will allow for further miniaturization and performance enhancements of electronic products. The industrial mass production of integrated circuits vies to keep up with Moore's Law, which states that every 18 months the number of transistors contained on an integrated circuit will double.

Photolithography is presently the state of the art process for the patterning of a substrate with chemically active compounds for mass production. With respect to the mass production of chemically active patterns on surfaces this technique is currently the apex. During the photolithographic process, a photoresist is applied onto a surface and subsequently different sections are developed by selective exposure to light. After exposure to light the more soluble area is removed. For positive resists, the areas exposed to light are washed away, while for the negative photoresists the area shielded from light remains soluble and washes away.[5] The limiting factor in this form of lithography is the wavelength of light that is used in the exposure step. In order for the industry to continue to improve according to Moore's Law, methods need to be developed that will allow the production of electrical circuit features that are smaller than those limited by photolithography.

New techniques of lithography are being explored. Soft lithography techniques are being developed based on the creation small features in poly-dimethylsiloxane (PDMS) and using the molded PDMS as a stamp. These techniques are being applied to a variety of functions, for the manipulation of DNA molecules and cells,[6,7] as biomaterials analogues,[8] supplementing atomic layer desorption,[9] and complementary plasmonic structures.[10] These soft lithographic techniques include, but are not limited to; microcontact printing, replica molding, and soft imprinting.[11,12]

Replica molding uses a PDMS mold in order to form the desired structure. Two related techniques are micromolding in capillaries and microtransfer molding. The initial procedure for micromolding in capillaries entailes the making of a PDMS mold, which is then placed on a surface, and the open capillaries within the PDMS are injected with a prepolymer. The prepolymer then fills the open space of the mold and is subsequently allowed to harden. [11] More recently this technique has been used with an analyte in a solvent instead of the prepolymer. The solvent is allowed to dry completely leaving a pattern of the analyte where the PDMS mold dictates.[13] This has advantageous properties for the design of patterns using nanoparticles and biomaterials.[13] The microtransfer molding procedure entails filling the PDMS mold with a prepolymer, removing the excess, applying to a surface and curing.

Soft imprinting is a procedure where a flexible surface is used to apply the pattern. Many polymers have been used to create the imprinting surface such as, PDMS, polystyrene, and polymethylmethacrylate.[12] This method takes advantage of the flexible nature of the stamp in order to apply the pattern to curved and irregular surfaces over a large area, such as a circular tube with a 16 mm diameter.[12] The limits of the detail of these methods reach down to 30 nm.[11]

Microcontact printing involves the production of a PDMS stamp. This stamp is dipped into a solution of molecules, the "ink", that are being used to create the self-assembled monolayer (SAM). The "ink" is then transferred to the substrate by direct contact, creating the pattern of the stamp. This technique has been used in conjunction with DNA sequences linked to fluorescent markers, illustrating the potential for research in the biomolecular field.[14] In microcontact printing, an elastomeric stamp is used to apply a SAM to the intended surface, often photoresist or alkanethiolate on a metal surface.[15] Figure V.1 illustrates multiple approaches to microcontact printing. A flat stamp with molded features is able to apply a monolayer to a flat surface, but cylindrical surfaces may also be used as the applicator or as the surface to which the monolayer is attached. Microcontact printing is able to form features as small as 50 nm.[15] This is achievable using specially designed stamps that contain an under-layer molded with rigid hydrosilane end-linked PDMS. A standard thick flexible layer of

PDMS is molded onto the rigid under-layer. This multiple layer stamp improves the shape and minimum size achievable for the transferred monolayered pattern.

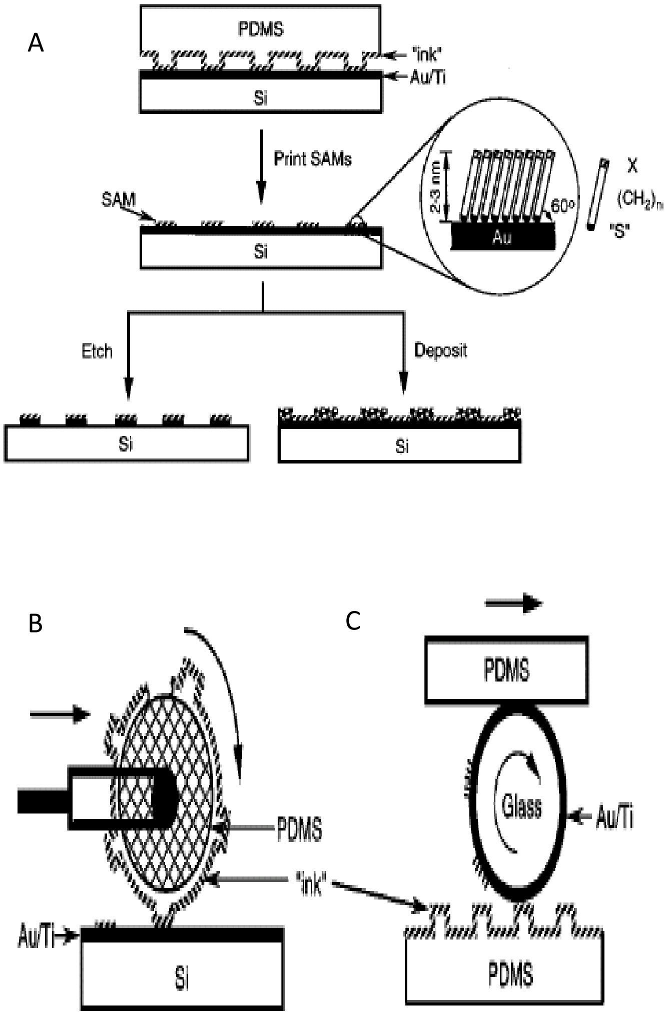
A
PDMS
"ink"
Au/Ti
Si
Print SAMs
SAM
Si
2-3 nm
60°
Au
X
$(CH_2)_n$
"S"
Etch
Deposit
Si
Si
B
PDMS
"ink"
Au/Ti
Si
C
PDMS
Glass
Au/Ti
PDMS

Figure V.1. Schematic procedures for microcontact printing of thiols on the surface of gold: (*A*) printing on a planar surface with a planar stamp, (*B*) printing on a planar surface over large areas with a rolling stamp, and (*C*) printing on a nonplanar surface with a planar stamp. Xia, Y.; Whitesides, G. M., *Annual Review of Material Science* **1998,** *28*, 153-184.

Another nanolithography method for applying a molecule to a surface is the "dip-pen" (DPN), a technique that uses a scanning probe tip as a dip pen to apply the ink. As shown in Figure V.2, 1-octadecanethiol dots can be applied with a 1.8 μm diameter to a gold surface, by using an atomic force microscope type tip made out of PDMS.[16] The dip-pen lithograph apparatus has been modified with as many as 55,000 pens arranged in parallel, in a 2D array that is able to print with a resolution better than 100 nm over 1 cm^2 area.[7] Depositing a thiol ink on a gold substrate is only one application of the DPN. This technique has been shown to be applicable to silazanes on semiconductor surfaces,[17] metal structures on conductive surfaces,[18] alkylthiol-modified oligonucleotides,[18] and inorganic salts on a silicon surface.[17] This technique has branched out rapidly since first reported by Mirkin and coworkers.[19] Some of the variants of the original thiol on a single tip apparatus include thermal DPN, electrochemical DPN, nanofountain pen lithography and parallel DPN.[20]

These methods of surface patterning are able to create exquisite forms on a surface, but with major drawbacks. Nanolithography with a scanning probe tip is only able to generate a design in a very small area. The tips also may become deformed during the process and lose their ability to perform with the required specifications do to fragile features and wear.[11] Stamping types of nanolithography require repeated inking of the elastomer

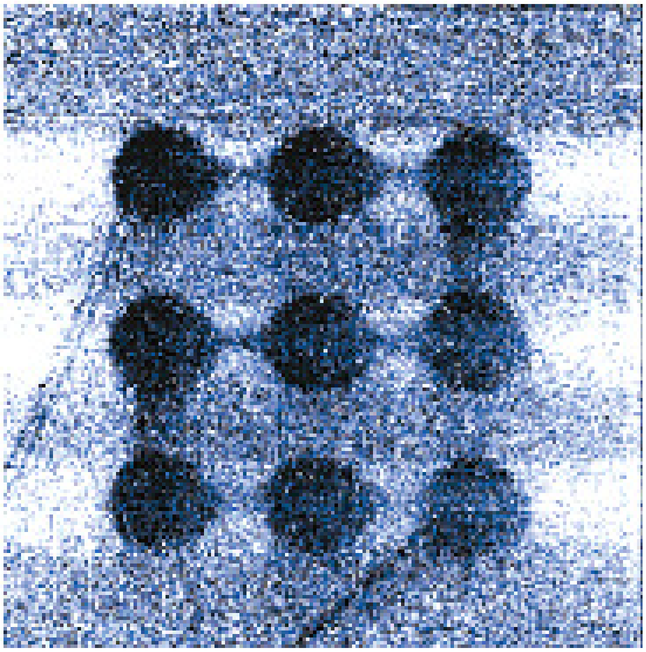

Figure V.2. 12 μm x 12 μm image of 1.8 μm octadecanethiol dots applied with poly(dimethylsiloxane) tip. Piner, R. D.; Zhu, J.; Xu, F.; Hong, S.; Mirkin, C., *Science* **1999,** *283*, 661-663.

stamp which is time consuming.

B. Capillary Electrophoresis. Capillary electrophoresis uses a high voltage power supply to force a small current through a quartz capillary with a small diameter. The applied voltage causes the electrophoretic migration of sample through the quartz capillary. The velocity, ν [m s^{-1}], at which something travels through capillary, follows Equation (1):

$$\nu = \mu E \qquad [1]$$

Here the velocity is expressed as a product between total mobility, μ [m^2 V^{-1} s^{-1}], and the field strength, E [V m^{-1}]. The velocity may also be defined in terms of the travel length per time:

$$\nu = \frac{L_d}{t_r} \qquad [2]$$

The length, L_d [m], is from the capillary input to the detector and, t_r [s], is the time it takes for the wave front to reach the detector. The combination and rearrangement of these two fundamental equations of elecrophoresis allows for the calculation of the mobility from known experimental parameters and the observed experimental time. The total mobility of a solute across the capillary is the sum of electroosmotic mobility, μ_{eo} [m^2 V^{-1} s^{-1}], and electrophoretic mobility, μ_{ep} [m^2 V^{-1} s^{-1}].[21]

$$\mu = \mu_{ep} + \mu_{op} \qquad [3]$$

The magnitude of the electroosmotic mobility depends on the applied voltage and the ionic strength of the buffer. The electroosmotic mobility is often determined through the addition of a neutral marker that travels at the velocity of the bulk solution. The electroosmotic flow transports the sample, but is not the cause of the separation that is observed.

The separation in capillary electrophoresis is the result of differing electrophoretic mobilities;

$$\mu_{ep} = \frac{q}{6\pi\eta r} \qquad [4]$$

Where, q [C], is the charge of the analyte, η [kg s^{-1} m^{-1}], is the viscosity of the solution, and, r [m], is the effective radius of the analyte.[21] The electrophoretic mobility is a measure of the ratio of charge to size and viscosity.

CE has been combined with other analytical tools in order to enhance analysis techniques. One example is the use of a scanning probe microscope in conjunction with a CE column for the analysis of small biological systems. This way the

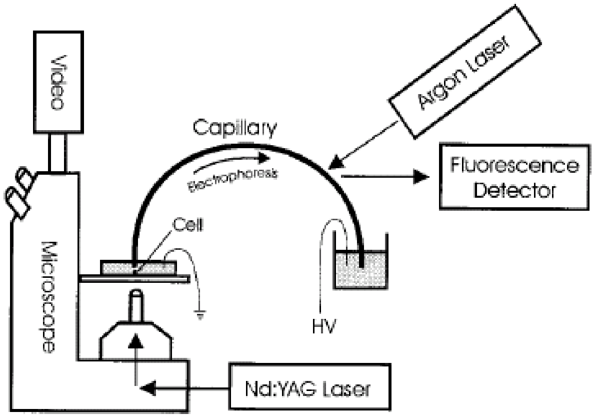

Figure V.3. Schematic of the system used for cell lysis. Li, H.; Sims, C. E.; Wu, H. Y.; Allbritton, N. L., *Analytical Chemistry* **2001,** *73*, 4625-4631

products of a single cell lysis can be separated and analyzed with an enhanced resolution. A single laser pulse from a Nd:YAG laser was able to lyse a rat basophilic leukemia cell.[22] The laser was aimed 20 μm away from the cell, in order to prevent photodestruction and photobleaching. The product of the lysis entered the capillary, positioned 15-20 μm above the cell. The results produced from the set up displayed in Figure V.3 are electropherograms with well defined peaks (not shown).[17] However, the combination of capillary electrophoresis with a scanning probe for the purpose of nanolithography presented in this chapter was unprecedented.

C. Capillary Electrophoresis Fountain Pen. To promote the substrate patterning endeavors, a capillary electrophoresis fountain pen (CEFP) was assembled and the plans are described in this chapter. Key for the analyte-substrate attraction is the proximity of the analyte to the surface. In order to assure that the analyte is presented to the surface, the capillary must be positioned near the surface. To accomplish this task, tip approach methods must be translated from similar tasks. Scanning electrochemical microscopy uses a feedback approach curve; an ultramicroelectrode can be approached to the distance where the current increases to eight times the steady state current for a conducting surface.[23] Combining electrophoretic separation with lithography will provide an exciting advance in production of patterns in the micrometer and nanometer range.

First, operating with the ink constantly available to be eluted from the tip, designs will be created as if the instrument is a fountain pen with a constant supply of ink. It will operate as if the chemical that is to be deposited on the surface had been previously separated and the solution is homogeneous. Instead of using a buffer solution for electroosmotic flow, the solution including the molecule of interest is used in the solution creating the electroosmotic flow.

Figure V.4 presents a schematic for assembling the instrumentation for the capillary electrophoresis fountain pen. In the simplest terms, a glass capillary is used as a conduit for the electrolyte solution, and the analyte that it carries with it, to reach the substrate where it is patterned by the movement of the

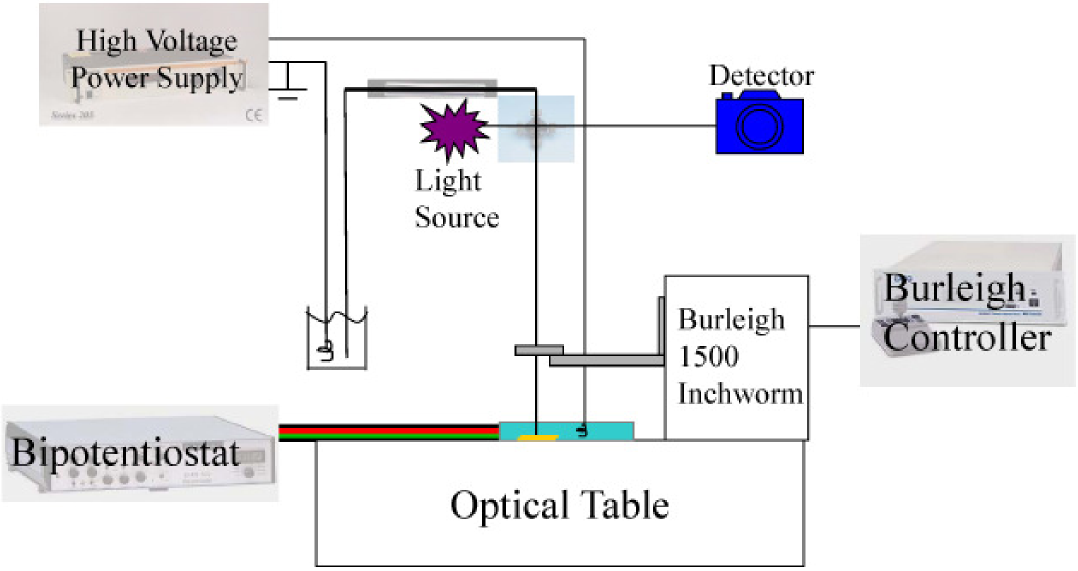
High Voltage
Power Supply
Detector
Light
Source
Burleigh
Controller
Burleigh
1500
Inchworm
Bipotentiostat
Optical Table

Figure V.4. Schematic of the capillary electrophoresis fountain pen.

nanopositioner. The potential to design experiments where the solution undergoing electrophoretic separation is characterized in real-time within the capillary followed by the examination of some specific activity across an array on the substrate could add a valuable tool for the analytical chemist to apply. The vast range of uses for the electrophoretic study of chemicals and solutions provides a myriad of potential analytes for use as the inking material.

D. Inks for CEFP. For the purpose of inking a substrate in the initial experiments, monolayer protected gold clusters were used. Templeton *et al.* have performed the capillary electrophoretic separation of this type of nanocrystals, and have shown that the electrophoretic flow is

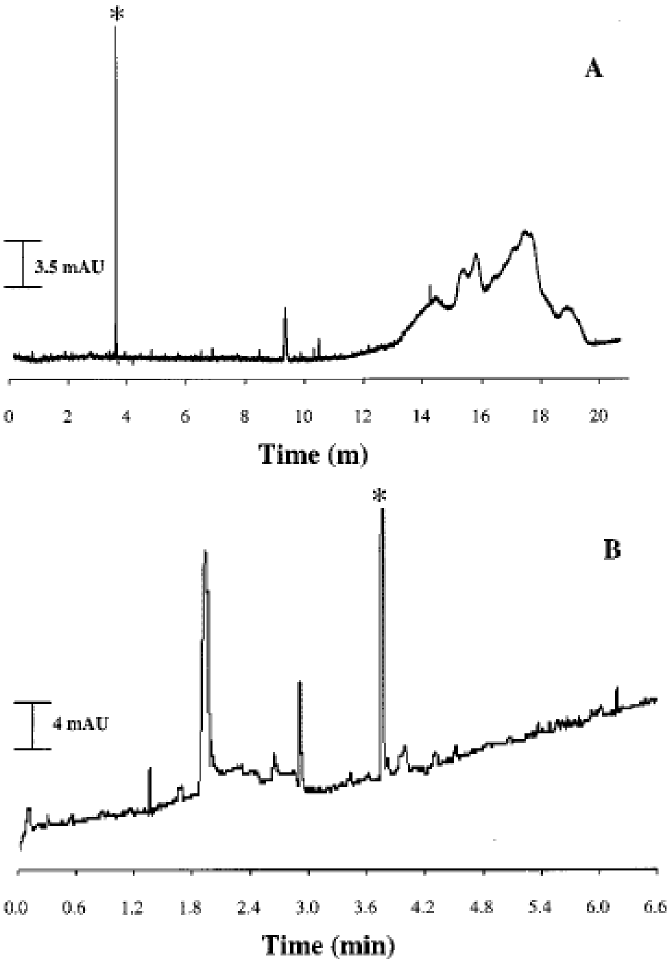

Figure V.5. Electropherograms of gold clusters protected with tiopronin (A) and MEAV (B) Templeton, A. C.; Cliffel, D. E.; Murray, R. W., *J. Am. Chem. Soc.* **1999,** *121*, 7081-7089

highly dependent on the properties of the gold's protecting monolayer.[24] The two types of monolayer protecting the gold clusters reported were tiopronin and N-(methyl)-N-(ethylamine)-viologen dinitrate (MEAV). Figure V.5 indicates that MEAV elutes prior to a neutral marker while the tiopronin cluster elutes after the neutral marker. Thus, the MEAV cluster maintains a positive charge in the buffer solution, sodium borate buffer (pH 9.3), while the tiopronin cluster is negative.[24] The magnitude of the charge on the tiopronin was reported as -7.4, while the electrophoretic separation of the sample of MEAV clusters resulted in a reported charge of +23.

Many of these values are determined during the electrophoretic separation using on-line detection. This detection takes advantage of the optical properties of the analyte, *e.g.*, the optical properties of monolayer protected clusters (MPCs). The optical properties of nanocrystals are of great interest because they have a tunable and intense color.[25] This intense color is due to the plasmon resonance that occurs upon the adsorption of electromagnetic radiation. The dimensions and dielectric constant of the nanocrystals define the wavelength of energy that is resonant with the particle.[26]

Figure V.6 shows the size dependant adsorption of light by monolayer protected clusters.[27] As the crystals become smaller, the plasmon resonance peak blue shifts prior to totally disappearing. This also corresponds to the observed color of the solution, larger particles show reds and oranges, while the solutions containing smaller nanocrystals (< 3 nm) become black as a result of the broad adsorption.[25] This is consistent with metal nanoclusters of all types of core materials.

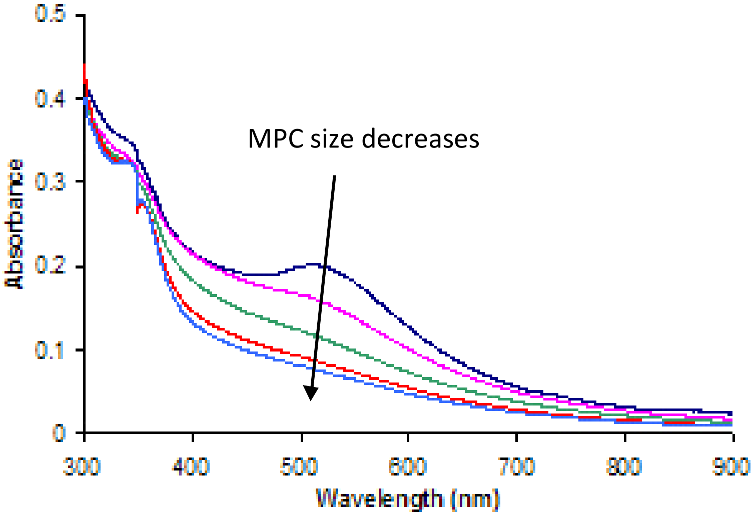

Figure V.6. UV-vis adsorption of gold monolayer protected clusters (unpublished data courtesy of Dr. R. Peterson)

2. Materials and Methods

A. Chemicals. 98% sodium borohydride, N-(2-mercaptopropioyl) glycine technical grade (99%) and methyl alcohol were purchased from Sigma-Aldrich. Glacial acetic acid was purchased from Fisher. Tetrachloroauric acid was prepared according to the literature.[28]

*B. Synthesis of Au Nanocrystals***.** 0.93 grams of tetrachloroauric acid and 1.14 g of N-(2-mercaptopropioyl) glycine were co-dissolved in 100 mL of 6:1 mixture of chilled methanol/acetic acid. To this ruby red stirred solution, 1.8 g of sodium borohydride were added. The crystals were allowed to develop in the solution for 30 minutes before the methanol was rotovapped off.[29]

*C. Capillary Electrophoresis***.** Capillary electrophoresis was performed with capillaries of various diameters purchased from Polymicro Technologies, LLC. In order to create the electroosmotic flow in the buffer solution a Berten high voltage power Supply Model 205A-20R was used. In order to monitor the substances traveling through the capillary Ocean Optics Inc. light source (Mini-D2T), UV-Vis detector (USB2000), and capillary holder/sample cell (CUV-CCE) was integrated into the system. Figure V.7 displays of the capillary electrophoresis system that I built for separations and use in the fountain pen. In order to keep the user safe, thus preventing electric shock, I installed an Omron Corporation Safety Door Switch Model D4BS with the corresponding operation

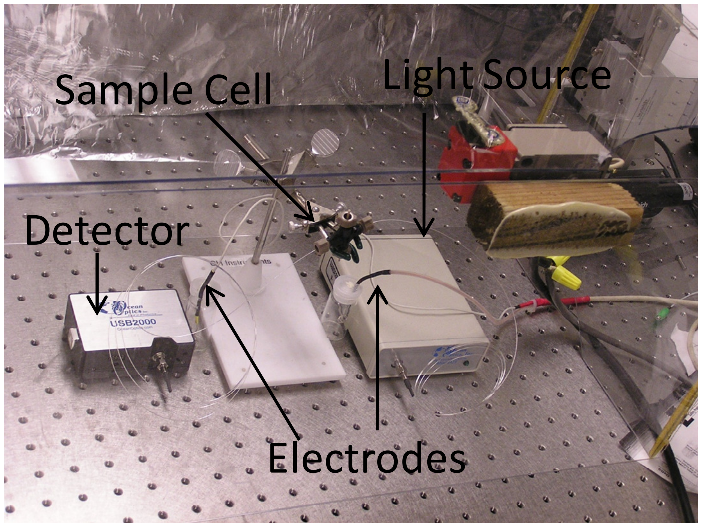

Figure V.7. Photograph of the capillary electrophoresis instrumentation.

key. This prevents the high voltage power supply from operating when the lid is opened.

3. Results and Discussions

A. Multipurpose Stage and Tip Holder. Figure V.8 is a photograph of the tip holder attached to the nanopositioner and the sample cell holder I affixed to the optical table. I constructed the tip holder and the legs of the stage using an acrylic polymer in order to prevent electrical conduction. In order to keep the electrode perpendicular to the plane of the substrate, I added leveling screws into the

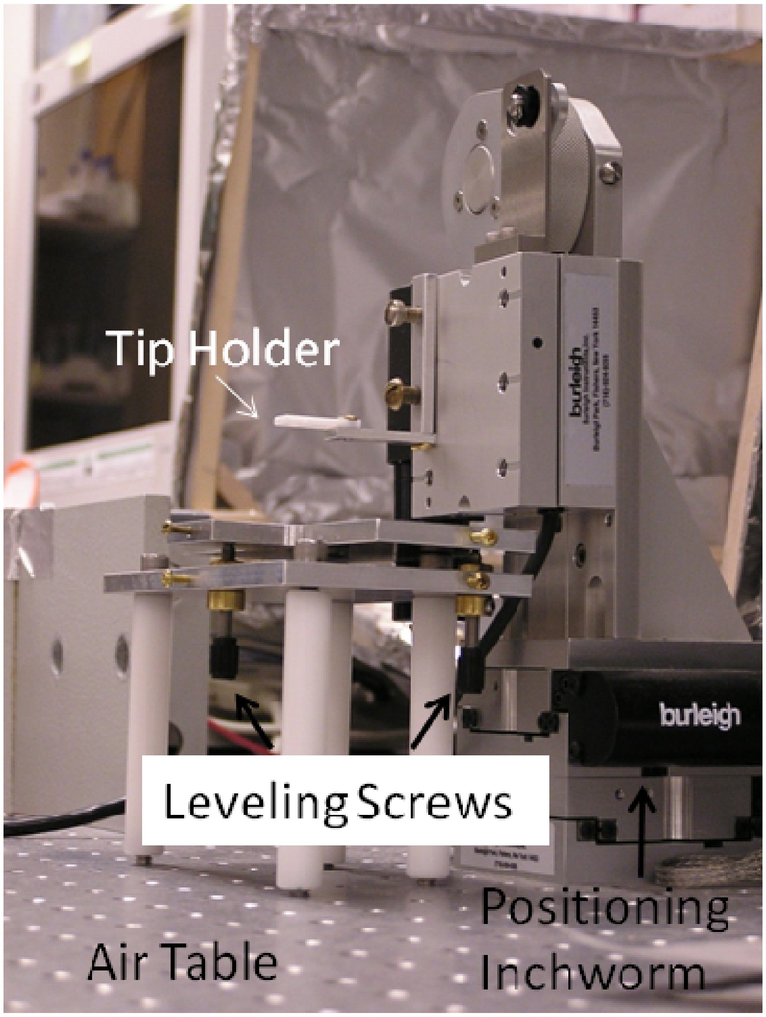
Tip Holder
burleigh
burleigh
Leveling Screws
Air Table
Positioning Inchworm

Figure V.8. SECM stage fixed to an air table with the UME tip holder attached to the xyz nanopositioners. Below the tip holder is the substrate platform with leveling screws.

design.

B. Capillary Electrophoresis Fountain Pen. Figure V.4 displays a schematic representation of the experimental set-up that I designed for the capillary electrophoresis fountain pen. I have secured an electrochemical microscope stage to the Burleigh 1500 three-axis nanopositioner on an optical table. The stage holds an electrochemical cell and it can be leveled using three leveling set screws. I have used a Cypress Systems Bipotentiostat Model EI-400 FCV to monitor the electrodes present in the system. I routed both the input and output from the bipotentiostat to the computer through a National Instruments BNC-2090. I directed the Burleigh Inchworm Controller 8200 to position the output of the capillary at the substrate. I have connected the Inchworm Controller directly to the computer through a GPIB card.

I made possible the analysis of the output of the capillary electrophoresis fountain pen by use of an Ocean Optics UV-Vis USB2000. I interfaced a high voltage source within the CEFP in order to create the electroosmotic flow through the capillary.

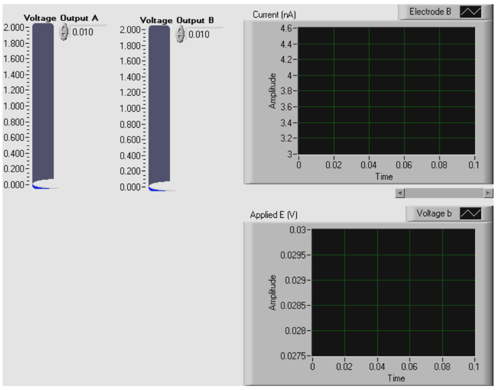
Voltage Output A
0.010
2.000
1.800
1.600
1.400
1.200
1.000
0.800
0.600
0.400
0.200
0.000
Voltage Output B
0.010
2.000
1.800
1.600
1.400
1.200
1.000
0.800
0.600
0.400
0.200
0.000
Current (nA)
Electrode B
Amplitude
4.6
4.4
4.2
4
3.8
3.6
3.4
3.2
3
0
0.02
0.04
0.06
0.08
0.1
Time
Applied E (V)
Voltage b
Amplitude
0.03
0.0295
0.029
0.0285
0.028
0.0275
0
0.02
0.04
0.06
0.08
0.1
Time

Figure V.9. Front panel of the program that controls the bipotentiostat

C. Computer Interface. In order to control the electrodes attached to the bipotentiostat I wrote a program in the LabVIEW programming environment.

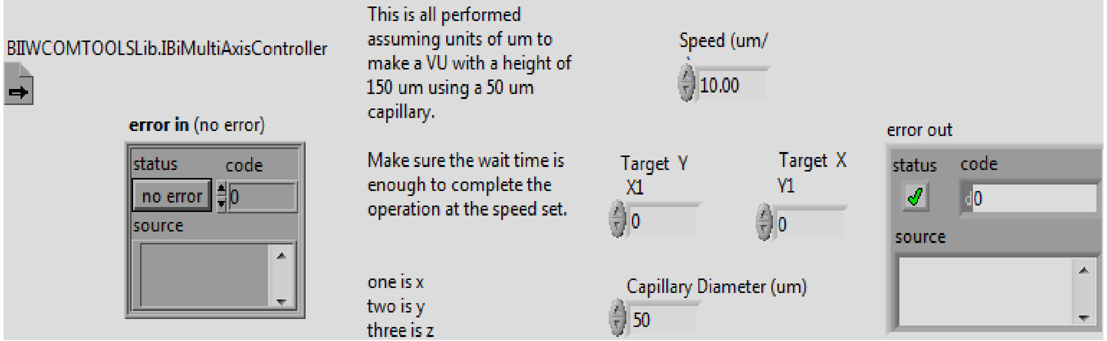
BIIWCOMTOOLSLib.IBiMultiAxisController

This is all performed assuming units of um to make a VU with a height of 150 um using a 50 um capillary.

Make sure the wait time is enough to complete the operation at the speed set.

one is x
two is y
three is z

error in (no error): status: no error; code: 0; source:

Speed (um/: 10.00

Target Y X1: 0

Target X Y1: 0

Capillary Diameter (um): 50

error out: status: ✓; code: 0; source:

Figure V.10. Front panel of the program that moves the tip in a pattern “VU.”

This program defines the output voltage for two WEs relative to a reference electrode while monitoring the current of the WEs. The front panel, which the scientist uses for the interface is presented in Figure V.9.

The desired deposition pattern was “VU.” In order to accomplish this I wrote a LabVIEW program that moved the capillary tip across the substrate in the shape of “VU.” The LabVIEW front panel, and user interface is

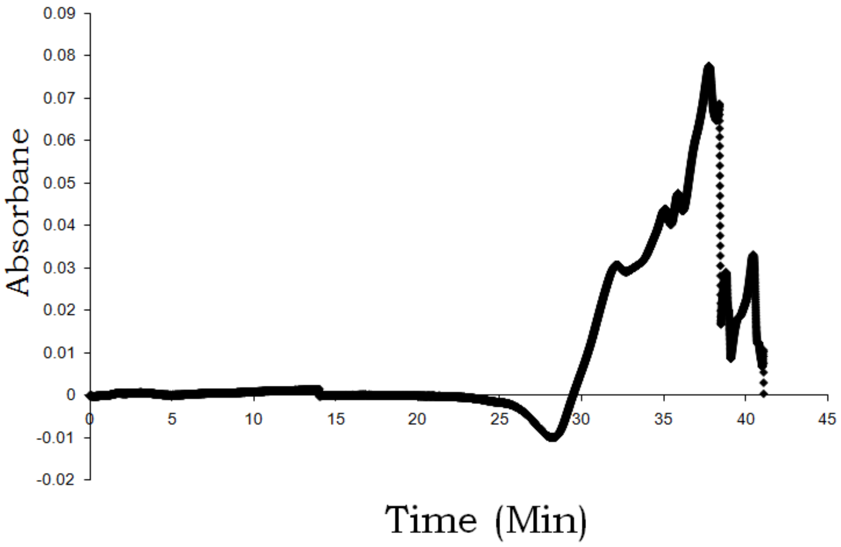

FigureV. 11. Electropherogram of the separation of Au MPCs. The electrophoretic mobility of the peak at 37 min is 2 x 10^{-5} cm^2 V^{-1} s^{-1}.

shown in Figure V.10.

D. Capillary Electrophoresis Separation. Figure V.11 shows an electropherogram of the separation of tiopronin protected Au MPCs in a borate buffer. The electropherogram shows the peak of the nanocrystals at 37 minutes for a separation using 20 kV. The nanocrystals in this solution present an electrophoretic mobility of 2 x 10^{-5} cm^2 V^{-1} s^{-1}. That results in 3.5 x 10^5 theoretical plates according to Equation (5).

$$N = \frac{\mu V}{2D_m} \qquad [5]$$

A 1 s pressure injection using 52 torr into the 50 μm diameter capillary results in 2.4 nL of analyte solution. At a sample concentration of 2 g ml^{-1} Au-tiopronin MPCs in borate buffer, that is ~5 x 10^{13} Au-tiopronin MPCs per injection. The total volume of a single injection could cover an area of 80 μm^2 at a coverage of 1 nmol cm^{-2}.

E. Monolayer Protected Cluster Deposition. I have used the capillary electrophoresis fountain pen for the deposition of nanoclusters in a 20 mM sodium borate buffer at pH 9.3. The ink used for the images shown in Figure 12 was Au-tiopronin MPCs. During the deposition process the MPCs were attached to a poly-L lysine film cast and dried on a glass slide. Figure V.12 displays optical images of two depositions via the CEFP.

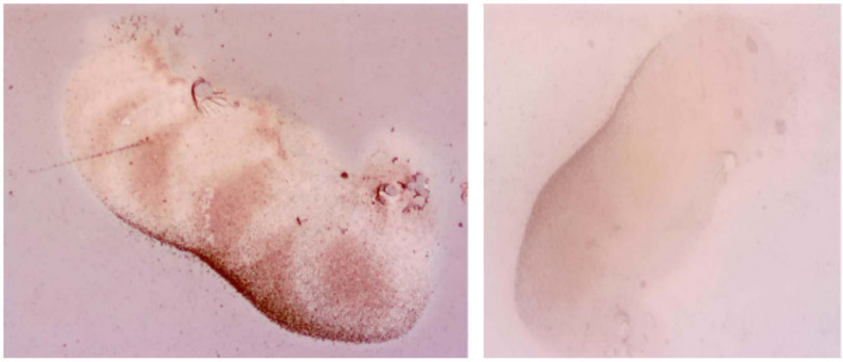

Figure V.12. Optical images of the deposition of Au protected MPCs on a poly-L-lysine cast on a glass slide.

4. Conclusions

I present in this chapter evidence of the viability for the capillary electrophoresis fountain pen. I have assembled the instrumentation, and I wrote the software in the LabVIEW programming environment. I separated Au-tiopronin MPCs with the CE and I integrated the CE apparatus with a micropositioner. I fastened a holder for the placement of the CE's capillary output at a substrate surface to the nanopositioner. I designed a cell holder for the substrate, and applied leveling screws for precision leveling. Finally, Au MPCs were deposited onto a poly-L-lysine coated glass substrate and these surfaces were subsequently imaged optically.

Ultimately, this instrument has been surpassed with the recent advances. The current state of fountain pen lithography shows great promise down many avenues. Beginning with the development of micropipettes for use as force probes in near-field scanning optical microscopy, the goal of applying these tips for patterning of substrates was forecast.[30] This research carried on to become a vehicle for the etching of a chrome substrate, which demonstrated the control of a chemical reaction at the 1 μm level.[31] For this procedure, a micropipette attached to a cantilever and the tip is brought in the vicinity of the substrate. The etchant in the pipette is forced onto the chrome substrate by use of a pressure regulator. As the cantilevered micropipette is moved the pattern is created on the substrate. This technique continued to develop into a vehicle for the patterning with biomaterials. Lines consisting of protein G were deposited on a substrate featuring an aldehyde group to create 500 nm wide lines that are 40 nm tall.[32] By using pressure in order to force the solution through the pipette a turbulent flow is created, using electoosmotic flow produces a laminar flow and more compact wave front. The ability to selectively deposit two different materials came with the introduction of the double barrel pipette by switching the polarity of the voltage in the circuit.[33] Rodolfa *et al.* used biotinylated DNA that was fluorescently labeled with a streptavidin coated glass substrate. By using different fluorescent markers, red alexa 647 and rhodamine green, in each barrel of the pipette they were able to exquisitely reproduce pieces of artwork with 1 μm pixels. By combining a feedback loop for z-axis control, pipette apertures of a 100 nm diameter and depositing patterns of two florescent molecules they have been able to produce fascinating pictures. However this technique does not provide the possibility for separation nor has a surface with a fuctional purpose, such as the deposition of nanoscale capacitors, been created. Most recently, a tapered glass pipette has been inserted into the place of an AFM cantilever tip, for the printing of BSA by use of a voltage drop across the glass capillary.[34] This advances the field of by combining the separation of a CE with the positioning precision of the AFM. This technique produced 50 nm tall features 500 nm wide. However, the strategy of using an AFM approach has a serious drawback, the feedback control of the z-axis position of requires the reflection of laser light in order to monitor the defection of the tip do to interaction with the substrate.

5. References

1. http://www.columbiapaint.com/tip6.php.

2. http://www.goldenglowpaints.com/Articles/GeneralArticles/Coldwthrptg.htm.

3. Bergh, S.; Guan, S.; Hagemeyer, A.; Lugmair, C.; Turner, H.; Volpe, A. F.; Weinberg, W. H.; Mott, G., *Appl. Catal., A* **2003,** *254* (1), 67-76.

4. Carlson, E.; Chandler, W.; Galdo, I.; Kudla, T.; Ta, C., *Jala* **2005,** *10* (6), 374-380.

5. http://www.ece.gatech.edu/research/labs/vc/theory/photolith.html.

6. Leuba, S. H.; Wheeler, T. B.; Cheng, C.-M.; Le Duc, P. R.; Fernandez-Sierra, M.; Quinones, E., *Methods (Amsterdam, Neth.)* **2009,** *47* (3), 214-222.

7. Braunschweig, A. B.; Huo, F.; Mirkin, C. A., *Nature Chemistry* **2009,** *1* (5), 353-358.

8. Grainger, D. W.; Castner, D. G., *Adv. Mater. (Weinheim, Ger.)* **2008,** *20* (5), 867-877.

9. Jiang, X.; Bent, S. F., *J. Phys. Chem. C* **2009,** *113* (41), 17613-17625.

10. Henzie, J.; Lee, J.; Lee, M. H.; Hasan, W.; Odom, T. W., *Annual Review of Physical Chemistry* **2009,** *60*, 147-165.

11. Xia, Y.; Whitesides, G. M., *Angew. Chem. Int. Ed.* **1998,** *37*, 550-575.

12. Mukherjee, R.; Sharma, A.; Patil, G.; Faruqui, D.; Pattader, P. S. G., *Bull. Mater. Sci.* **2008,** *31* (3), 249-261.

13. Cavallini, M.; Albonetti, C.; Biscarini, F., *Adv. Mater. (Weinheim, Ger.)* **2009,** *21* (10-11), 1043-1053.

14. Akbulut, O.; Yu, A. A.; Stellacci, F., *Chem. Soc. Rev.* **2010,** *39* (1), 30-37.

15. Odom, T. W.; Love, J. C.; Wolfe, D. B.; Paul, K. E.; Whitesides, G. M., *Langmuir* **2002,** *18*, 5314-5320.

16. Wang, X.; Ryu, K. S.; Bullen, D. A.; Zou, J.; Zhang, H.; Mirkin, C.; Llu, C., *Langmuir* **2003,** *19* (21), 8951-8955.

17. Li, H.; Sims, C. E.; Wu, H. Y.; Allbritton, N. L., *Analytical Chemistry* **2001,** *73*, 4625-4631.

18. Xia, Y.; Whitesides, G. M., *Annual Review of Material Science* **1998,** *28*, 153-184.

19. Piner, R. D.; Zhu, J.; Xu, F.; Hong, S.; Mirkin, C., *Science* **1999,** *283*, 661-663.

20. Haaheim, J.; Nafday, O. A., *Scanning* **2008,** *30* (2), 137-150.

21. Weinberger, R., *Practical Capillary Electrophoresis*. 2nd ed.; Academic Press: New York, 2000.

22. Sims, C. E.; Meredith, G. D.; Krasieva, T. B.; Berns, M. W.; Tromberg, B. J.; Allbritton, N. L., *Analytical Chemistry* **1998,** *70*, 4570-4577.

23. Bard, A. J.; Faulkner, L. R., *Electrochemical Methods: Fundamentals and Applications*. 2nd ed.; Wiley: New York, 2000.

24. Templeton, A. C.; Cliffel, D. E.; Murray, R. W., *J. Am. Chem. Soc.* **1999,** *121*, 7081-7089.

25. Link, S.; El-Sayed, M. A., *Annu. Rev. Phys. Chem.* **2003,** *54*, 331-366.

26. Wilson, M.; Kannangara, K.; Smith, G.; Simmons, M.; Raguse, B., *Nanotechnology: Basic Science and Emerging Technologies*. Chapman & Hall/CRC: New York, 2002.

27. Eckhard, K.; Etienne, M.; Schulte, A.; Schuhmann, W., *Electrochem. Commun. FIELD Full Journal Title:Electrochemistry Communications* **2007,** *9* (7), 1793-1797.

28. Brauer, G., *Handbook of Preparative Inorganic Chemistry*. Academic Press: New York, 1963.

29. Templeton, A. C.; Chem, S.; Gross, S. M.; Murray, R. W., *Langmuir* **1999,** *15*, 66-76.

30. Shalom, S.; Lieberman, K.; Lewis, A.; Cohen, S. R., *Rev. Sci. Instrum.* **1992,** *63* (9), 4061-5.

31. Lewis, A.; Kheifetz, Y.; Shambrodt, E.; Radko, A.; Khatchatryan, E.; Sukenik, C., *Applied Physics Letters* **1999,** *75* (17), 2689-2691.

32. Taha, H.; Marks, R. S.; Gheber, L. A.; Rousso, I.; Newman, J.; Sukenik, C.; Lewis, A., *Applied Physics Letters* **2003,** *83* (5), 1041-1043.

33. Rodolfa, K. T.; Bruckbauer, A.; Zhou, D.; Korchev, Y. E.; Klenerman, D., *Angew. Chem., Int. Ed.* **2005,** *44* (42), 6854-6859.

34. Lovsky, Y.; Lewis, A.; Sukenik, C.; Grushka, E., *Anal. Bioanal. Chem.* **2010,** *396* (1), 133-138.

APPENDIX

1. Atomic Force Microscopy of PSI and related substrates

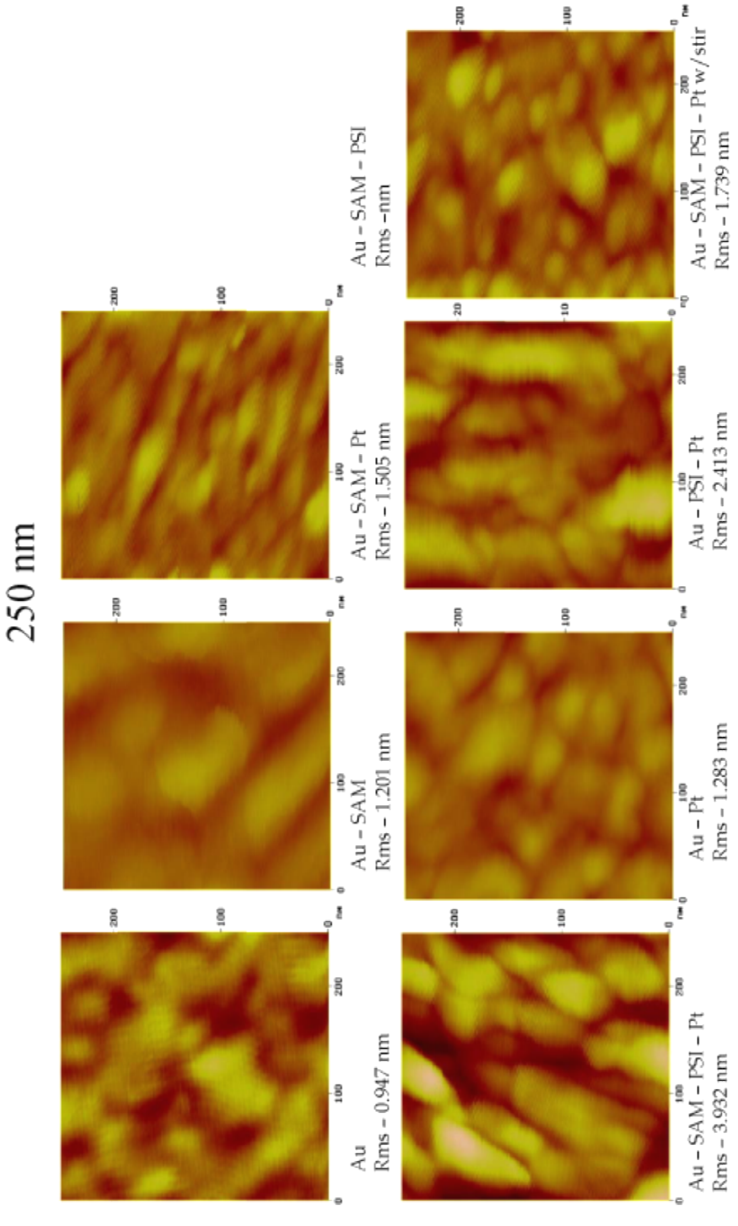
250 nm
Au
Rms – 0.947 nm
Au – SAM
Rms – 1.201 nm
Au – SAM – Pt
Rms – 1.505 nm
Au – SAM – PSI
Rms –nm
Au – SAM – PSI – Pt
Rms – 3.932 nm
Au – Pt
Rms – 1.283 nm
Au – PSI – Pt
Rms – 2.413 nm
Au – SAM – PSI – Pt w/stir
Rms – 1.739 nm

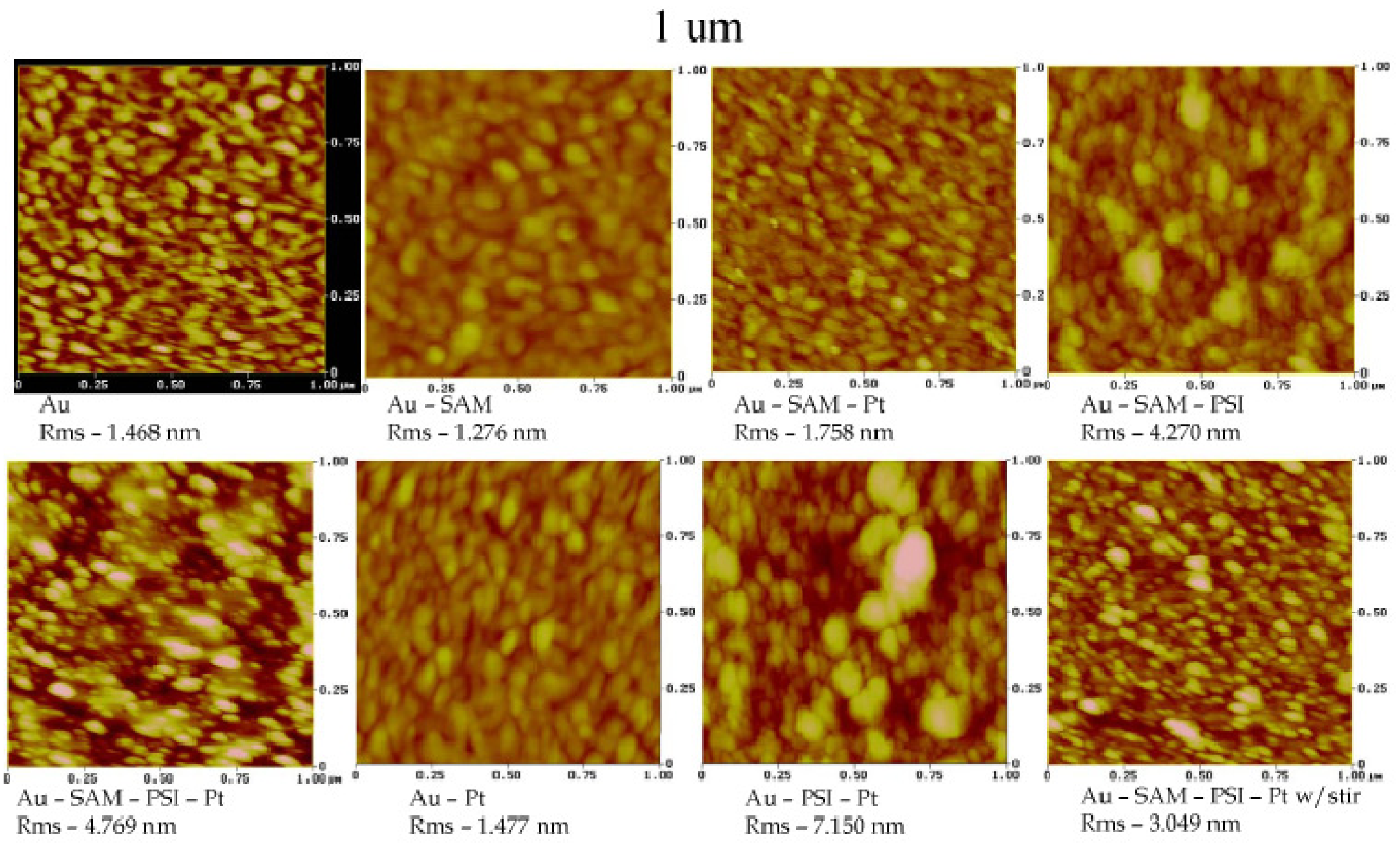
1 um
0
0.25
0.50
0.75
1.00 µm

Au
Rms – 1.468 nm

Au – SAM
Rms – 1.276 nm

Au – SAM – Pt
Rms – 1.758 nm

Au – SAM – PSI
Rms – 4.270 nm

Au – SAM – PSI – Pt
Rms – 4.769 nm

Au – Pt
Rms – 1.477 nm

Au – PSI – Pt
Rms – 7.150 nm

Au – SAM – PSI – Pt w/stir
Rms – 3.049 nm

5 um

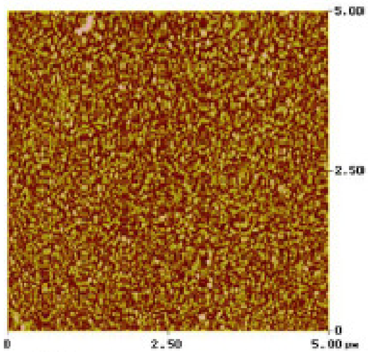
5.00
2.50
0
0
2.50
5.00 µm

Au
Rms – 1.617 nm

Au – SAM
Rms –nm

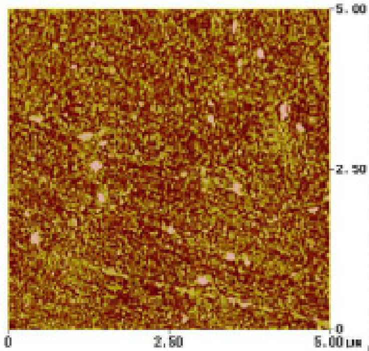
5.00
2.50
0
0
2.50
5.00 µm

Au – SAM – Pt
Rms – 2.002 nm

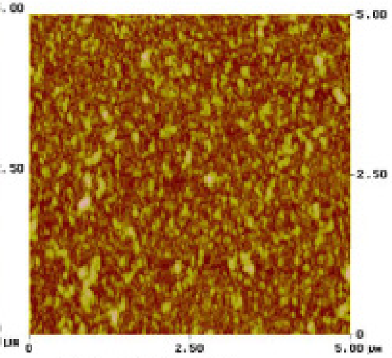
5.00
2.50
0
0
2.50
5.00 µm

Au – SAM – PSI
Rms – 4.993 nm

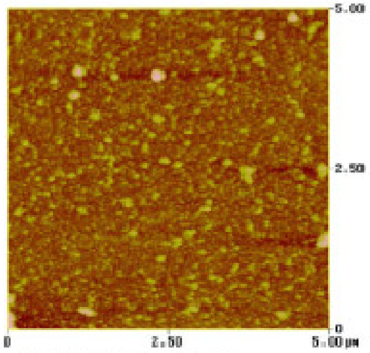
5.00
2.50
0
0
2.50
5.00 µm

Au – SAM – PSI – Pt
Rms –nm

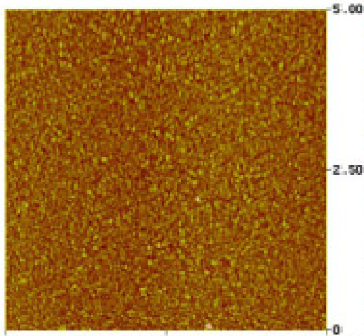
5.00
2.50
0
0
2.50
5.00 µm

Au – Pt
Rms – 1.561 nm

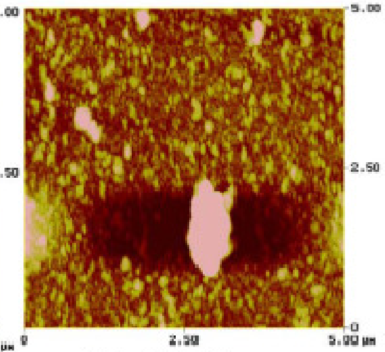
5.00
2.50
0
0
2.50
5.00 µm

Au – PSI – Pt
Rms – 18.397 nm

Au – SAM – PSI – Pt w/stir
Rms –nm

2. PSI Extraction

The Day Before: Prep

2 buffers, 1 medium, and the spinach (All need to be stored in the fridge overnight)

Column Buffer: 0.01 M Phosphate Buffer pH 7.0

Na_2HPO_4 – 1.0186 g

NaH_2PO_4 – 0.8556 g in 1 L H_2O

Adjust to pH 7.0 with NaOH

Elution Buffer: 0.2 M Phosphate Buffer pH 7.0 with Triton-X (0.05% wt/vol)

Na_2HPO_4 – 20.6146 g

NaH_2PO_4 – 16.9878 g

Triton X-100 – 0.5 g in 1 L H_2O

Triton – In order to get the triton in solution, first dissolve the other components of the solution in water. Carefully, weigh out the triton on the corner of a small weighing boat. Use a pipette to spray the solution onto the triton containing weigh boat while allowing it to run into the beaker, this probably needs to be done a dozen time to get all of the triton. Feel the weigh boat; if it feels soapy you did not get all of the triton. Start over.

Adjust to pH 7.0 with NaOH

Re-suspending Medium: 50 mM HEPES pH 7.6

Sorbitol - 6.0116 g

EDTA – 0.0584 g

$MgCl_2 \times 6H_2O$ – 0.0203 g

MnCl2 x 4H2O – 0.0198 g

HEPES - 1.1915 g --- 4-(2-Hydroyethyl)- 1- piperazineethane solfonic acid

Triton X-100 – 1.0 g

See the note on Triton under elution buffer

Adjust to pH 7.6 with NaOH

Spinach:

All of the center veins and the major side veins should be trimmed away (they are too coarse and in the macerating process damage the PSI). Also remove any sections that are discolored or damaged.

Get the freshest **Baby** spinach you can find. A single bag from Harris Teeter gives over forty grams when trimmed.

Regenerating Buffer: 0.5 M Phosphate Buffer pH 7.0

This is supposed to regenerate the column, but I have never done it

Na_2HPO_4 – 25.7347 g

NaH_2PO_4 – 21.2504 g in 500 mL H_2O

Adjust to pH 7.0 with NaOH

The problem, I was told, is that the reused column becomes more compact as the separation continues, this slows, or completely halts, the flow of the solution.

The Day of: The Extraction

Grinding Medium: pH 6.5

Sorbitol – 18.04 g

$Na_4P_2O_7$ x10 H_2O – 1.34 g – Sodium Pyrophosphate

$MgCl_2$ x 6H_2O – 0.24 g

Sodium Ascorbic Acid – 0.11g in 300 mL H_2O

Adjust to pH 6.5 with HCl and place in the freezer

Hydroxylapatite Column

The separation is performed in a 3 cm diamerter jacketed column. Set this up with the pump in ice water before the hydroxylapatite is ready to pour. Replenish the ice so that it does not all melt.

Hydroxylaapatite – 15 g in 300 mL **Column Buffer**

Gently add the hydroxyapatite to the column buffer while swirling the slurry. Check the bottom of the flask for chunks and break them with a glass stir rod. Once it is homogeneous let the gel settle until the supernatant is clear and decant off the supernatant except for a volume equal to the volume of the hydroxylapatite. Keeping a volume of supernatant equal to the volume of HA. Resuspend and rinse the hydroxylapatite two additional times with column buffer. After the final rinse decant down to a milky white and quickly pour this slurry, while swirling the flask, onto one inch of column buffer. Let the hydroxylapatite settle and drain the buffer. Carefully pipette two full loads of the column buffer onto the column, without disturbing the top layer of the column bed, in order to rinse the column. Use a long pipette to bring the column buffer directly above the solution and slowly drain the buffer, try to avoid any force that would dent the hydroxylapatite bed. The buffer that exits the column should be at the same pH as the column buffer prepared the day before, (pH 7). If this did not occur rinse the column again with the column buffer. Try to leave the column with as little buffer left (1 mL) as possible without letting the top of the column go dry. Wrap the column in Al foil to block any stray light.

Centrifugation:

Make sure that the centrifuge is set up to run at 4 ^{o}C with the proper centrifuge tube and holder are installed. Centrifuge tube holder F0850 should be used initially with the larger tubes and holder F0630 is for use with the smaller tubes.

The Cart:

I used the centrifuge in the Wright Lab for the extractions I performed. This required a cart with the following items:

- On ice in cooler
    - Centrifuge tubes, some filled (8 large) and some empty (2 small)
    - Resuspending medium
- Pipettes
- Cotton swabs
- Kimwipes
- Waste beaker

Macerating Spinach:

Remove the grinding medium from the freezer and shake it. It should be the consistency of melted snow. If there is a significant amount of ice, let it thaw a few minutes. If it is too icy the extraction may not work. Turn off the lights. Add the spinach to the food processor followed by the grinding medium. The spinach leaves should be homogenized in the grinding medium when it looks like melting snow. Several quick bursts (~ 4) from the food processor should accomplish this.

Pass the mixture through 2 layers of cheesecloth into a 600 ml beaker, followed by 8 layers into a 500 mL Erlenmeyer flask, which is being chilled on ice in a large crystallizing dish. Squeeze the liquid out so that in excess of 200 mL of a green solution is produced. Quickly add **exactly** 25 mL to each of eight centrifuge tubes. The tubes should be packed on ice in a Styrofoam cooler and brought to the centrifuge.

The first centrifuging process in tube holder F0850 should be at 8000 RCF for 5s. As you place the tubes in the centrifuge make sure the outside of the tubes are dry and free from ice, using a Kimwipe. The supernatant should be poured off and the pellet resuspended in two pipette fulls (about 3 mL) of, guess what, resuspending buffer. Resuspendion should be assisted with cotton swabs on a stick. Add the current contents of four of the initial centrifuge tubes to each of the two smaller tubes and make sure they have identical volumes, and are dry and free of ice, before centrifuging. The second centrifuging process takes place in tube holder F0630 should be at 20000 RCF for 15 minutes. (All times start once the centrifuge speed has been reached.) The supernatant should still be dark green after this process. If not, start the extraction all over again.

Separation:

With the lights off, pipette the dark green supernatant onto the column quickly and carefully; do not to disturb the top of the column bed. Drain all of the supernatant into the column bed; leave as little as possible (~ 1ml) without exposing the top of the column to air. Refill with column buffer minimizing mixing and damage to the top of the column bed. Run column buffer through the column until the elutant is clear. After the first clear drops, run a full column of column buffer through; drain it until their is almost no liquid on top of the bed, without running it dry. Fill with elution buffer. Pass the buffer through to waste until the elutant contains green. Catch this product, on ice until done. Pipette 1mL of this elutant into microcentrifuge tubes, swirl the solution frequently so that it is homogeneous, you are aiming for between 17 and 25 mL, keep these on ice. Do not collect any fraction passed ~ 25 – 30 mL. Keep one of these in the fridge, the rest should be placed into a –80 ^{o}C freezer, I use the one in the Stone Lab

The Day After: Quantification

Get to work early in order to defrost PSI. Remove the PSI from the Deep Freeze (-80 ^oC) and place it in the refrigerator for 6 hours before it is ready to be used. Check the one that was left in the refrigerator overnight for any separation or solids that crashed out of solution. If the PSI left overnight in the refrigerator appears inhomogeneous, it is probably best to redo the extraction.

Be sure that all of the glassware has been rinsed with acetone to remove all PSI from the last quantification. (unless it is plastic that will dissolve in acetone and thus not glassware)

Part 1 – Solutions required:

1. 80% Acetone (High grade HPLC) / 20% water by volume – 25 mL total

2. For the Oxidation of PSI. 1 M $K_3Fe(CN)_6$ 3.293 g in 10 mL water. Wrap in Al foil it is light sensitive. This solution requires stirring for the salt to dissolve

3. For the Reduction of PSI. 0.5 M Sodium Ascorbate (not the ascorbic acid) 5 mM dithiothreitol (in the fridge). 0.0991 g sodium ascorbate and 0.0008 g of dithiothreitol in 1mL water. Wrap solution in Al foil it is light sensitive.

4. BABA Assay buffer: it is easiest to make this solution in a small beaker

a. 50 mM Tricine	0.8959 g
b. 0.1 M Sorbitol	1.8217 g
c. 0.01 NaCl	0.0585 g
d. 0.05% Triton	0.05g

See the note on Triton under Elution Buffer

In 100 mL water adjusted to pH 7.8 with NaOH

5. 50 mM Phosphate buffer pH 7.0 – you can buy this in the stockroom. It is the normal buffer used for the standardization of a pH meter

6. Filter Spinach Extract. This proves to be more difficult than one would expect. First, the lights must be off so the PSI is not degraded, it doesn't have the leaf to protect it anymore. Second, invert the microcentrifuge tube that the extract is stored and defrosted in, this is done to make sure the solution is homogeneous. Slowly filter the PSI containing extract in to a different microcetrigure tube through a 0.2 um filter. This is difficult because pressure may build up and some of the extract can squirt out. In order to prevent this go very slowly, especially near the end of the filtering. Near the end of the filtering process, pushing the syringe so that 0.05 mL is dispensed could still be more than the system can handle. Losing a few tenths of a mL does not sound bad, but because some of the material you want to quantify remains is the filter in addition to the material that you lose causes the concentration to drop. Some of these problems were eliminated when the frit of the column was changed to a 30 mm disk with porosity of 25 – 50 um. (From Ace Glass – Fritted Ware – Glass disc pore C 7176-29)

   The first drop or two out of the filter is clear, containing neither chlorophylls nor PSI. As you continue to pass the solution through the filter chorophylls and PSI are able to pass. If some of the solution is lost the final concentration will not represent a properly filtered solution, and thus is not comparable to previous work. Remember, you worked all day yesterday to get this stuff out of the plant, than you had to wait 6 hours to defrost it, if you lose even 0.1 mL the work has been wasted!!

Part 2 – The Analysis:

1. A dual beam UV-Vis from 350 – 750 in phosphate buffer.

   Cuvette one – the reference cuvette to be placed in the far slot – 2500 uL Phosphate buffer.

Cuvette two – the sample cuvette near slot in the UV-Vis – 2450 uL Phosphate buffer and 50 uL filtered spinach extract. Be sure to invert the solution on the way to the spectrophotometer to be sure it is well mixed.

Use kimwipes to make sure there are no fingerprints on the cuvettes.

If the features so not show up in the assay, after you repeat the analysis, there is no need to continue with the other experiments.

2. Single beam experiment. 2500 uL of Acetone/Water mixture compared to 2450 uL Acetone/Water plus 50 uL Spinach extract. Mix by inverting, use the caps or acetone will evaporate. The absorbance of these solutions need to be compared and recorded at 645 nm, 652 nm, 663 nm, in this order. Set-up menu parameters requiring modification are: single beam, 5 replicates, and the wavelength. When the zero button is pressed it will ask for the blank, and when you start a run, the sample will be requested. Be sure to hold the cuvettes with Kimwipes.

3. A dual beam UV-Vis from 650 nm -750 nm of the PSI in the BABA assay

   Each cuvette should have 2275 uL of BABA assay and 100 uL PSI. Mix by inverting. Take the scan, repeat the scan after five minutes. Add 120 uL water to the reference cuvette. Simultaneously add 5 uL of Na-ascorbate solution to the reference cuvette and 125 uL of the potassium ferricyanide solution. Quickly invert both cuvettes and run scan. Wait 15 minutes and run the scan again. Export the 5 minute baseline and the 15 minute scan into an excel file and subtract the two runs. Take the difference between the isosbestic point (725 nm) and the peak. This value and the three values from the single wavelength experiments to give the chlorophyll totals and the PSI ratio.

nm	645	652	663	Chl a	Chl b	a/b	Total Chl	Chl a [mg/mL]	Chl b [mg/mL]	**Chl total [mg/mL]**	Chl total [mMol/mL]	A for diluted P700	total A	P700 [mMol/mL]	**PSI type**
sample 1	0.0401	0.0617	0.1128	0.0013	0.0004	3.39	0.0018	0.07	0.02	**0.09**	0.00010	0.00885	0.221	3.457E-06	**29**
				(0.0127*D7)-(0.00269*B7)		E7/F7		E7*50		**H7*50**			M7*25		
					(0.0229*B7)-(0.00468*D7)		C7/34.5		F7*50		K7/900			(N7/64000)	

The values that you enter are the absorbance values for 645 nm, 652 nm, 663 nm and A for diluted p700. The rest is calculated according to the equation below the value for the example.

3. LabVIEW Programs

A. Monitor Electrodes

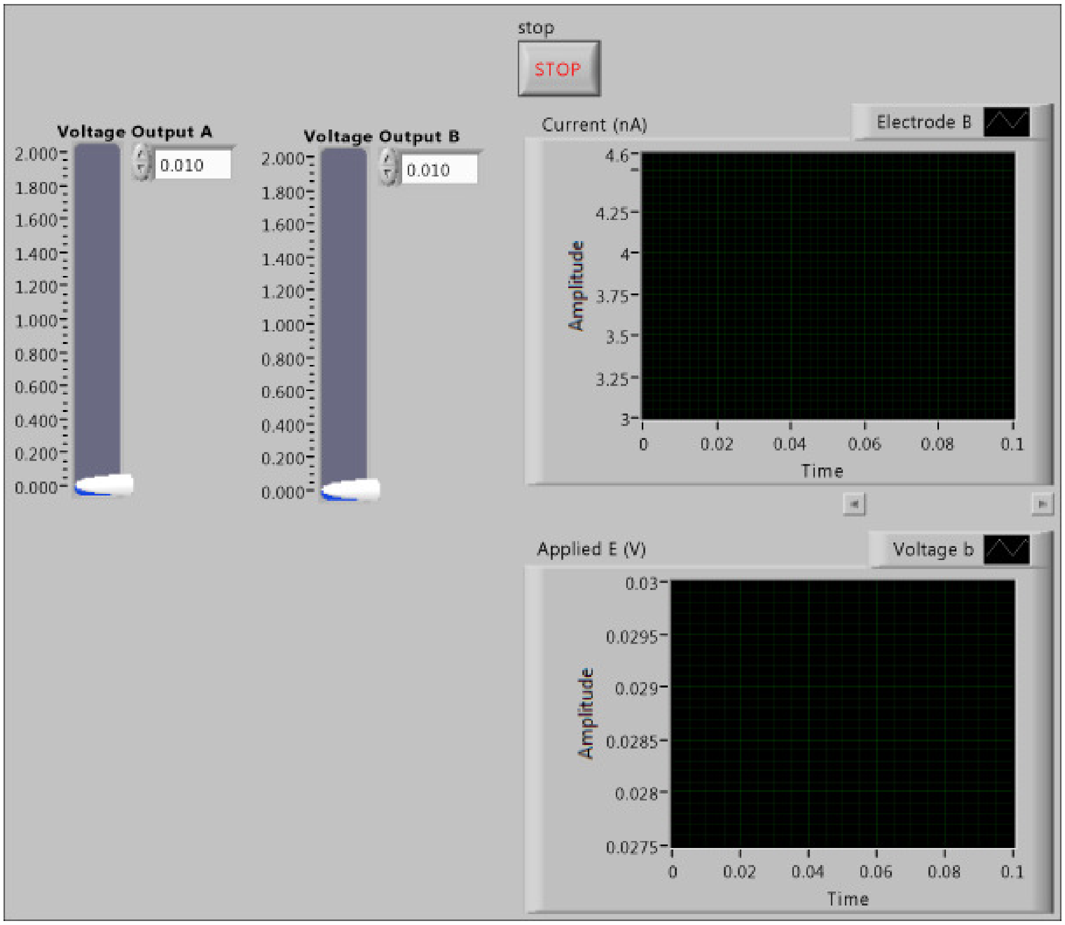

Voltage Output A 0.010

Voltage Output B 0.010

stop
STOP
2.000
1.800
1.600
1.400
1.200
1.000
0.800
0.600
0.400
0.200
0.000
Current (nA)
Electrode B
Amplitude
4.6
4.25
4
3.75
3.5
3.25
3
0
0.02
0.04
0.06
0.08
0.1
Time
Applied E (V)
Voltage b
0.03
0.0295
0.029
0.0285
0.028
0.0275

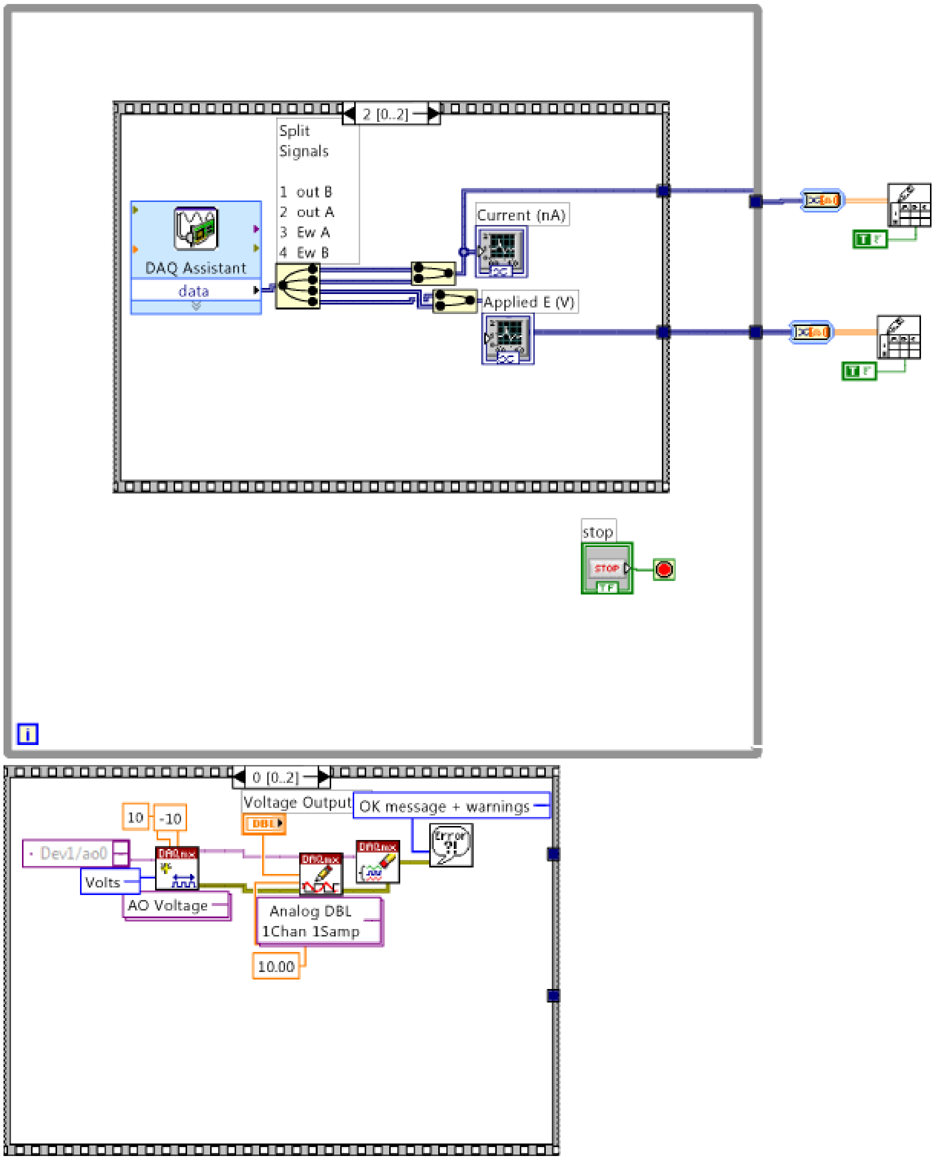
2 [0..2]
Split Signals
1 out B
2 out A
3 Ew A
4 Ew B
DAQ Assistant
data
Current (nA)
Applied E (V)
stop
STOP
TF
0 [0..2]
Voltage Output
DBL
OK message + warnings
10
-10
Dev1/ao0
Volts
AO Voltage
DAQmx
Analog DBL 1Chan 1Samp
10.00

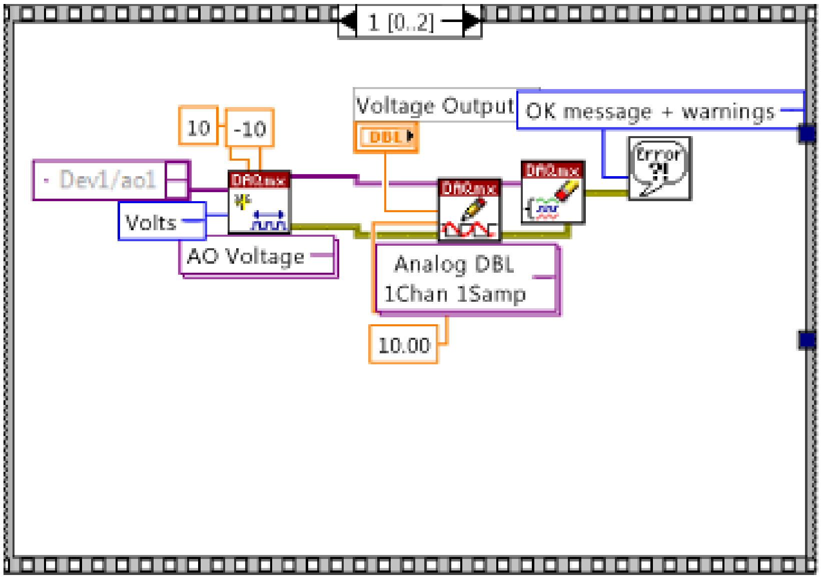
1 [0..2]
10
-10
Dev1/ao1
Volts
AO Voltage
Voltage Output
DBL
DAQmx
Analog DBL
1Chan 1Samp
10.00
OK message + warnings
Error ?!

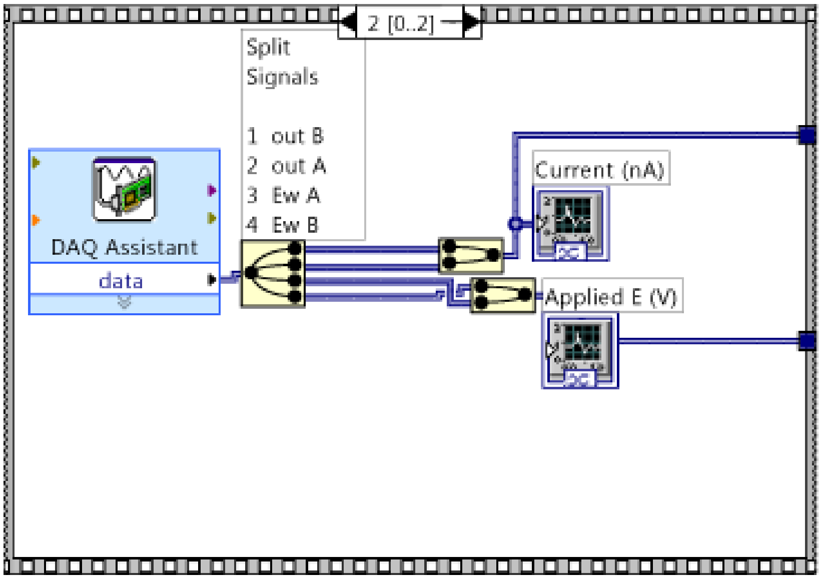
2 [0..2]
Split
Signals
1 out B
2 out A
3 Ew A
4 Ew B
DAQ Assistant
data
Current (nA)
Applied E (V)

B. Movement in Shape of "VU"

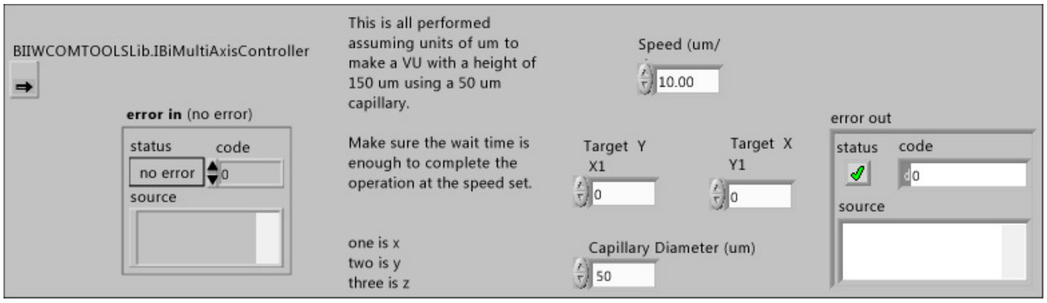

BIIWCOMTOOLSLib.IBiMultiAxisController

This is all performed assuming units of um to make a VU with a height of 150 um using a 50 um capillary.

Make sure the wait time is enough to complete the operation at the speed set.

one is x
two is y
three is z

Speed (um/ 10.00

error in (no error)
status: no error
code: 0
source

Target Y X1: 0

Target X Y1: 0

Capillary Diameter (um): 50

error out
status: ✓
code: 0
source

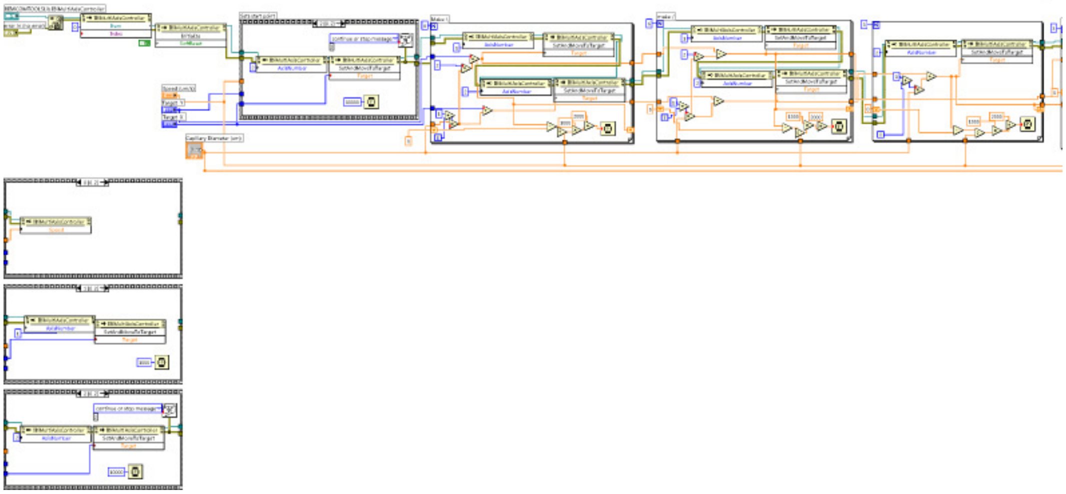

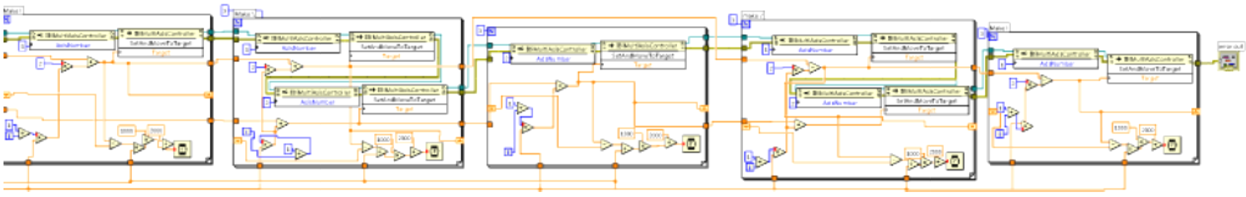

C. Movement of Inchworm (GPIB)

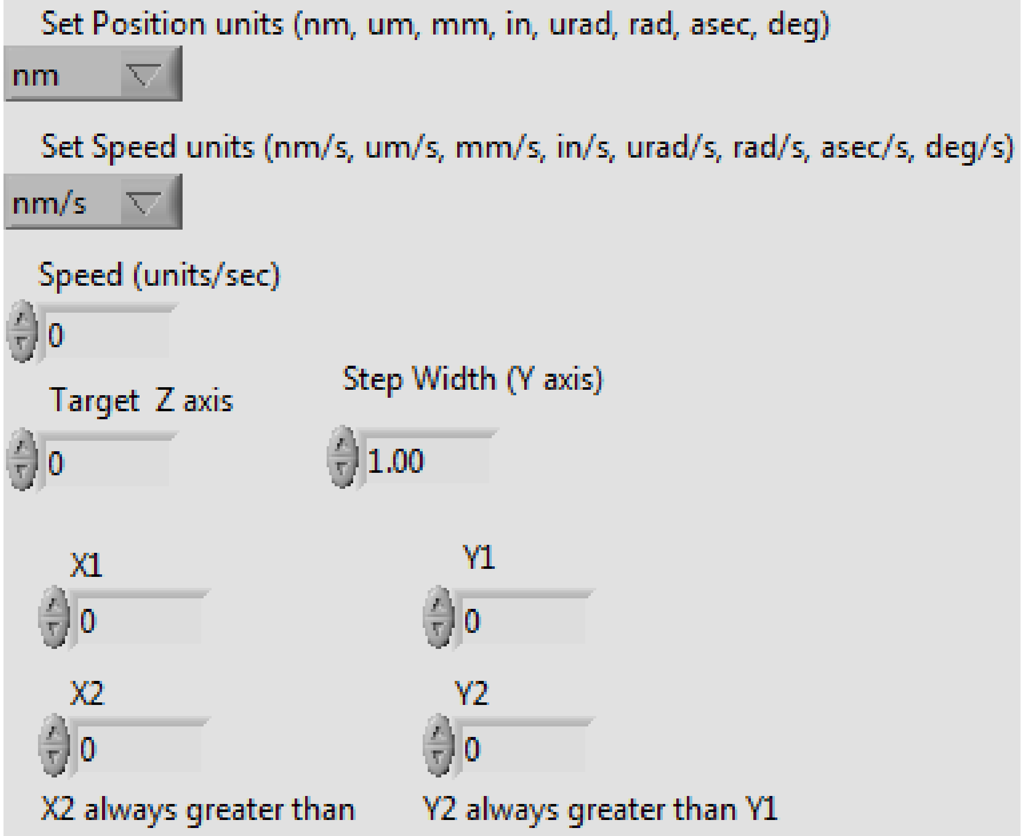

Set Position units (nm, um, mm, in, urad, rad, asec, deg)
nm

Set Speed units (nm/s, um/s, mm/s, in/s, urad/s, rad/s, asec/s, deg/s)
nm/s

Speed (units/sec)
0

Target Z axis
0

Step Width (Y axis)
1.00

X1
0

Y1
0

X2
0

Y2
0

X2 always greater than

Y2 always greater than Y1

Block Diagram

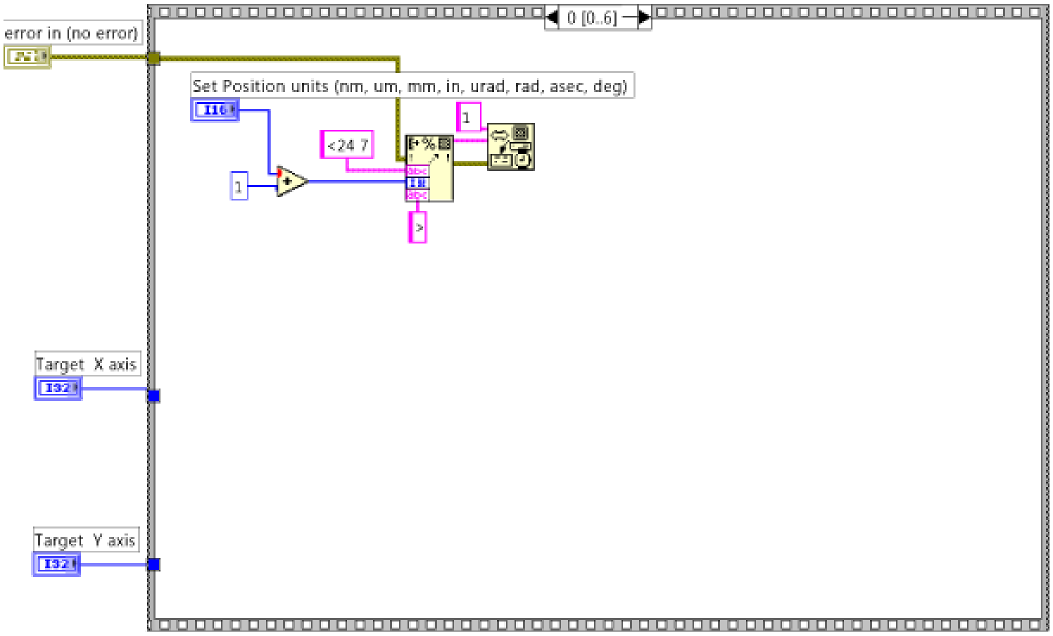
error in (no error)
0 [0..6]
Set Position units (nm, um, mm, in, urad, rad, asec, deg)
I16
1
<24 7
1
I8
>
Target X axis
I32
Target Y axis
I32

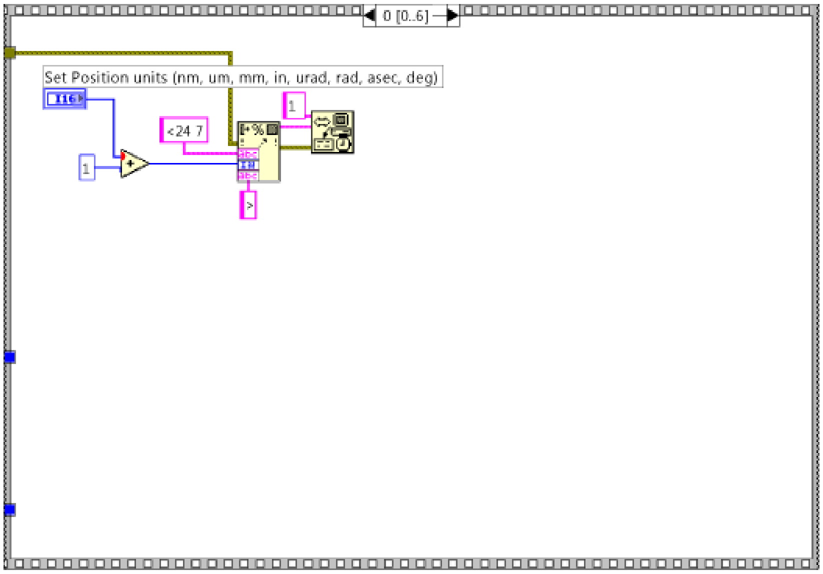
0 [0..6]
Set Position units (nm, um, mm, in, urad, rad, asec, deg)
I16
1
<24 7
1
>

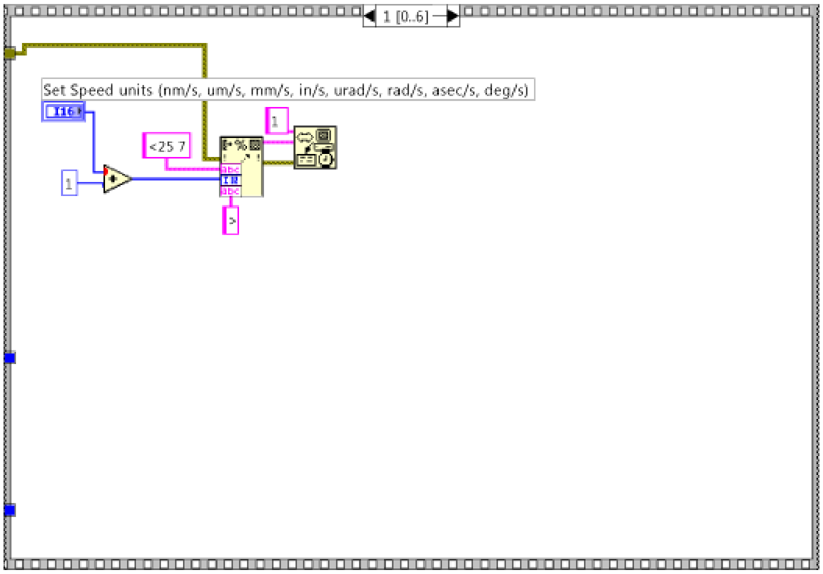
1 [0..6]
Set Speed units (nm/s, um/s, mm/s, in/s, urad/s, rad/s, asec/s, deg/s)
I16
1
<25 7
1
>

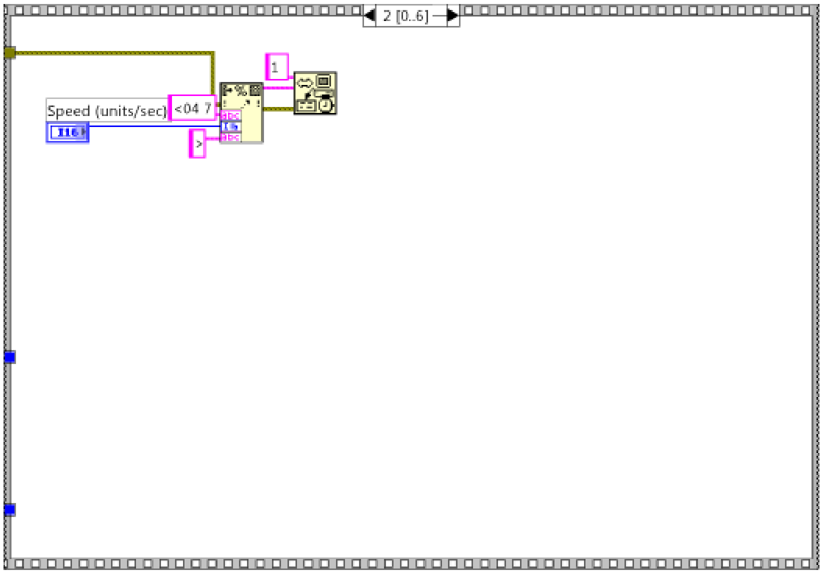
2 [0..6]
Speed (units/sec)
<04 7
I16
>
1

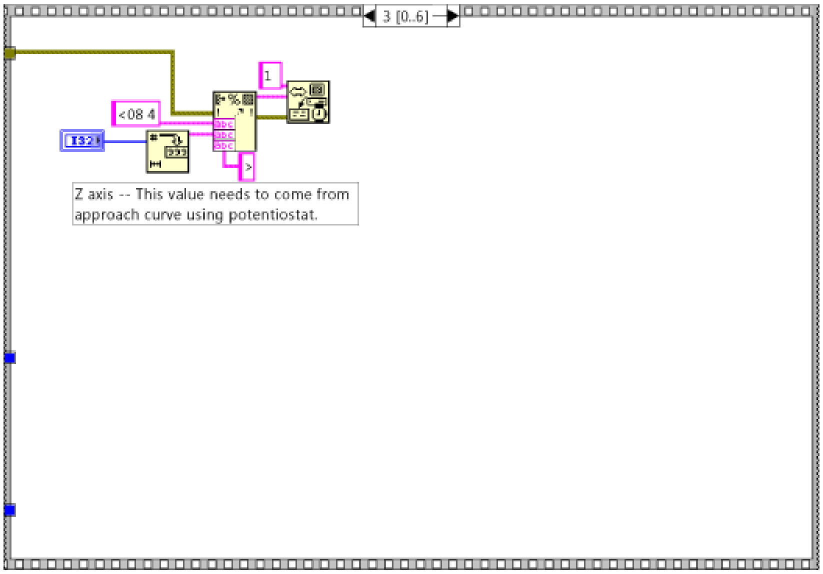
3 [0..6]
<08 4
I32
>
1

Z axis -- This value needs to come from approach curve using potentiostat.

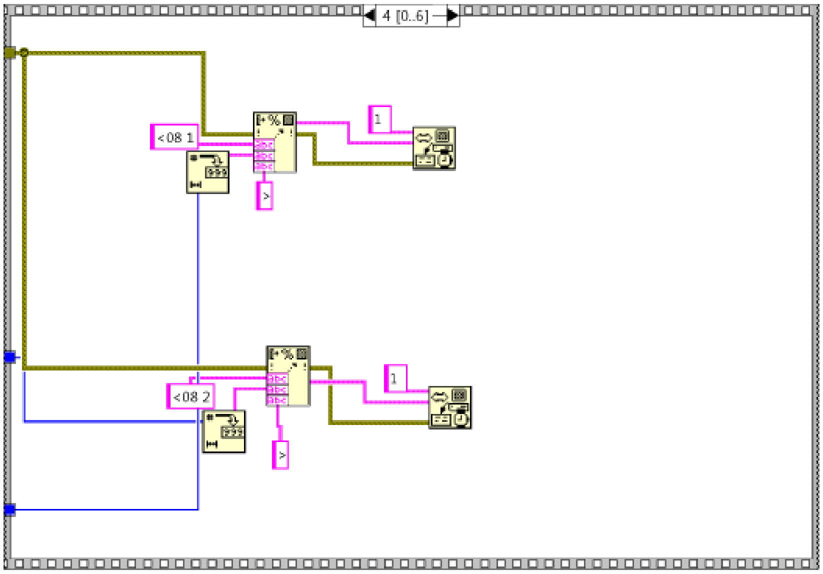
4 [0..6]
<08 1
1
>
<08 2
1
>

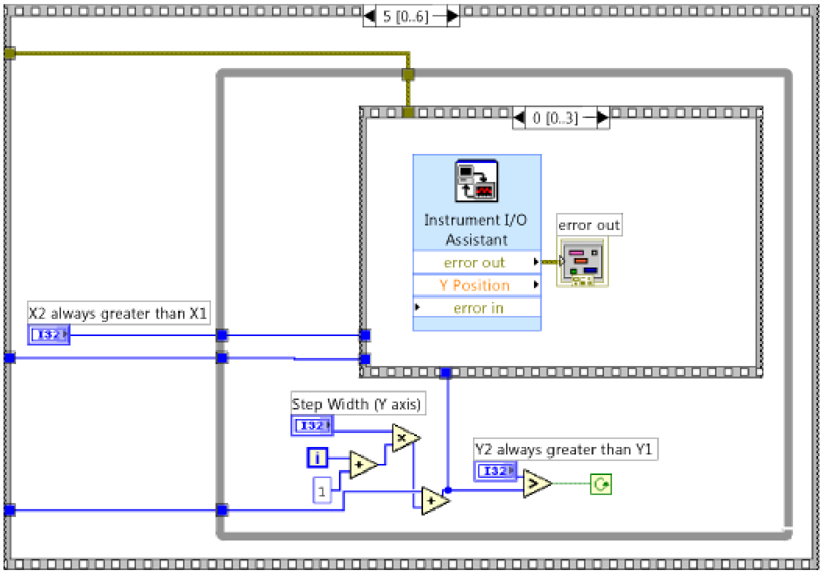
5 [0..6]
0 [0..3]
Instrument I/O Assistant
error out
Y Position
error in
error out
X2 always greater than X1
I32
Step Width (Y axis)
I32
i
1
Y2 always greater than Y1
I32

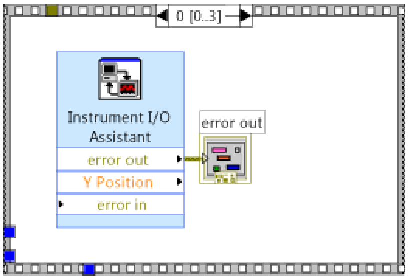
0 [0..3]
Instrument I/O Assistant
error out
Y Position
error in
error out

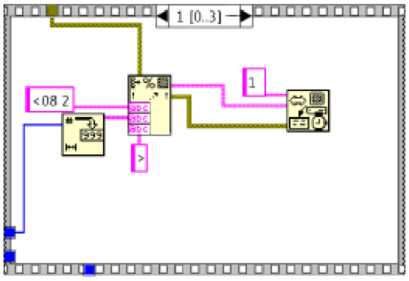
1 [0..3]
<08 2
1
>

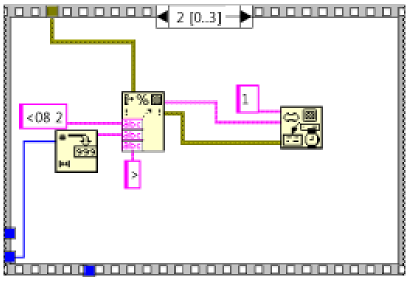
2 [0..3]
<08 2
1
>

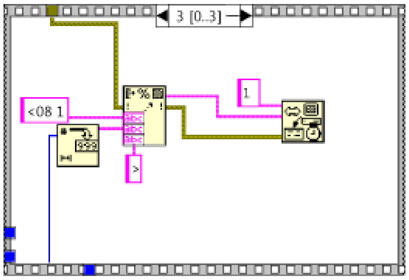
3 [0..3]
<08 1
1
>

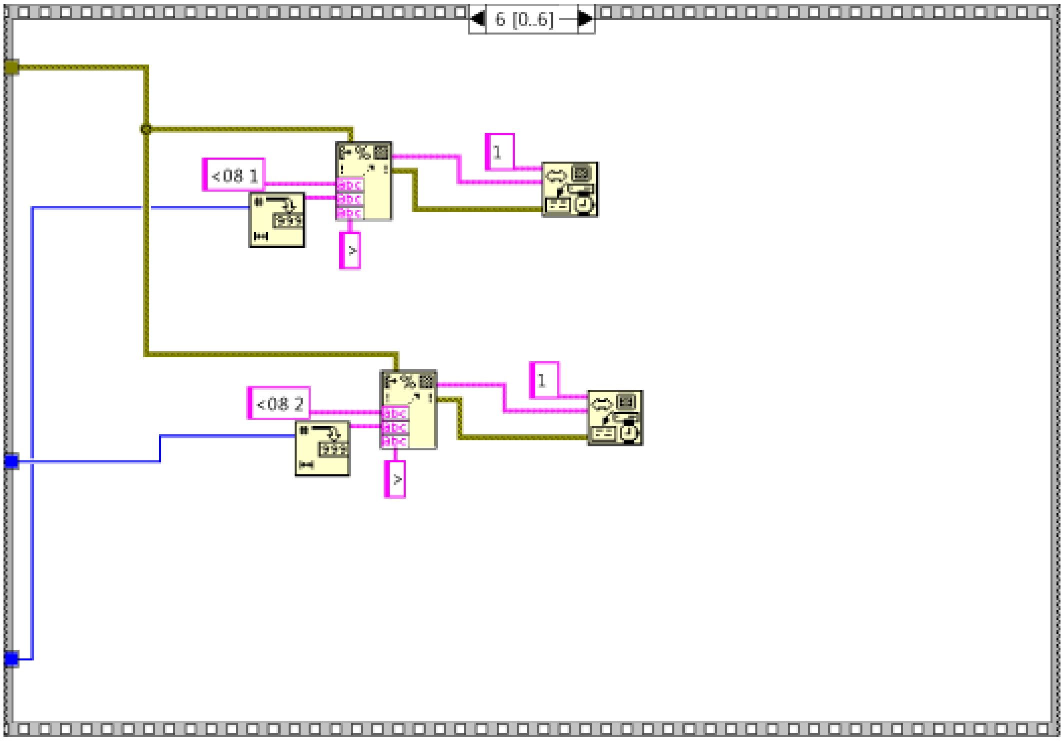
6 [0..6]
<08 1
1
>
<08 2
1
>

D. Movement of Inchworm (Active X)

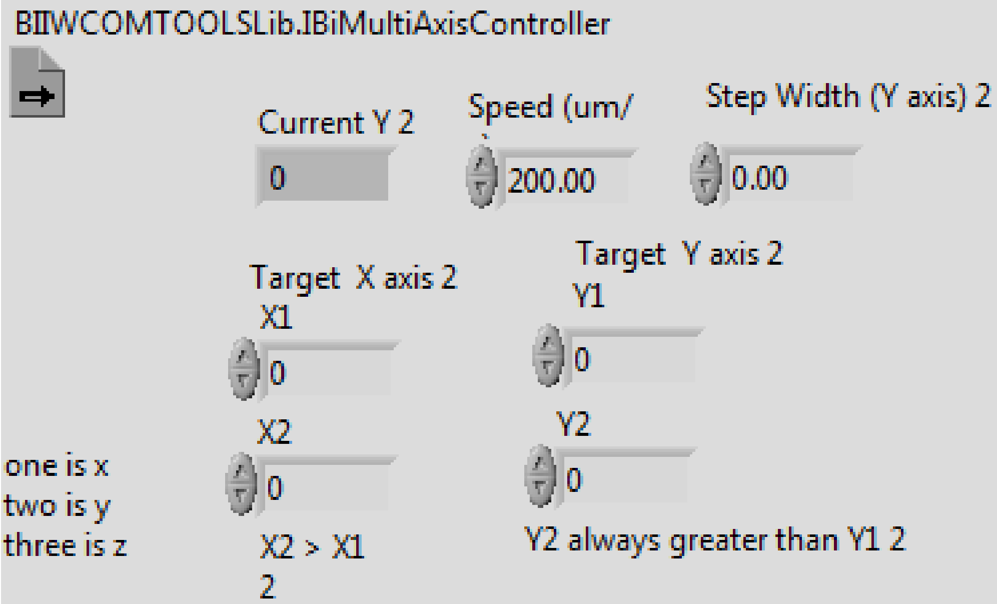

BIIWCOMTOOLSLib.IBiMultiAxisController

Current Y 2: 0

Speed (um/: 200.00

Step Width (Y axis) 2: 0.00

Target X axis 2

X1: 0

X2: 0

X2 > X1 2

Target Y axis 2

Y1: 0

Y2: 0

Y2 always greater than Y1 2

one is x
two is y
three is z

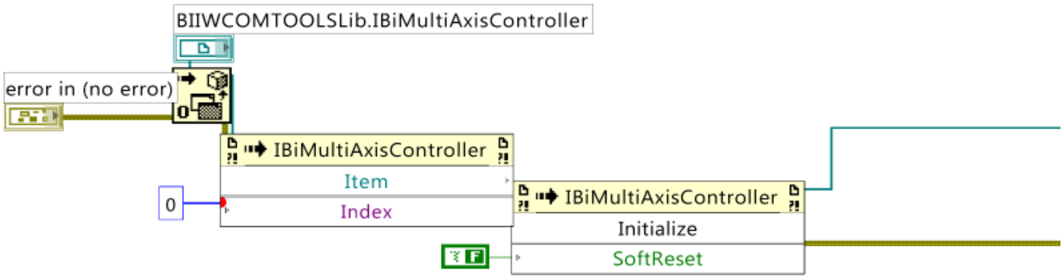
BIIWCOMTOOLSLib.IBiMultiAxisController
error in (no error)
IBiMultiAxisController
Item
Index
0
IBiMultiAxisController
Initialize
SoftReset

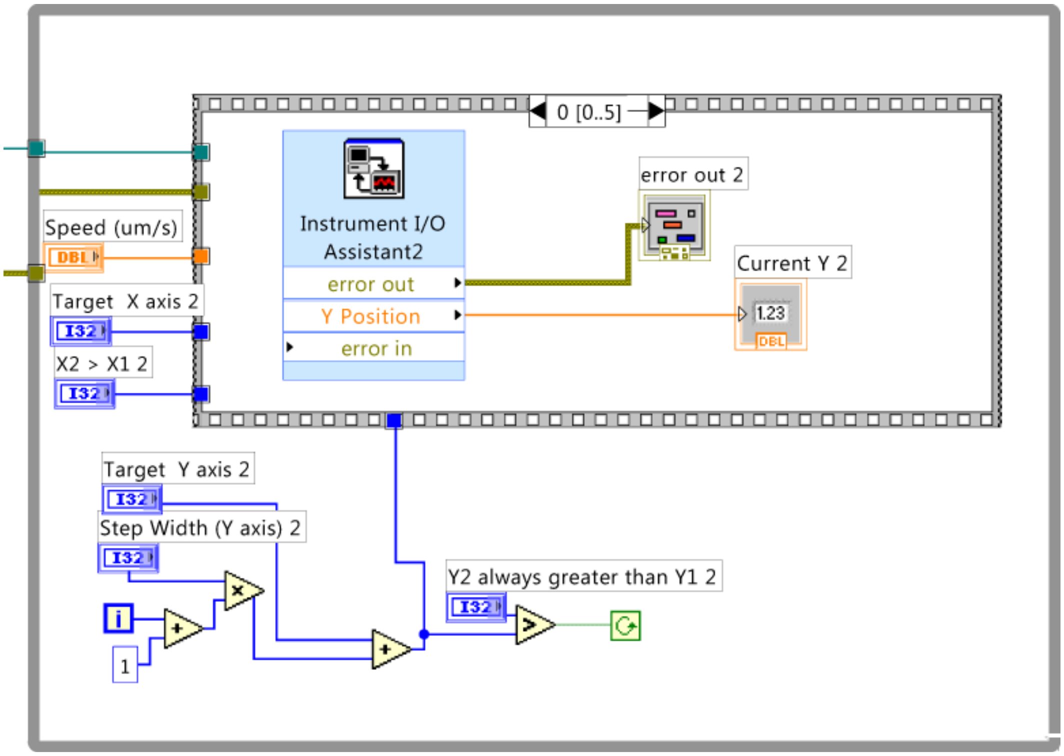
0 [0..5]
Instrument I/O Assistant2
error out
Y Position
error in
error out 2
Current Y 2
1.23
DBL
Speed (um/s)
DBL
Target X axis 2
I32
X2 > X1 2
I32
Target Y axis 2
I32
Step Width (Y axis) 2
I32
i
1
Y2 always greater than Y1 2
I32

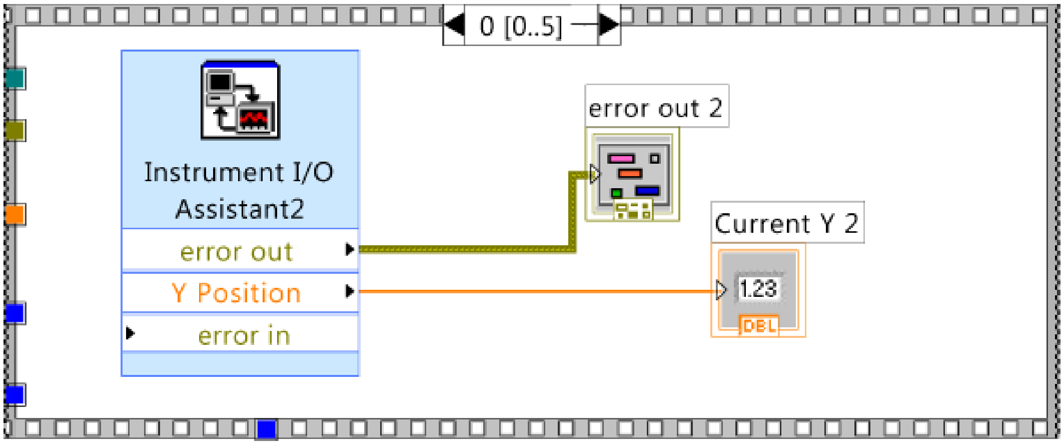
0 [0..5]
Instrument I/O Assistant2
error out
Y Position
error in
error out 2
Current Y 2
1.23
DBL

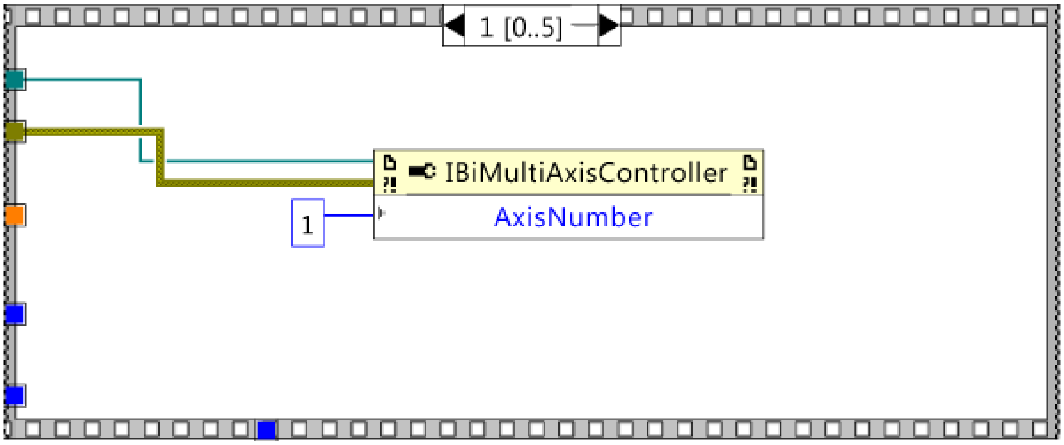
1 [0..5]
IBiMultiAxisController
AxisNumber
1

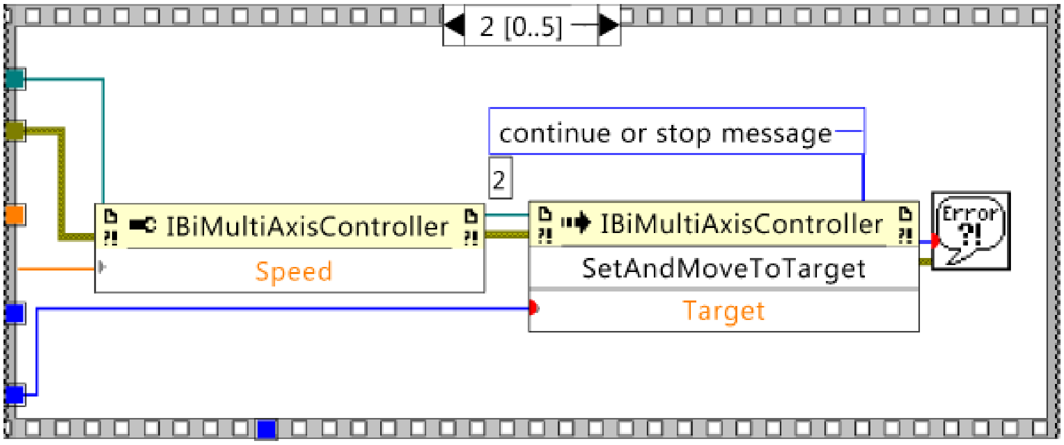
2 [0..5]
continue or stop message
2
IBiMultiAxisController
Speed
IBiMultiAxisController
SetAndMoveToTarget
Target
Error
?!

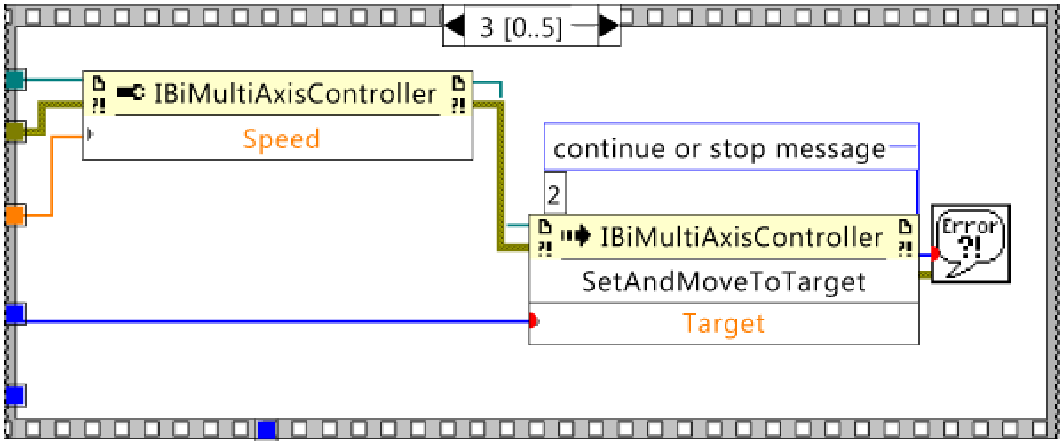
3 [0..5]
IBiMultiAxisController
Speed
continue or stop message
2
IBiMultiAxisController
SetAndMoveToTarget
Target
Error
?!

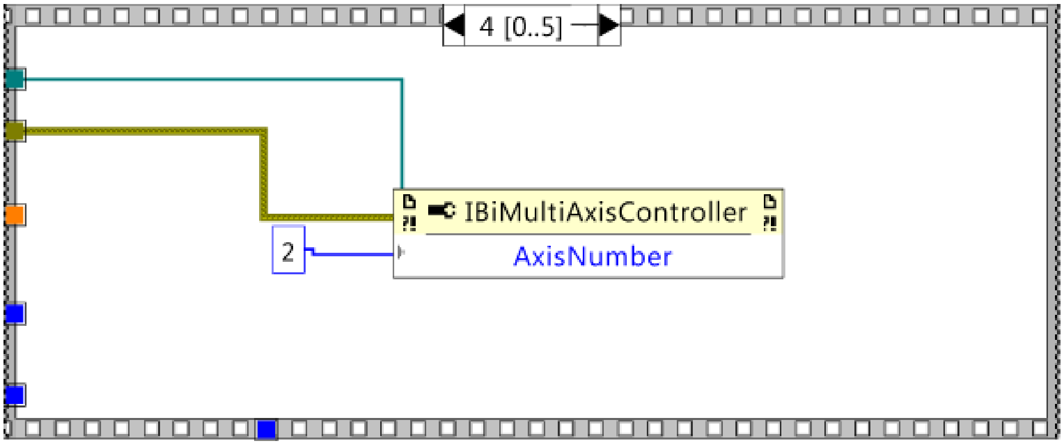
4 [0..5]
IBiMultiAxisController
AxisNumber
2

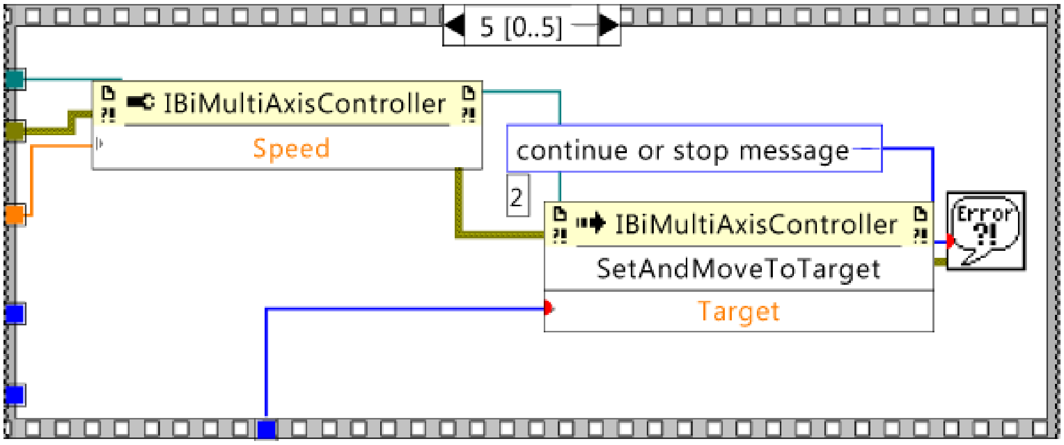
5 [0..5]
IBiMultiAxisController
Speed
continue or stop message
2
IBiMultiAxisController
SetAndMoveToTarget
Target
Error
?!

E. Cyclic Voltametry

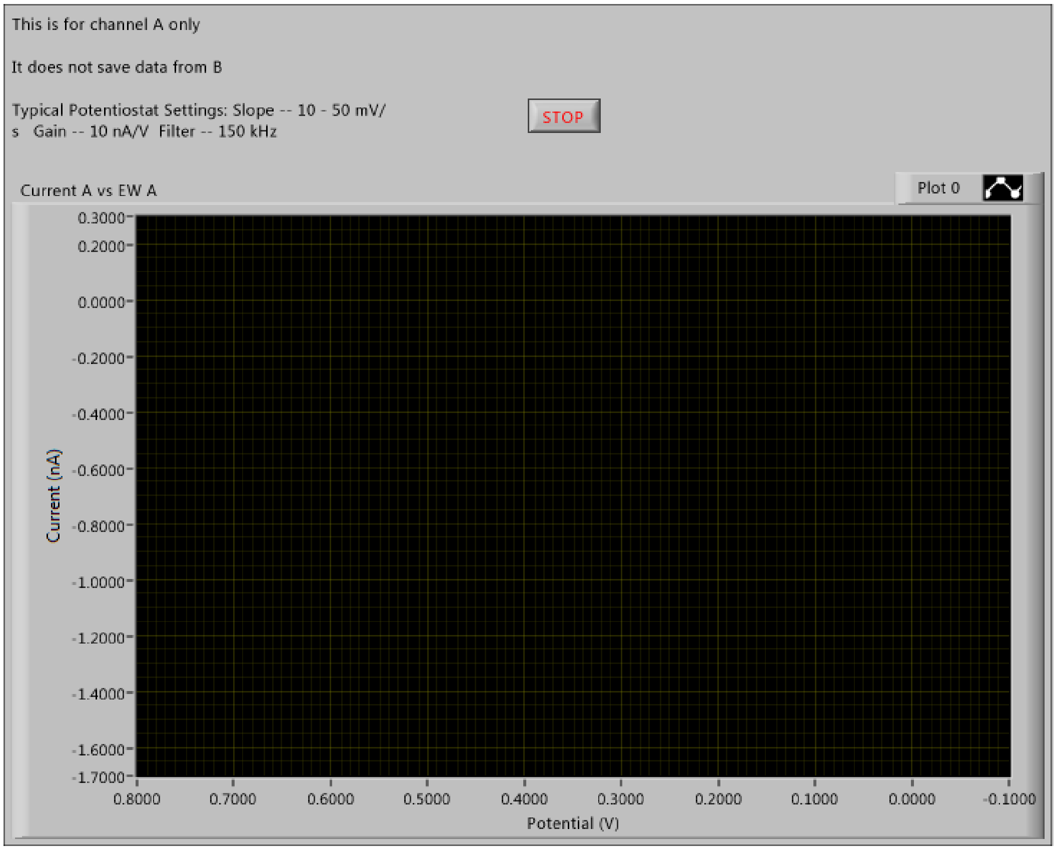

This is for channel A only

It does not save data from B

Typical Potentiostat Settings: Slope -- 10 - 50 mV/s Gain -- 10 nA/V Filter -- 150 kHz

STOP
Current A vs EW A
Plot 0
0.3000
0.2000
0.0000
-0.2000
-0.4000
-0.6000
-0.8000
-1.0000
-1.2000
-1.4000
-1.6000
-1.7000
Current (nA)
0.8000
0.7000
0.6000
0.5000
0.4000
0.3000
0.2000
0.1000
0.0000
-0.1000
Potential (V)

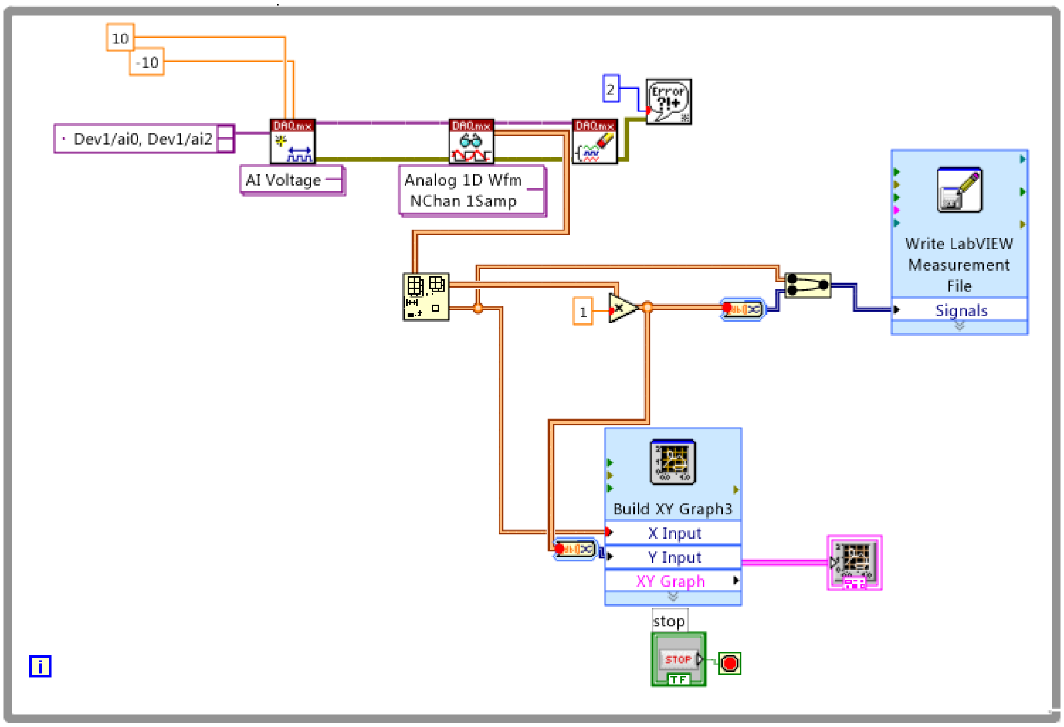
10
-10
Dev1/ai0, Dev1/ai2
AI Voltage
Analog 1D Wfm NChan 1Samp
2
1
Write LabVIEW Measurement File
Signals
Build XY Graph3
X Input
Y Input
XY Graph
stop
STOP
TF

CV Program Flowchart

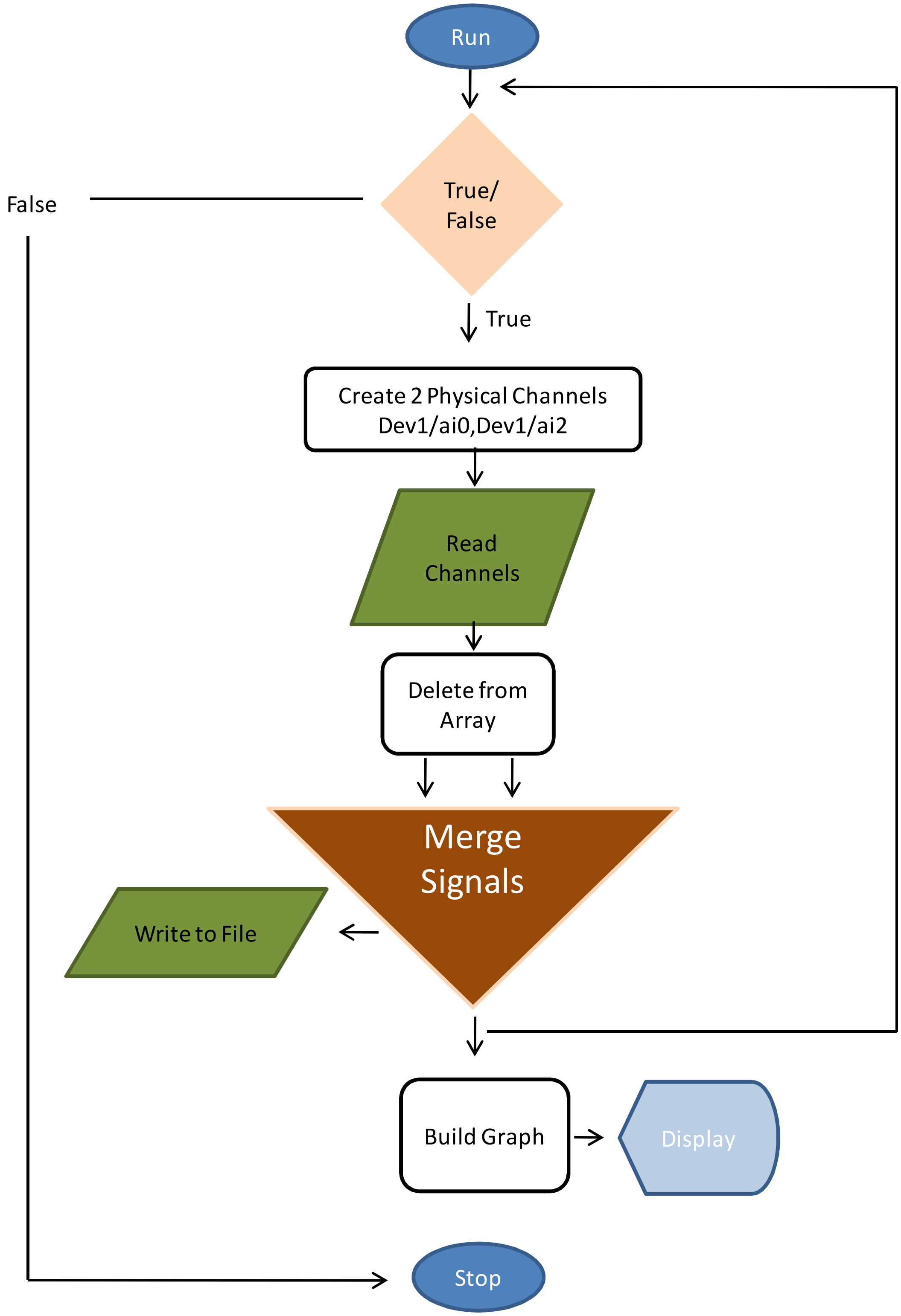
Run
True/
False
False
True
Create 2 Physical Channels
Dev1/ai0,Dev1/ai2
Read
Channels
Delete from
Array
Merge
Signals
Write to File
Build Graph
Display
Stop

F. Approach

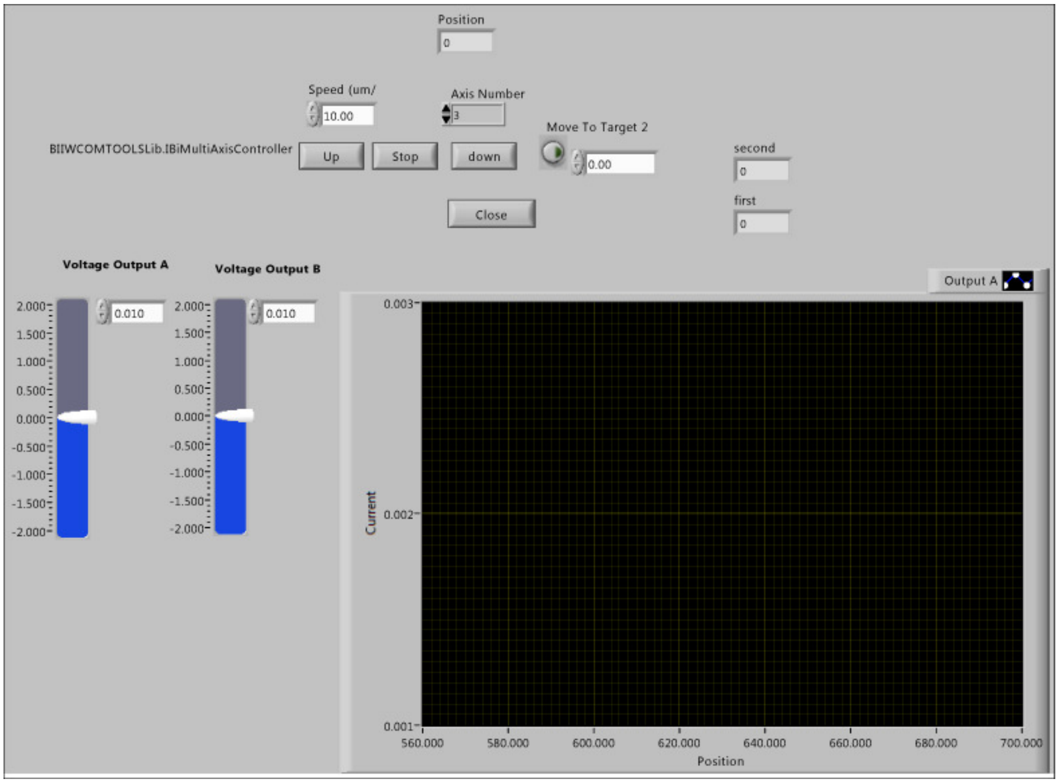

Position: 0

Speed (um/: 10.00

Axis Number: 3

Move To Target 2: 0.00

second: 0

first: 0

Voltage Output A: 0.010

Voltage Output B: 0.010

BIIWCOMTOOLSLib.IBiMultiAxisController
Up
Stop
down
Close
2.000
1.500
1.000
0.500
0.000
-0.500
-1.000
-1.500
-2.000
Output A
0.003
0.002
0.001
Current
560.000
580.000
600.000
620.000
640.000
660.000
680.000
700.000
Position

AC Program Flowchart

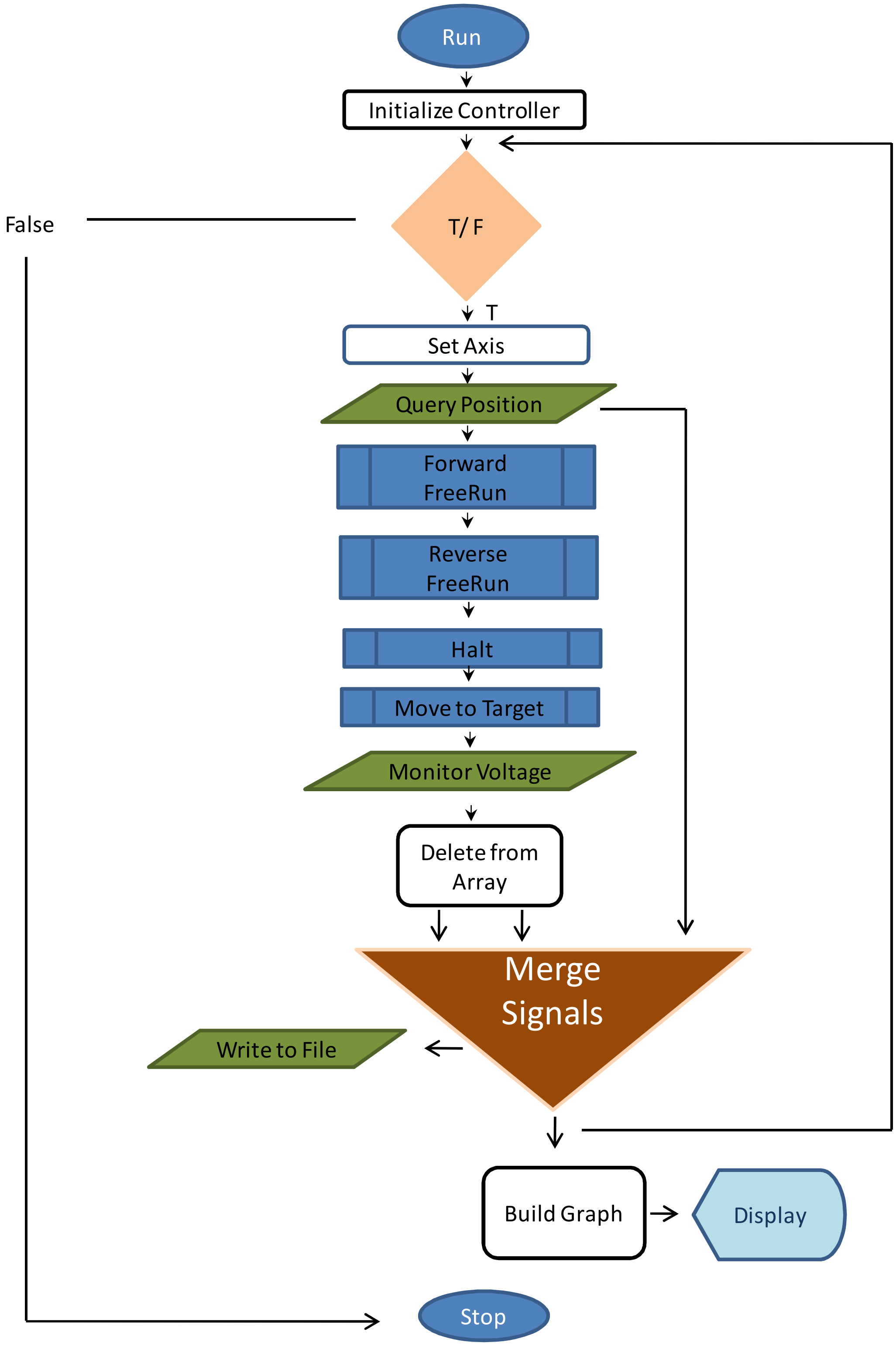
Run
Initialize Controller
False
T/ F
T
Set Axis
Query Position
Forward FreeRun
Reverse FreeRun
Halt
Move to Target
Monitor Voltage
Delete from Array
Merge Signals
Write to File
Build Graph
Display
Stop

Forward Free Run

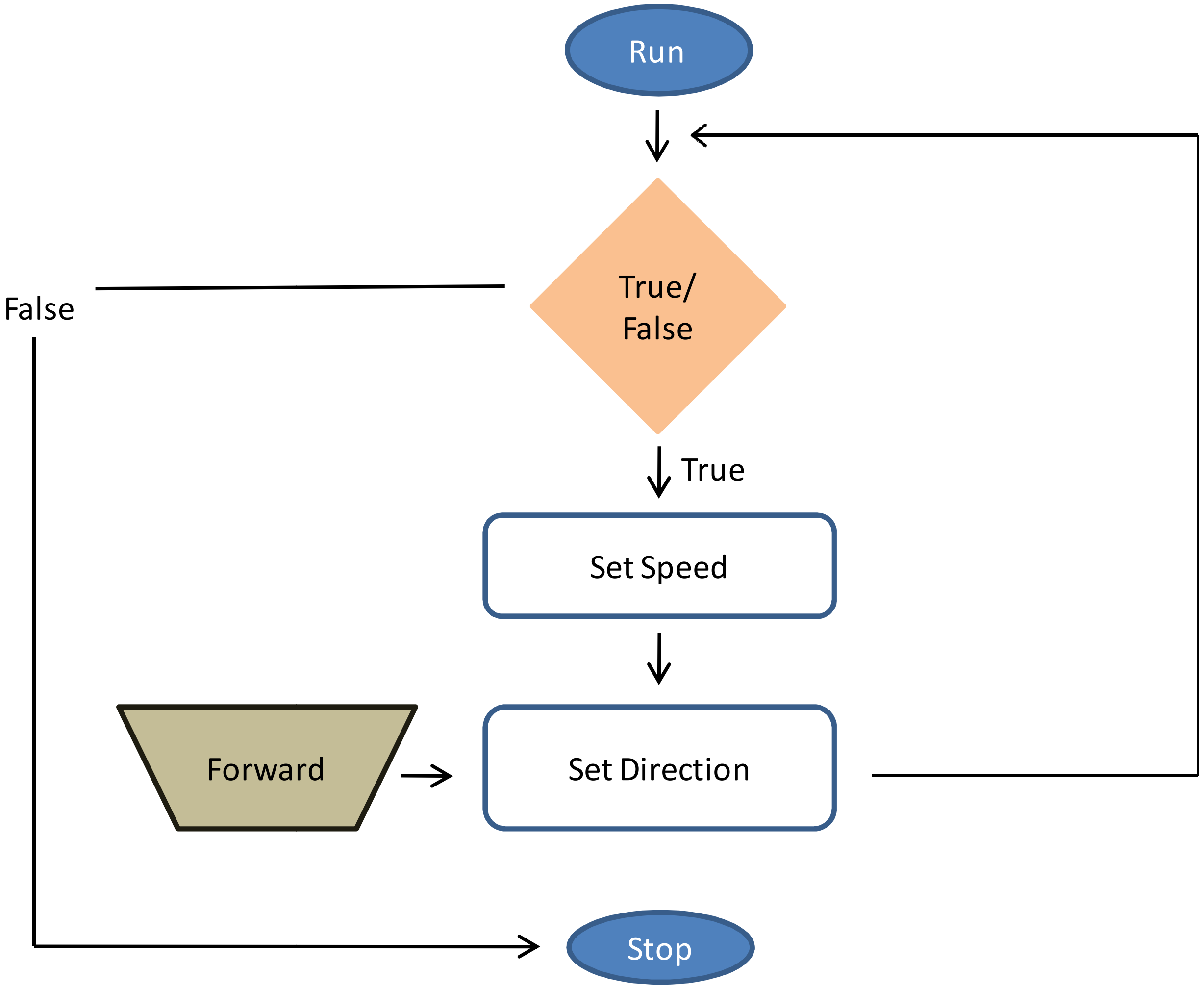
Run
True/
False
False
True
Set Speed
Forward
Set Direction
Stop

Reverse Free Run

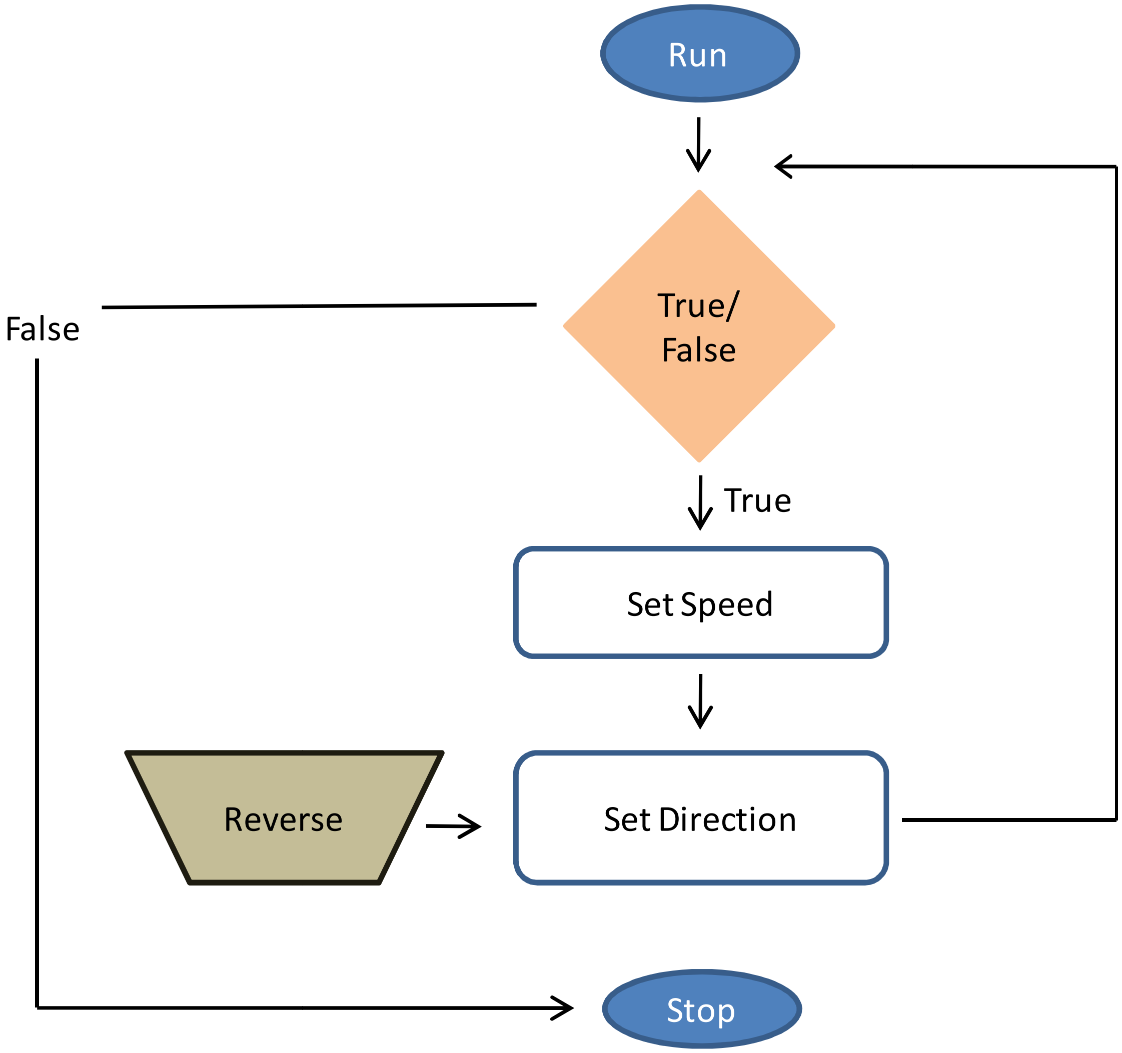
Run
True/
False
False
True
Set Speed
Reverse
Set Direction
Stop

Halt

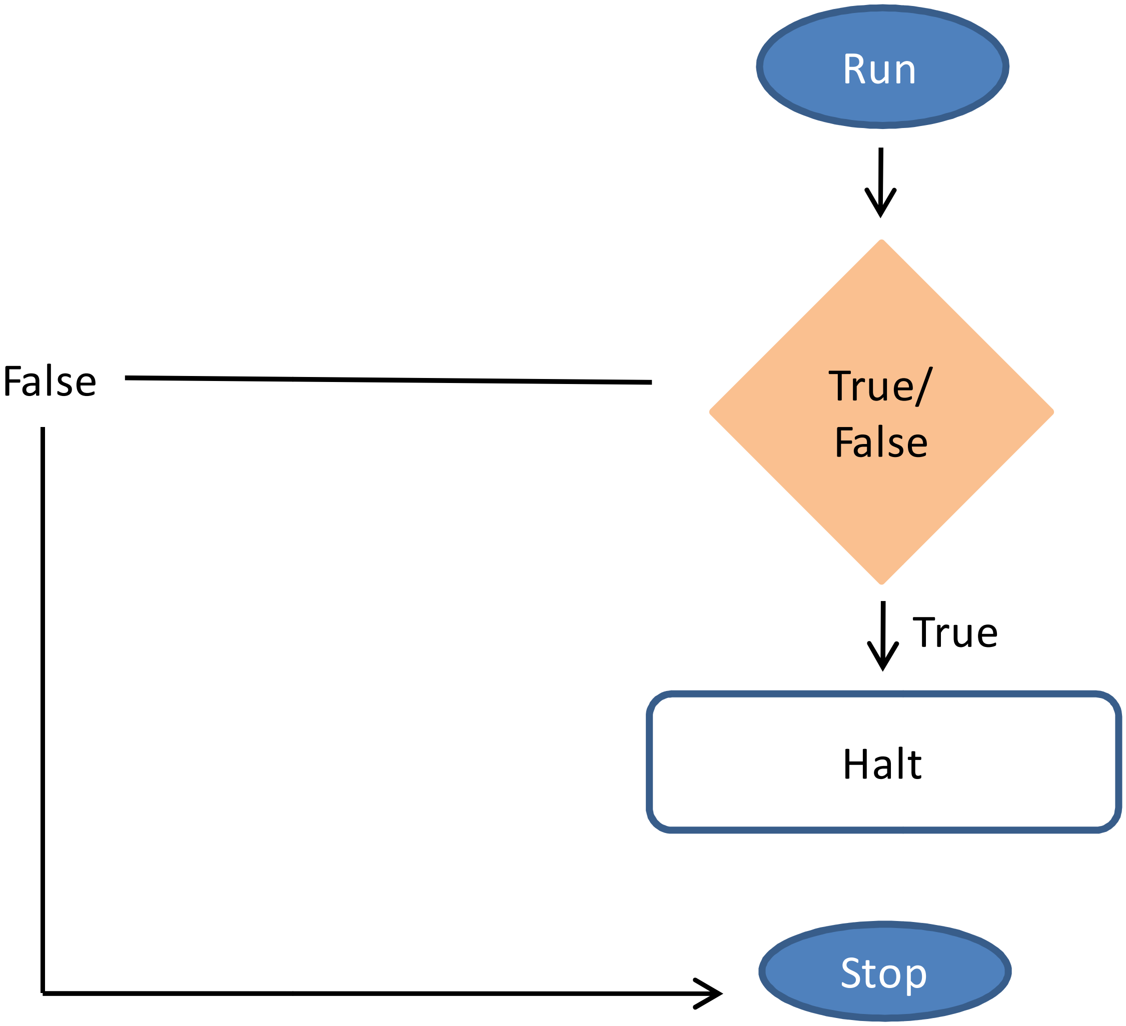
Run
True/
False
False
True
Halt
Stop

Move to Target

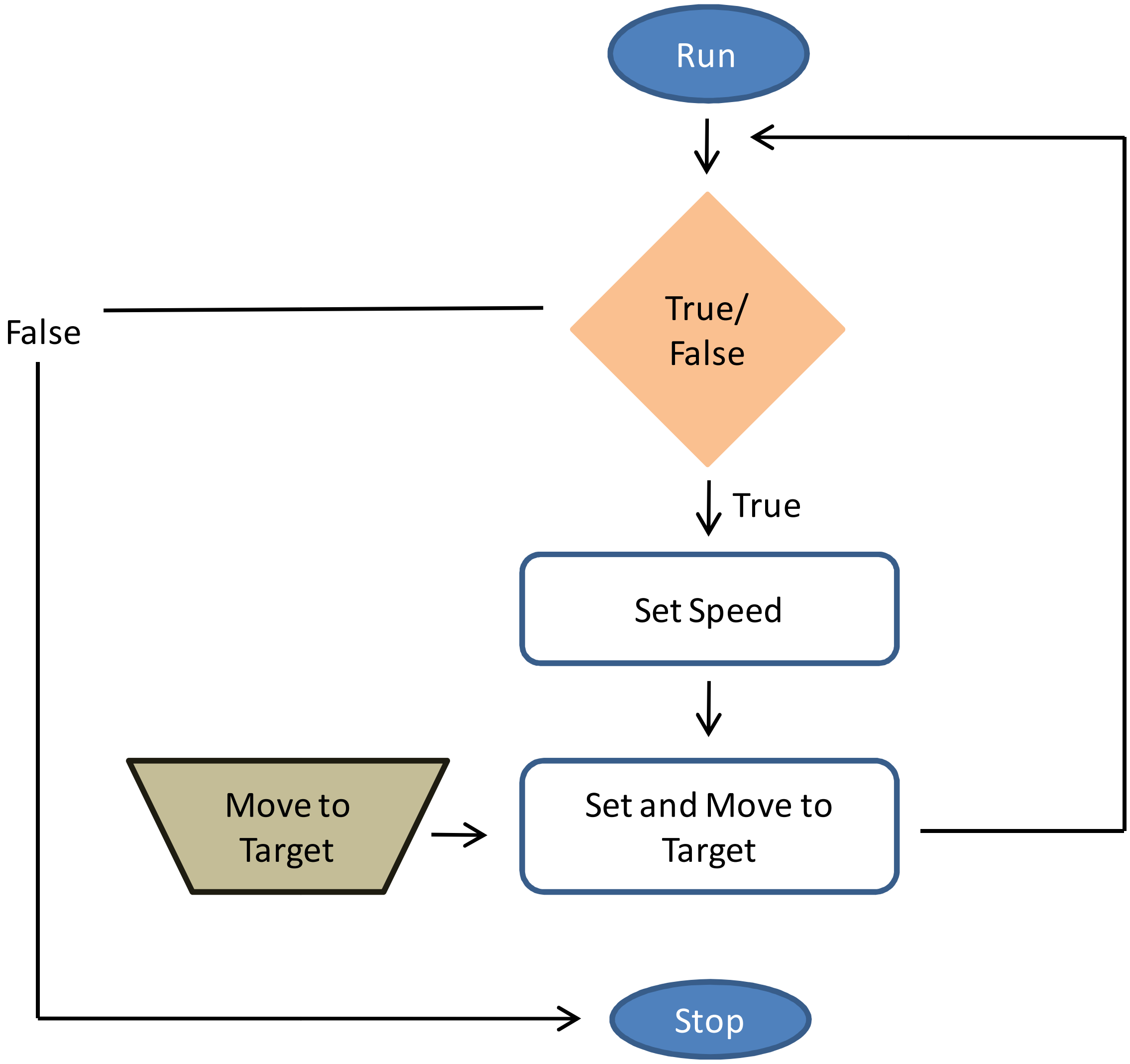
Run
True/
False
False
True
Set Speed
Move to
Target
Set and Move to
Target
Stop

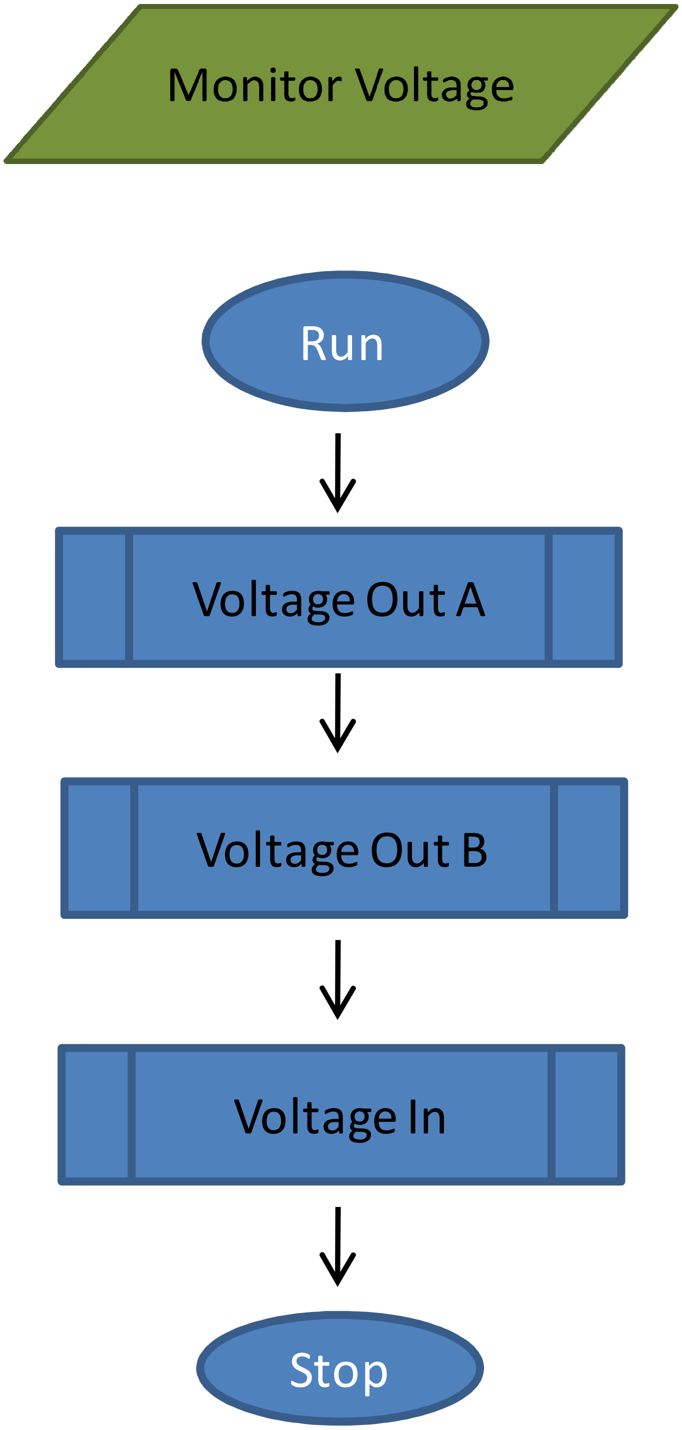
Monitor Voltage
Run
Voltage Out A
Voltage Out B
Voltage In
Stop

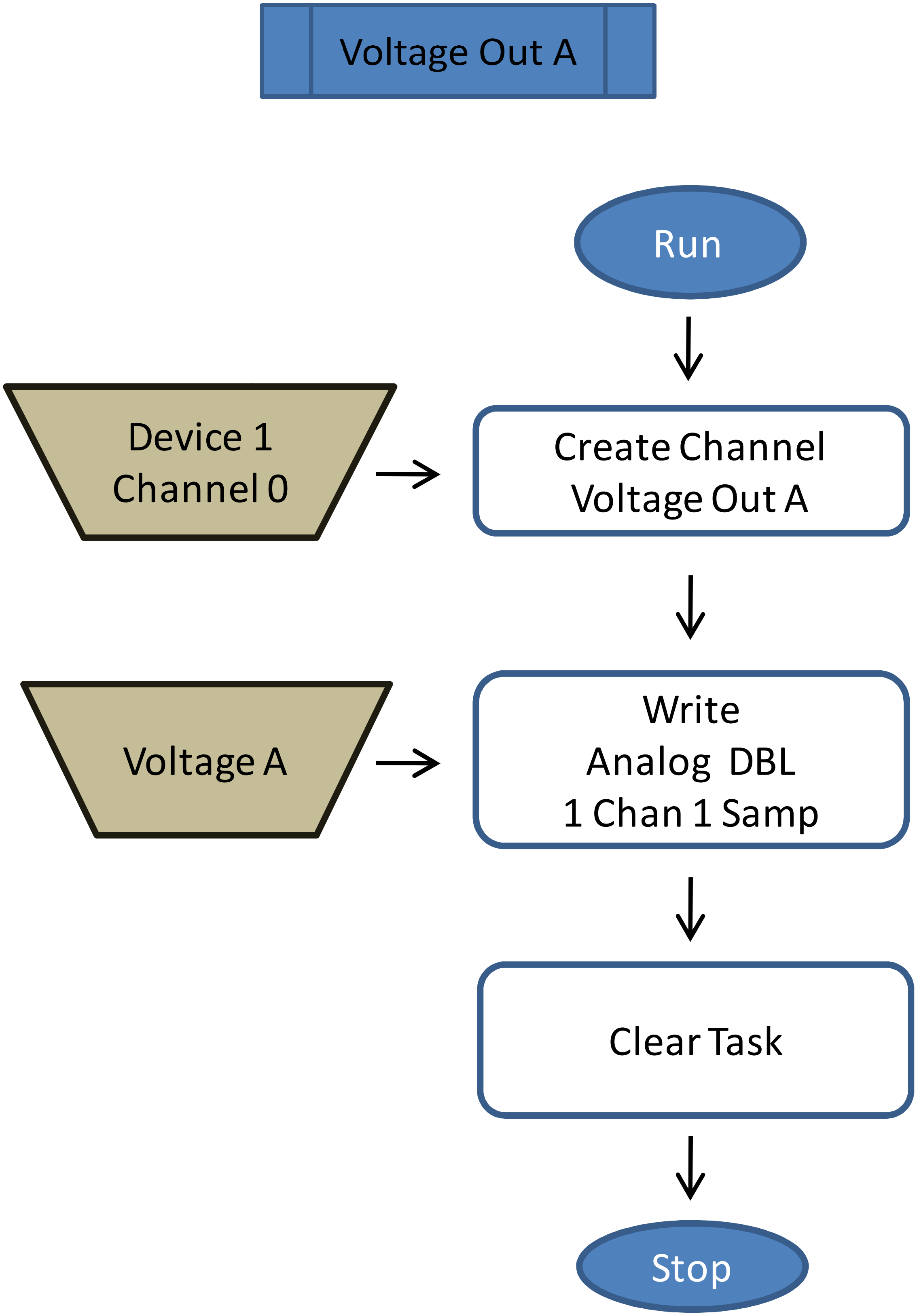
Voltage Out A
Run
Device 1
Channel 0
Create Channel
Voltage Out A
Voltage A
Write
Analog DBL
1 Chan 1 Samp
Clear Task
Stop

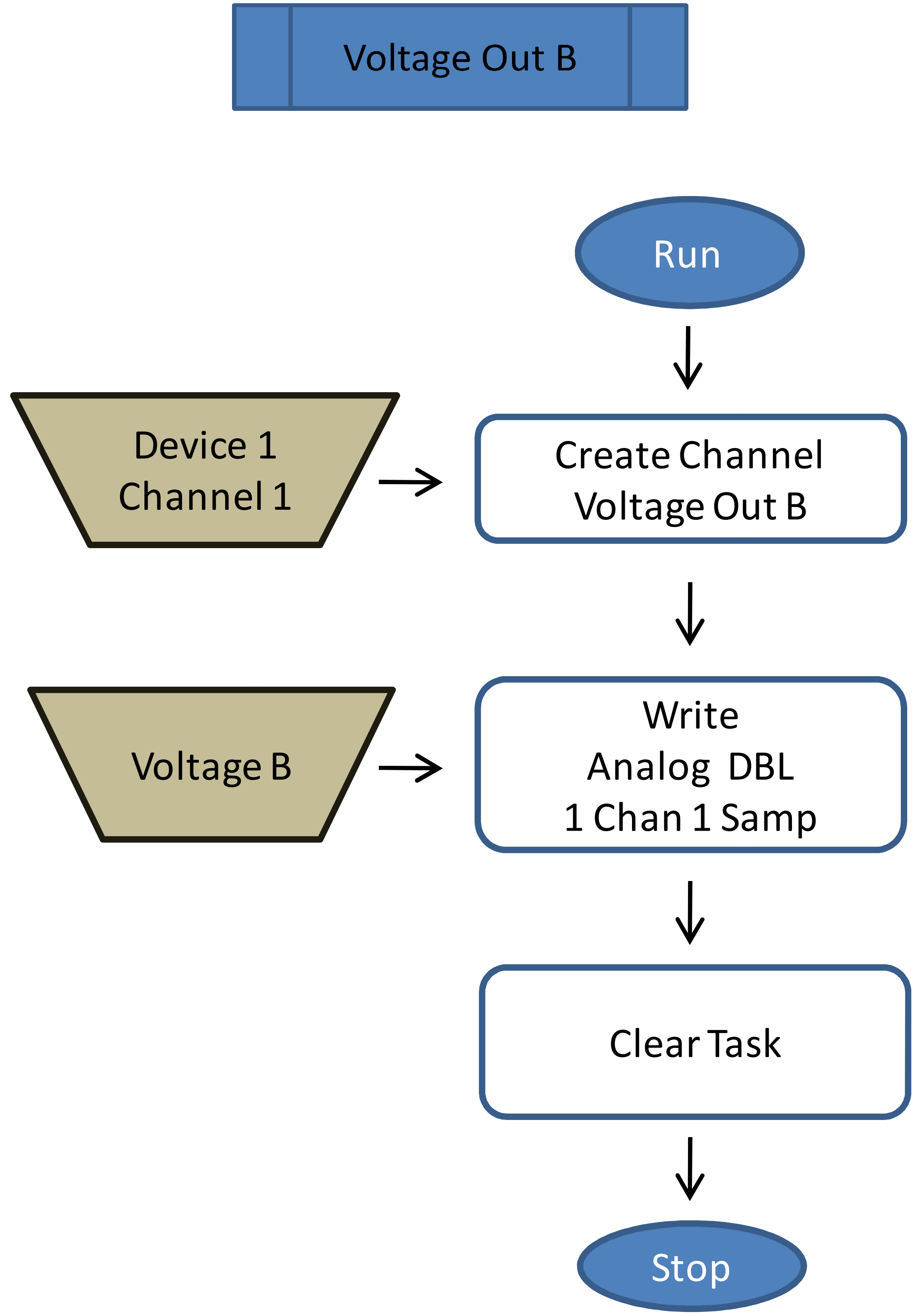
Voltage Out B
Run
Device 1
Channel 1
Create Channel
Voltage Out B
Voltage B
Write
Analog DBL
1 Chan 1 Samp
Clear Task
Stop

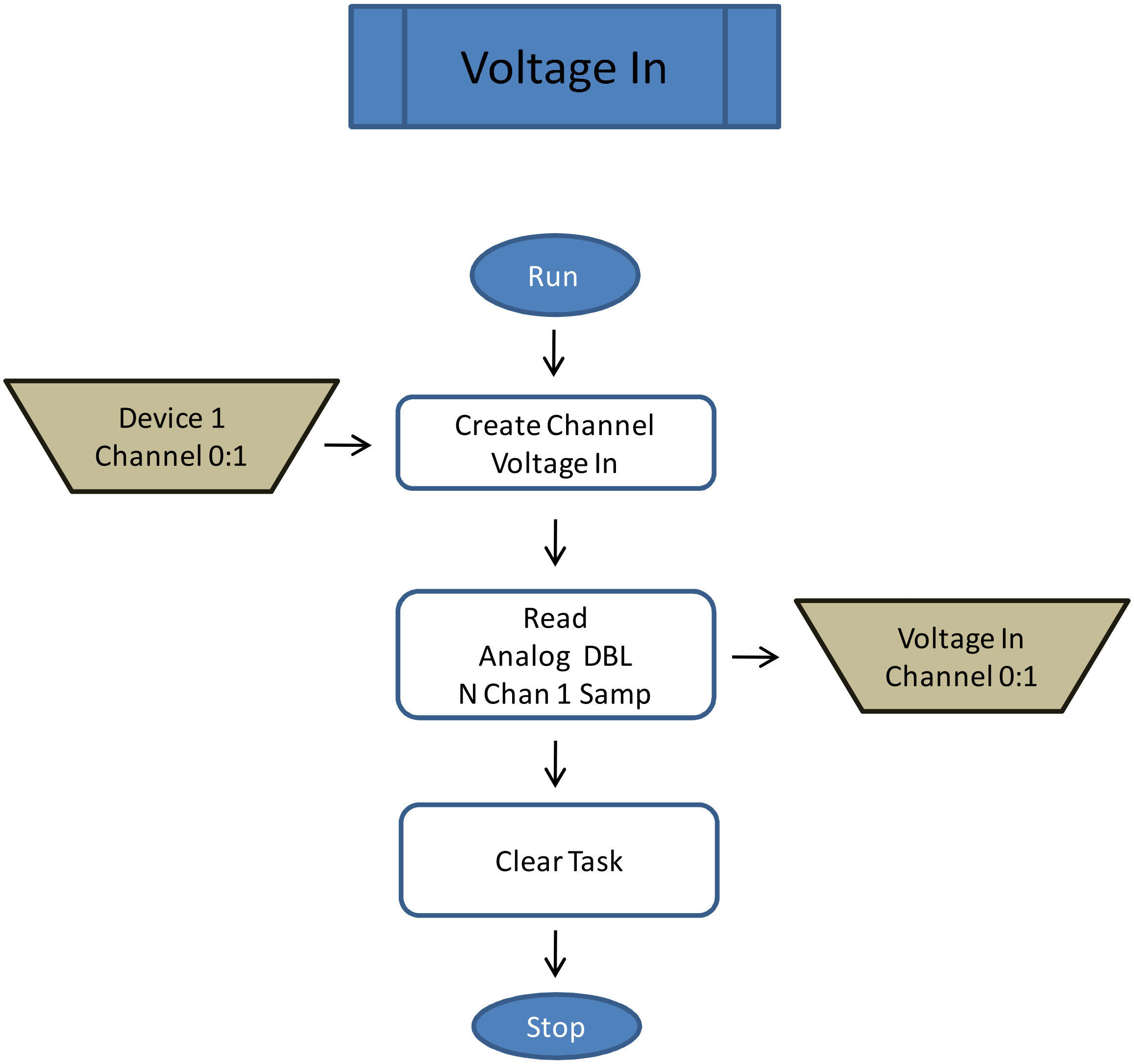
Voltage In
Run
Device 1
Channel 0:1
Create Channel
Voltage In
Read
Analog DBL
N Chan 1 Samp
Voltage In
Channel 0:1
Clear Task
Stop

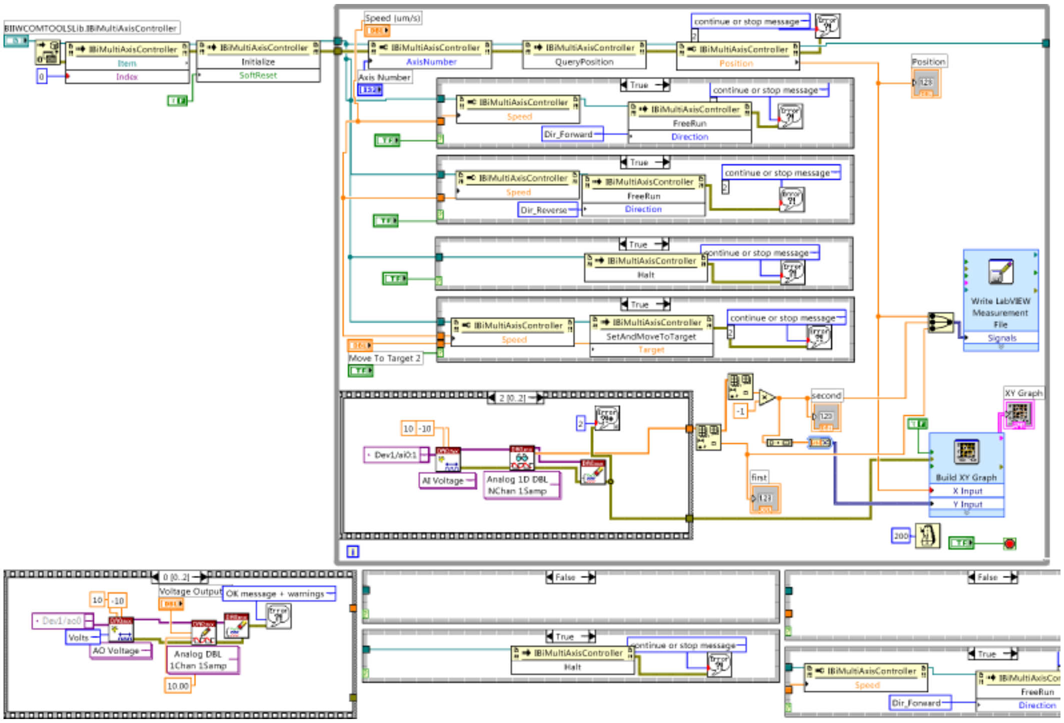

BIIWCOMTOOLSLib.IBiMultiAxisController
IBiMultiAxisController
Item
Index
IBiMultiAxisController
Initialize
SoftReset
Speed (um/s)
Axis Number
IBiMultiAxisController
AxisNumber
IBiMultiAxisController
QueryPosition
continue or stop message
IBiMultiAxisController
Position
Position
True
IBiMultiAxisController
Speed
Dir_Forward
IBiMultiAxisController
FreeRun
Direction
True
IBiMultiAxisController
Speed
Dir_Reverse
IBiMultiAxisController
FreeRun
Direction
True
IBiMultiAxisController
Halt
True
IBiMultiAxisController
Speed
IBiMultiAxisController
SetAndMoveToTarget
Target
Move To Target 2
Write LabVIEW Measurement File
Signals
2 [0..2]
10
-10
Dev1/ai0:1
AI Voltage
Analog 1D DBL NChan 1Samp
second
first
-1
XY Graph
Build XY Graph
X Input
Y Input
200
0 [0..2]
Voltage Output
OK message + warnings
Dev1/ao0
Volts
AO Voltage
Analog DBL 1Chan 1Samp
10.00
False
True
IBiMultiAxisController
Halt
continue or stop message
False
True
IBiMultiAxisController
Speed
Dir_Forward
IBiMultiAxisController
FreeRun
Direction

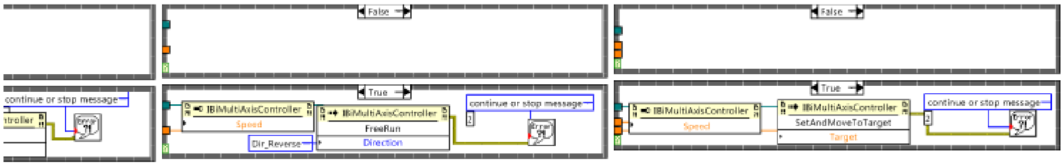

False
False
continue or stop message
True
IBiMultiAxisController
Speed
Dir_Reverse
IBiMultiAxisController
FreeRun
Direction
continue or stop message
True
IBiMultiAxisController
Speed
IBiMultiAxisController
SetAndMoveToTarget
Target
continue or stop message

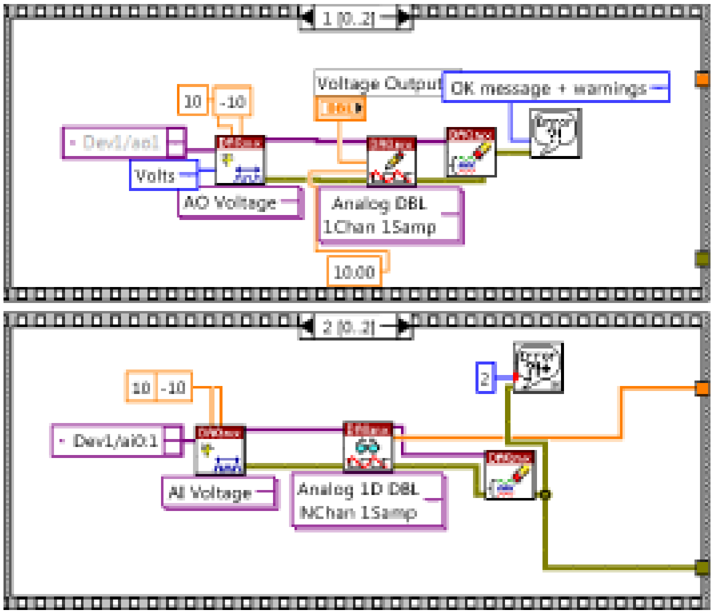

1 [0..2]
10
-10
Voltage Output
OK message + warnings
Dev1/ao1
Volts
AO Voltage
Analog DBL 1Chan 1Samp
10.00
2 [0..2]
2
10
-10
Dev1/ai0:1
AI Voltage
Analog 1D DBL NChan 1Samp

G. Image

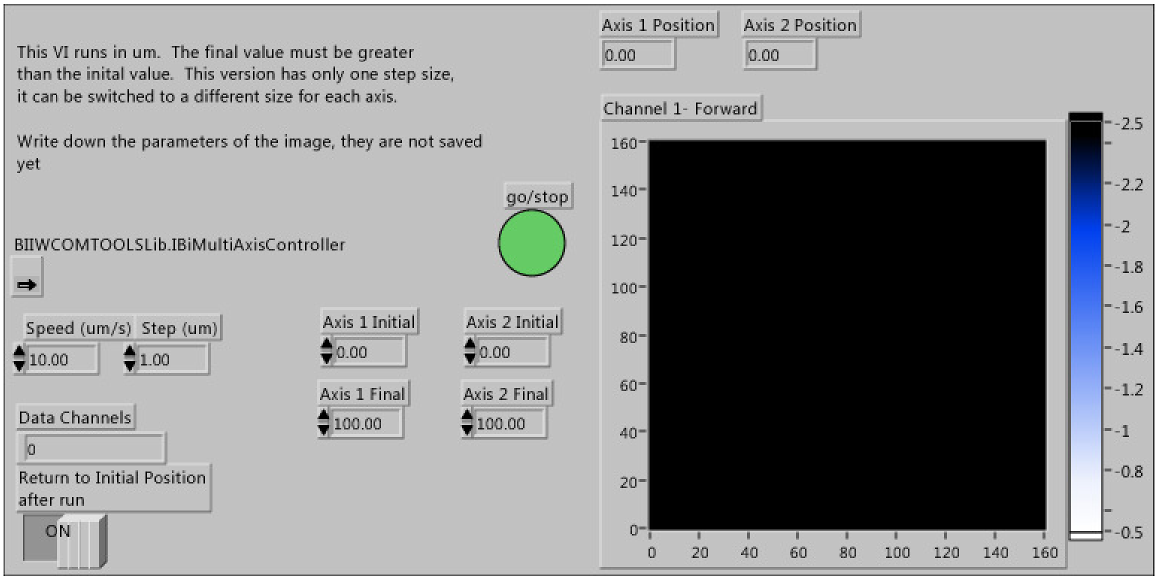

This VI runs in um. The final value must be greater than the inital value. This version has only one step size, it can be switched to a different size for each axis.

Write down the parameters of the image, they are not saved yet

BIIWCOMTOOLSLib.IBiMultiAxisController

Axis 1 Position: 0.00
Axis 2 Position: 0.00
Speed (um/s): 10.00
Step (um): 1.00
Axis 1 Initial: 0.00
Axis 2 Initial: 0.00
Axis 1 Final: 100.00
Axis 2 Final: 100.00
Data Channels: 0
Return to Initial Position after run: ON

go/stop
Channel 1- Forward
160
140
120
100
80
60
40
20
0
0
20
40
60
80
100
120
140
160
-2.5
-2.2
-2
-1.8
-1.6
-1.4
-1.2
-1
-0.8
-0.5

Imaging Program

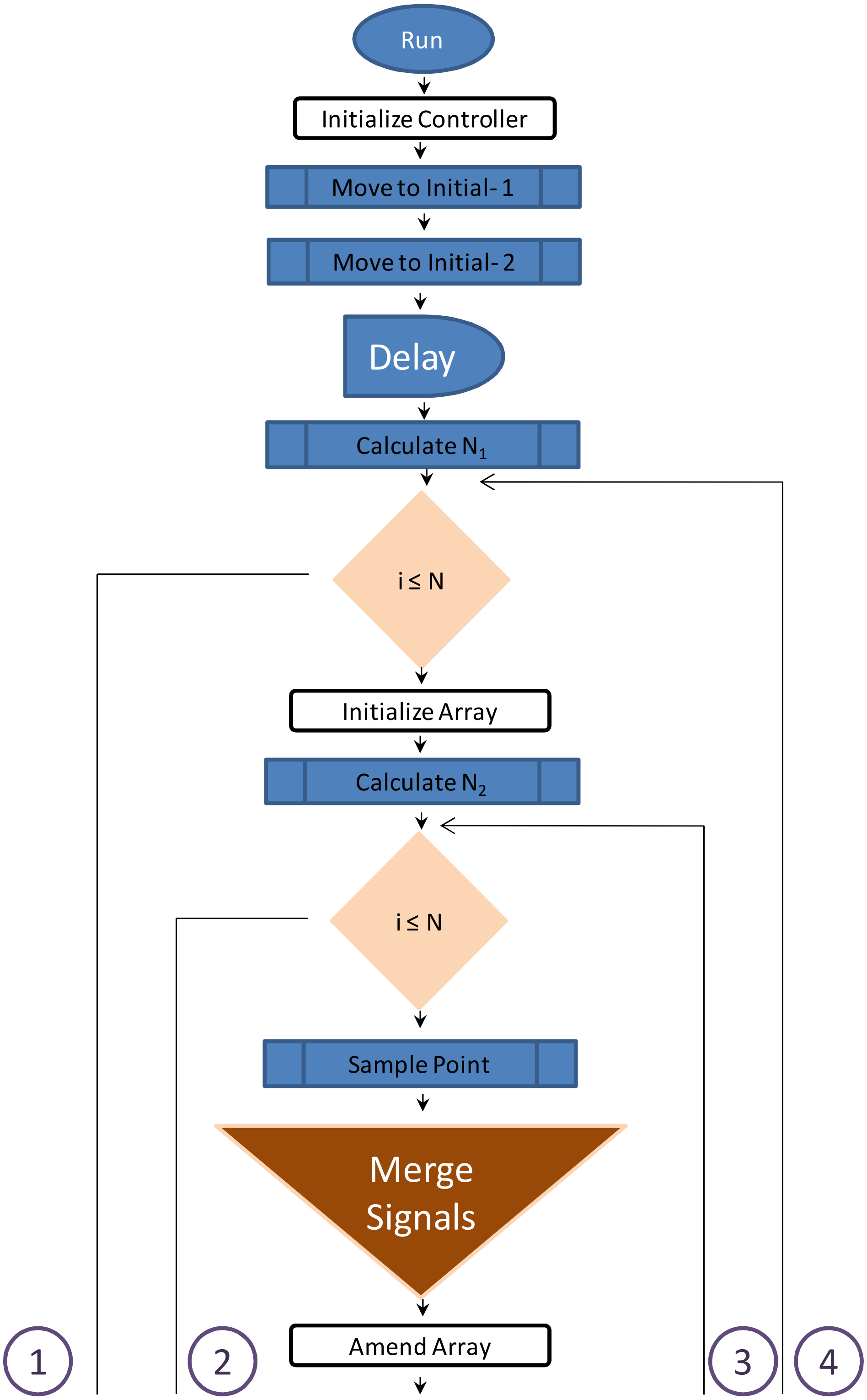
Run
Initialize Controller
Move to Initial - 1
Move to Initial - 2
Delay
Calculate N_1
i ≤ N
Initialize Array
Calculate N_2
i ≤ N
Sample Point
Merge Signals
Amend Array
1
2
3
4

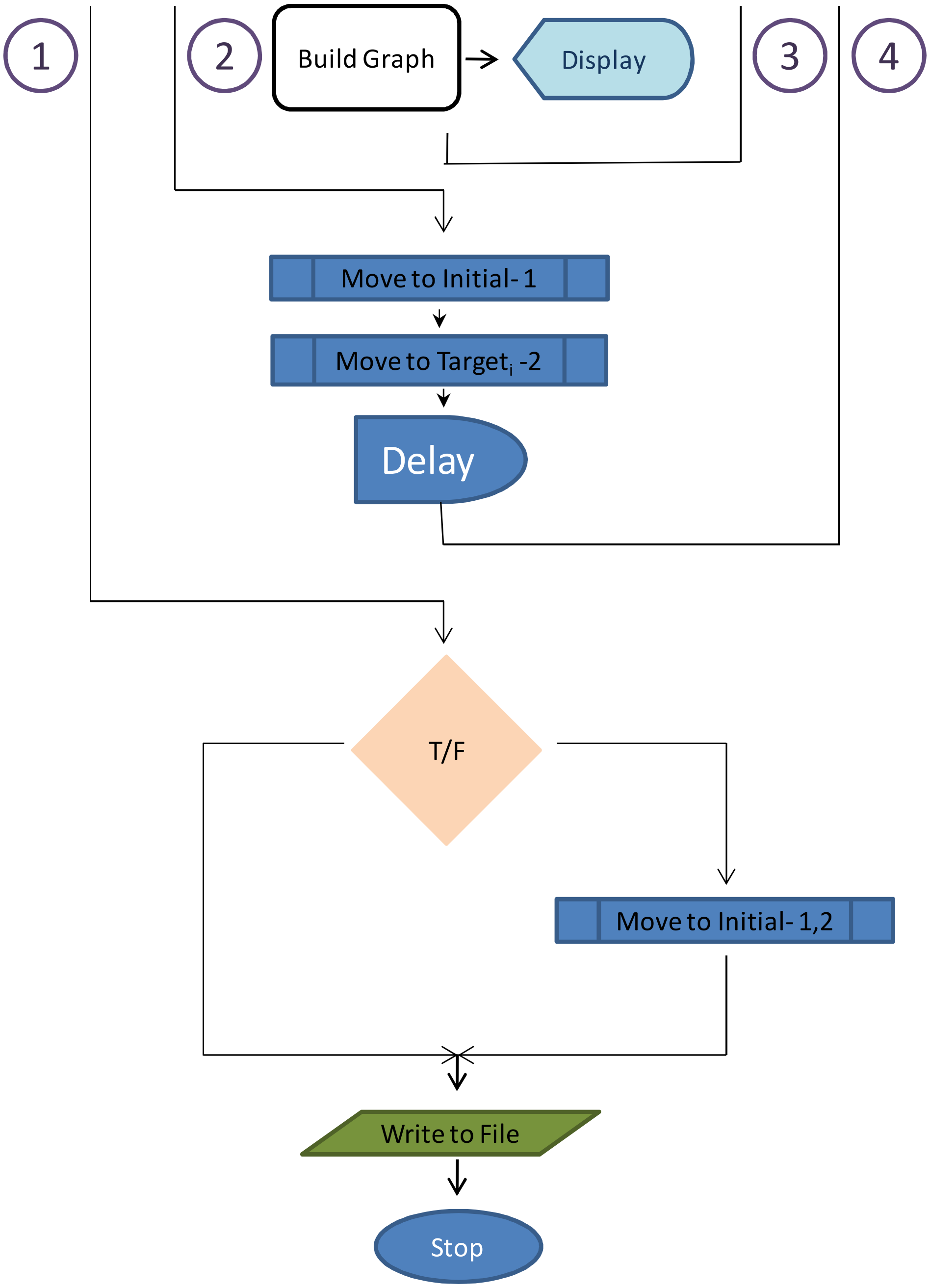
1
2
Build Graph
Display
3
4
Move to Initial- 1
Move to Target$_i$ -2
Delay
T/F
Move to Initial- 1,2
Write to File
Stop

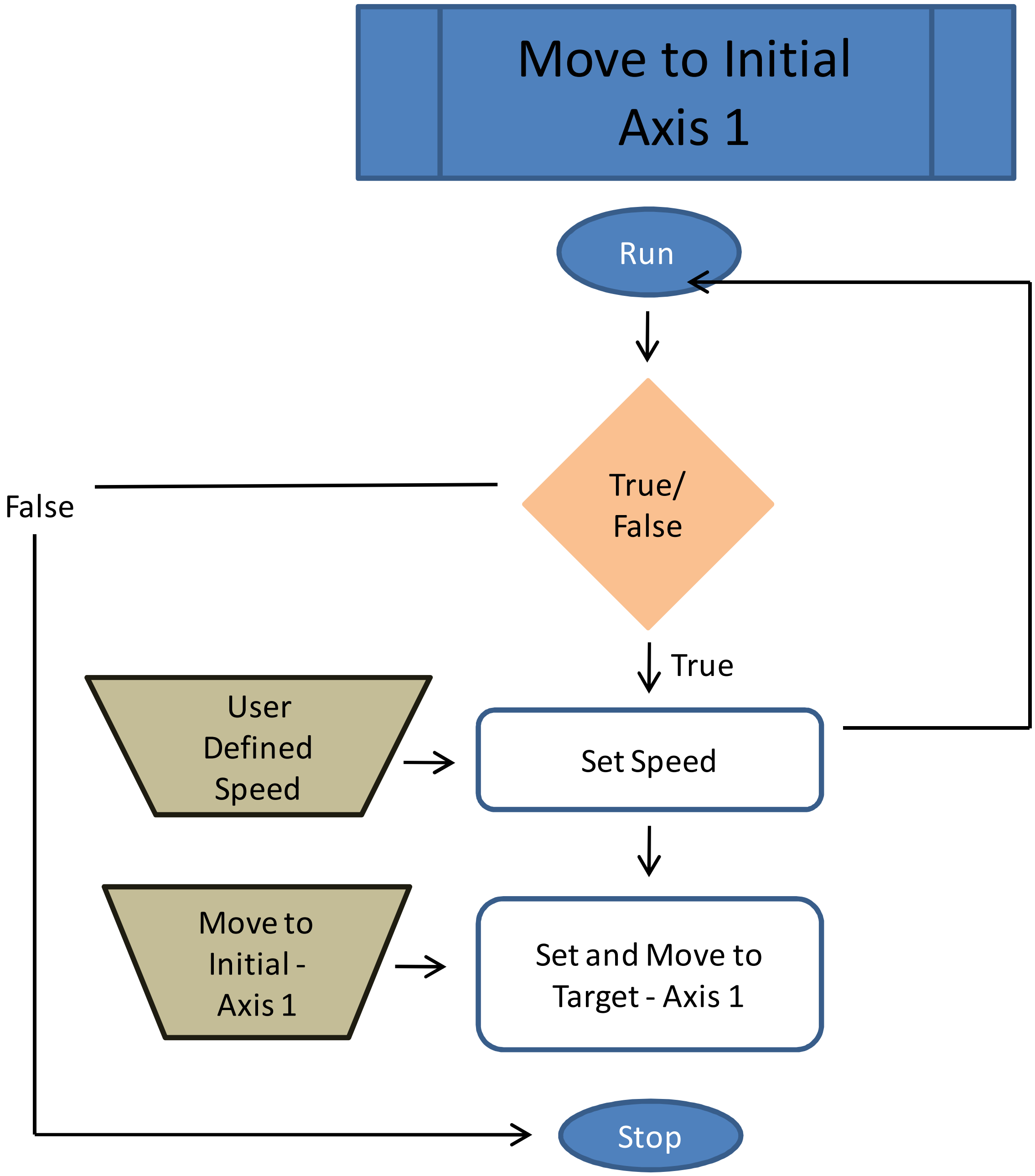
Move to Initial Axis 1
Run
False
True/ False
True
User Defined Speed
Set Speed
Move to Initial - Axis 1
Set and Move to Target - Axis 1
Stop

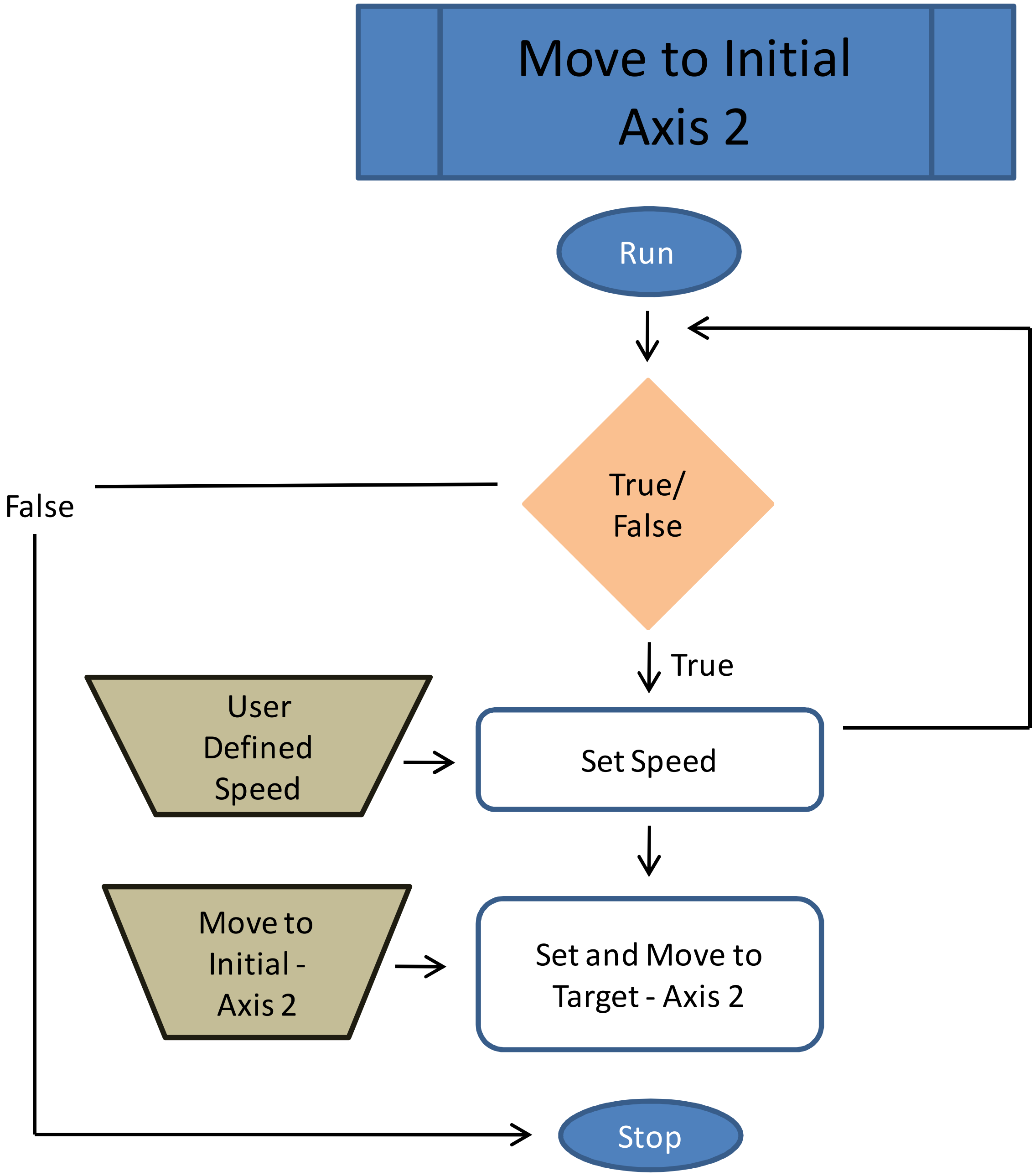
Move to Initial Axis 2
Run
True/ False
False
True
User Defined Speed
Set Speed
Move to Initial - Axis 2
Set and Move to Target - Axis 2
Stop

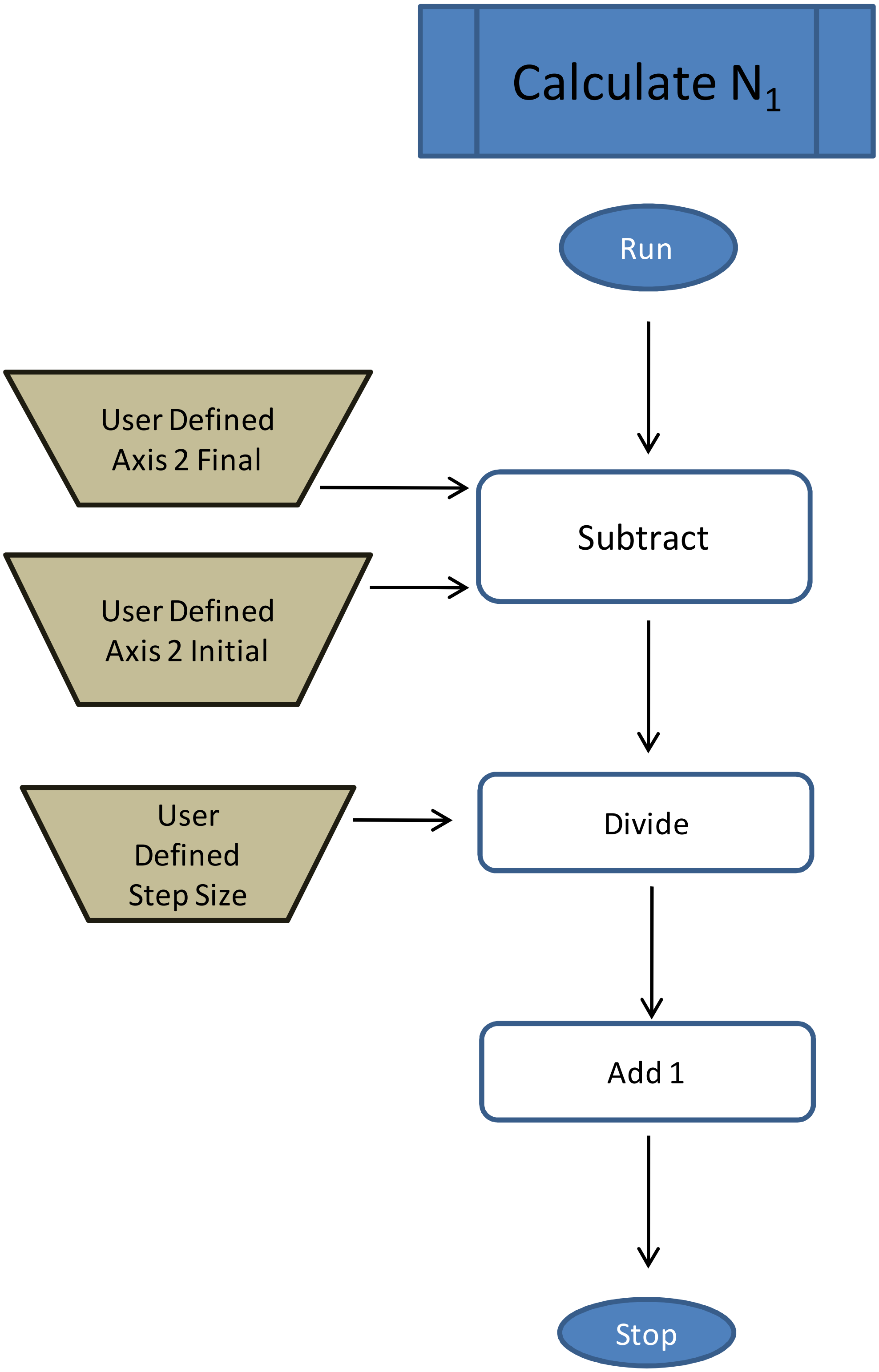
Calculate N_1
Run
User Defined Axis 2 Final
User Defined Axis 2 Initial
Subtract
User Defined Step Size
Divide
Add 1
Stop

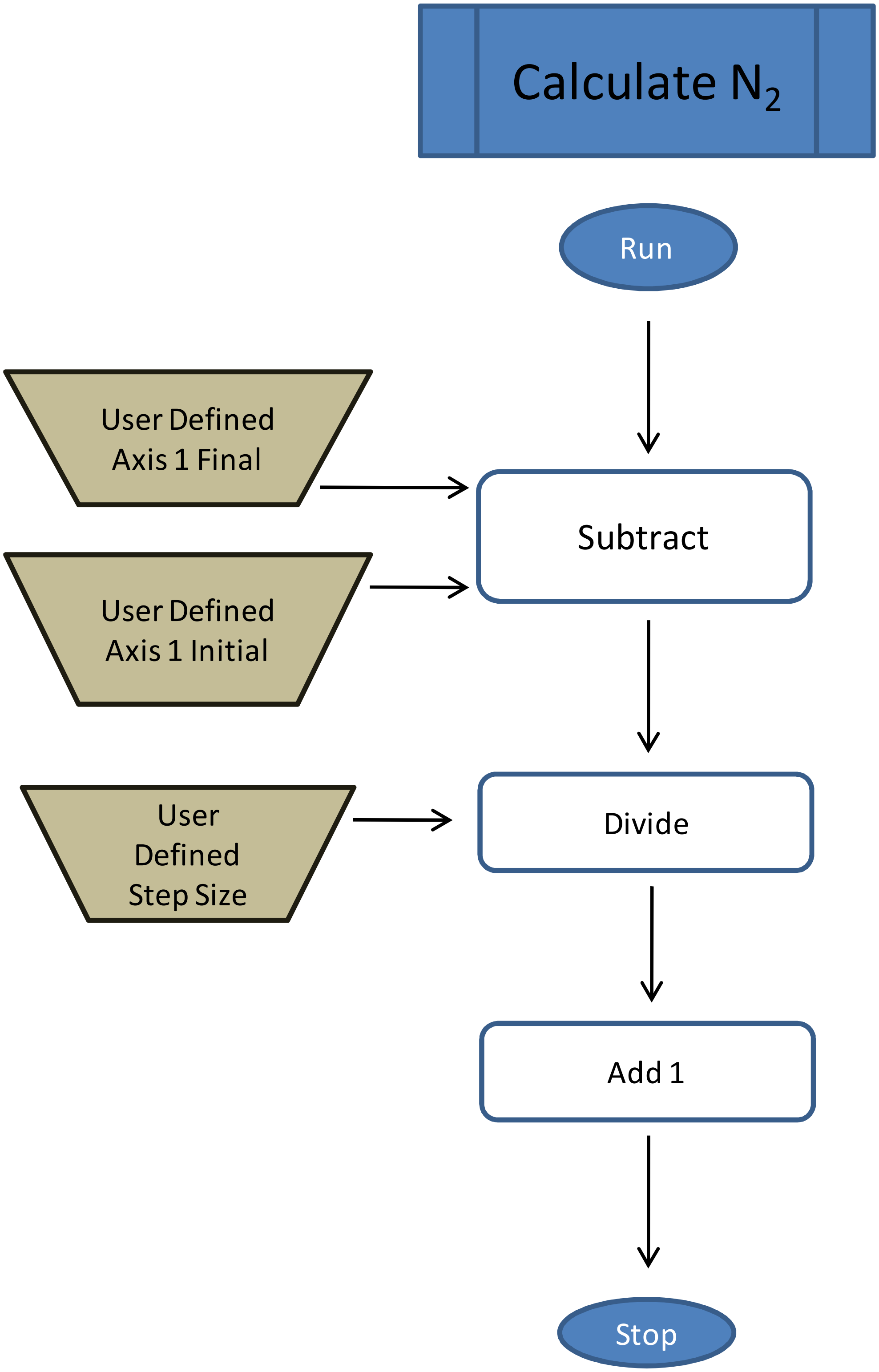
Calculate N_2
Run
User Defined Axis 1 Final
User Defined Axis 1 Initial
Subtract
User Defined Step Size
Divide
Add 1
Stop

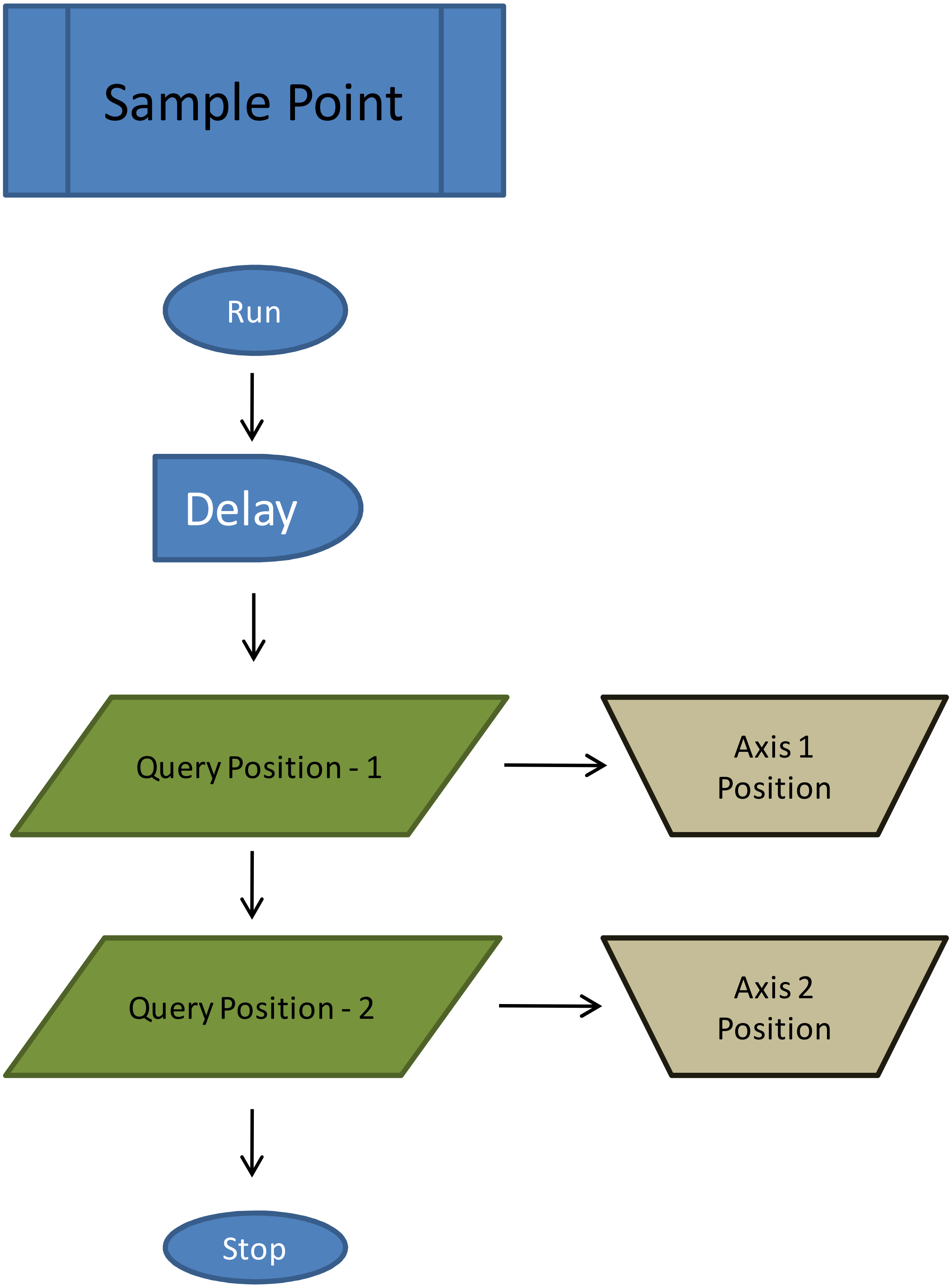
Sample Point
Run
Delay
Query Position - 1
Axis 1 Position
Query Position - 2
Axis 2 Position
Stop

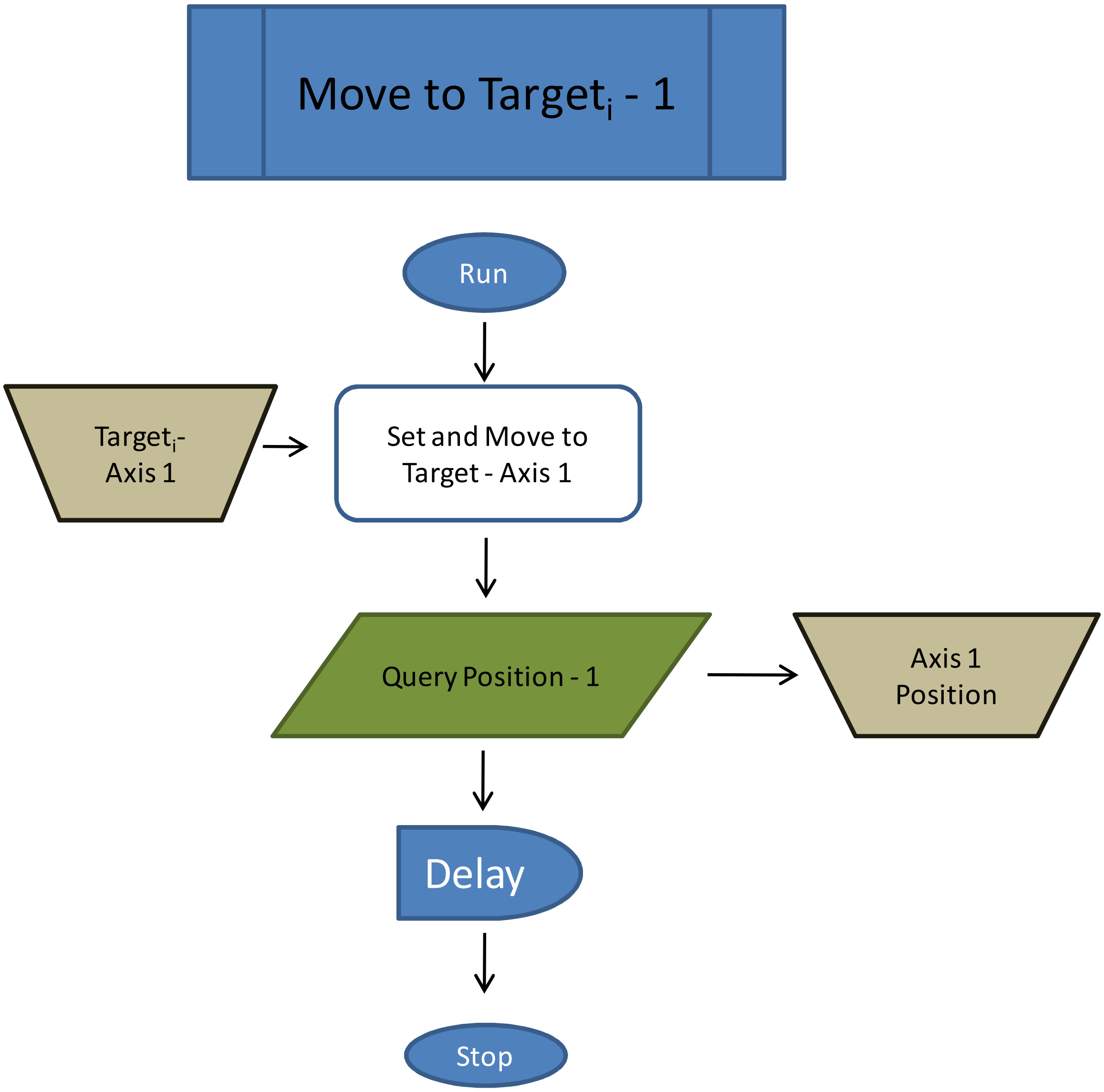
Move to Target$_i$ - 1
Run
Target$_i$-
Axis 1
Set and Move to
Target - Axis 1
Query Position - 1
Axis 1
Position
Delay
Stop

Move to Target$_i$ - 2

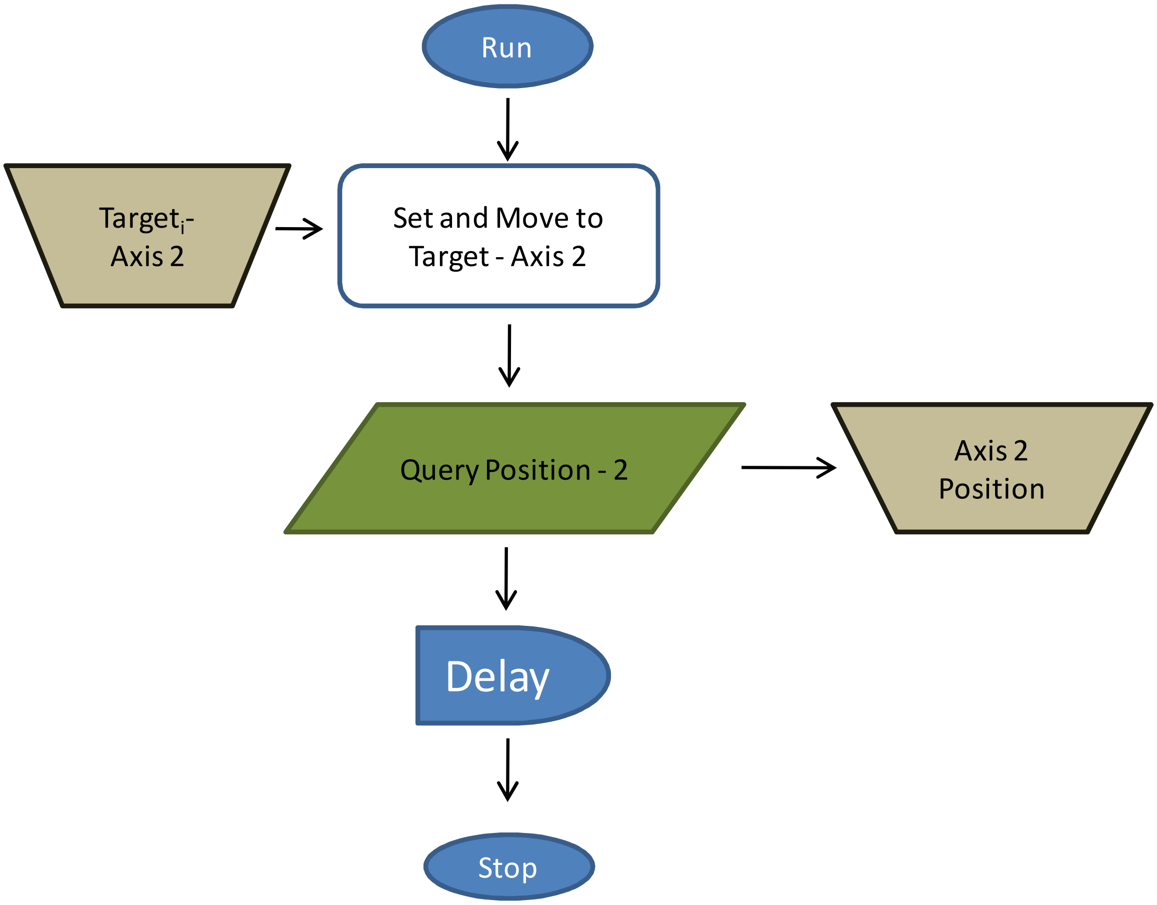
Run
Target$_i$- Axis 2
Set and Move to Target - Axis 2
Query Position - 2
Axis 2 Position
Delay
Stop

Move to Initial- 1,2

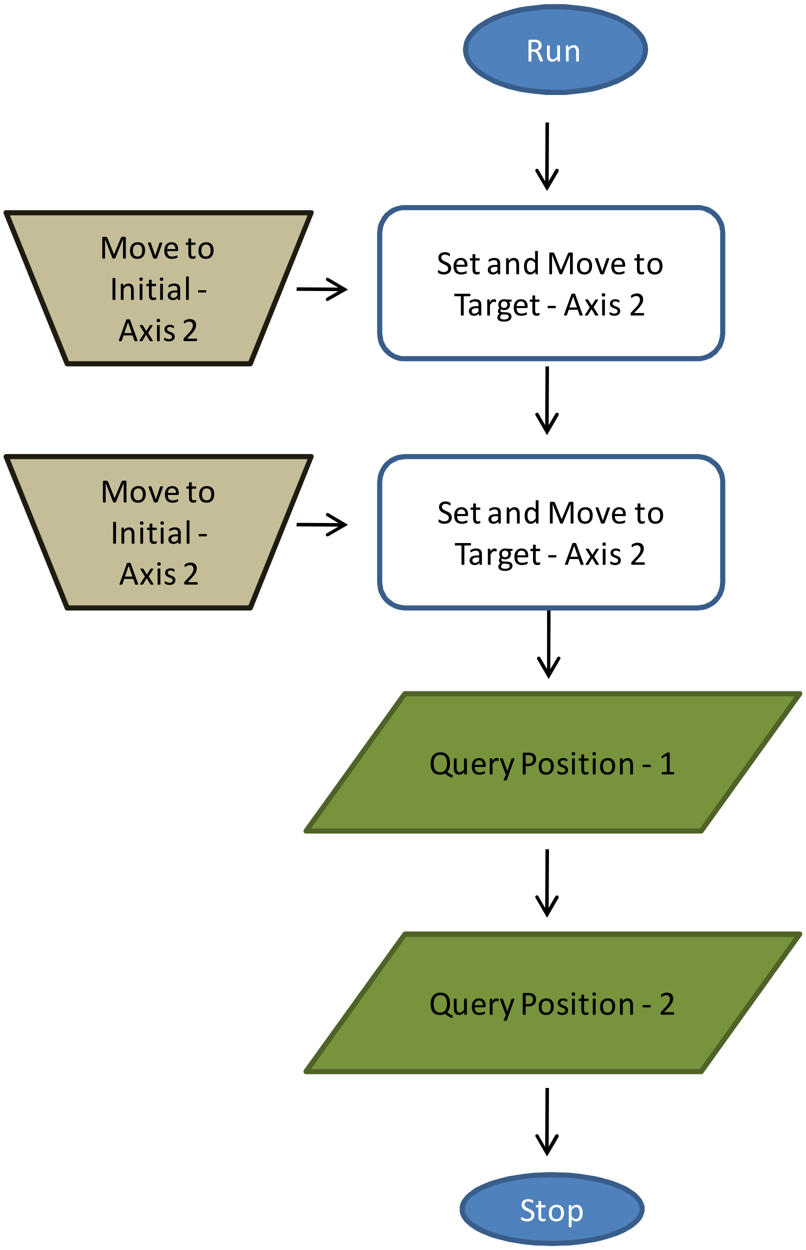
Run
Move to Initial - Axis 2
Set and Move to Target - Axis 2
Move to Initial - Axis 2
Set and Move to Target - Axis 2
Query Position - 1
Query Position - 2
Stop

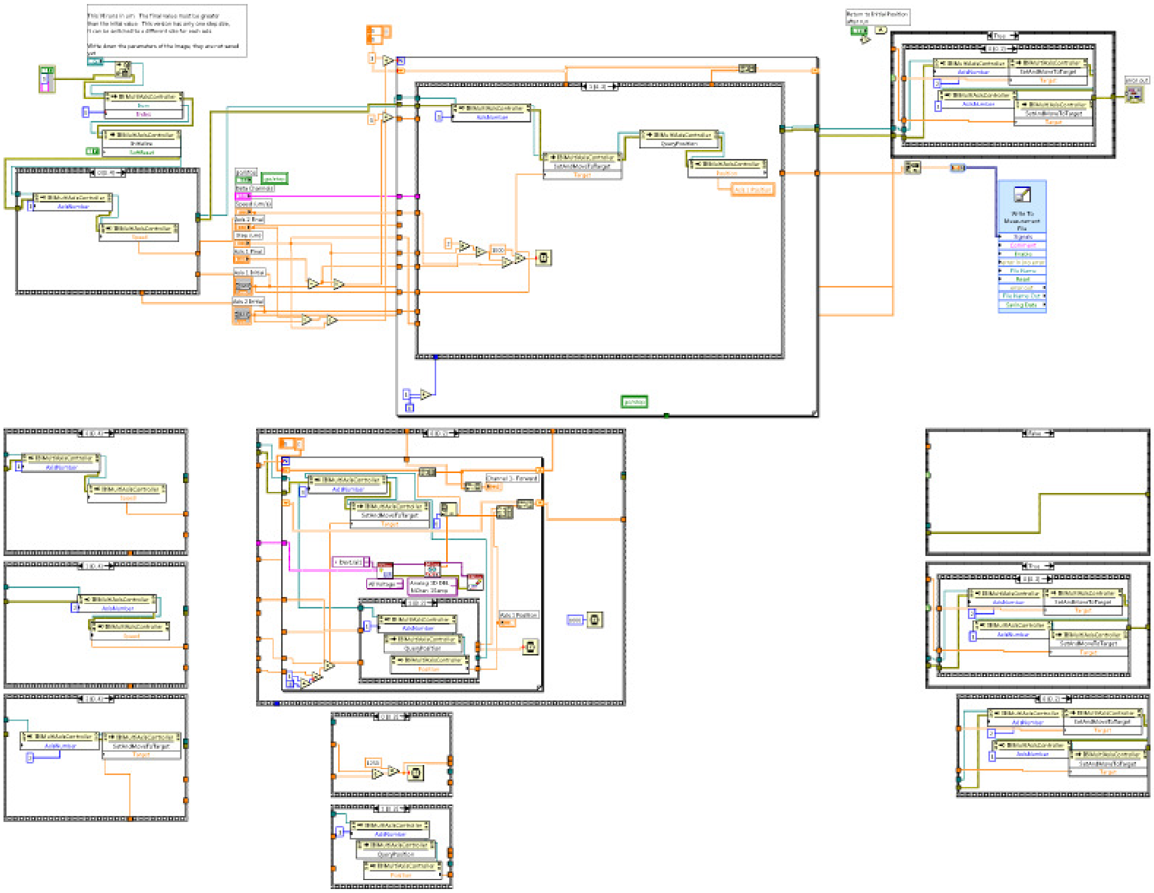
IBMultiAxisController
AxisNumber
SetAndMoveToTarget
Target
QueryPosition
Position
Speed
Axis 1 Position
Channel 1- Forward
Write To Measurement File
Signals

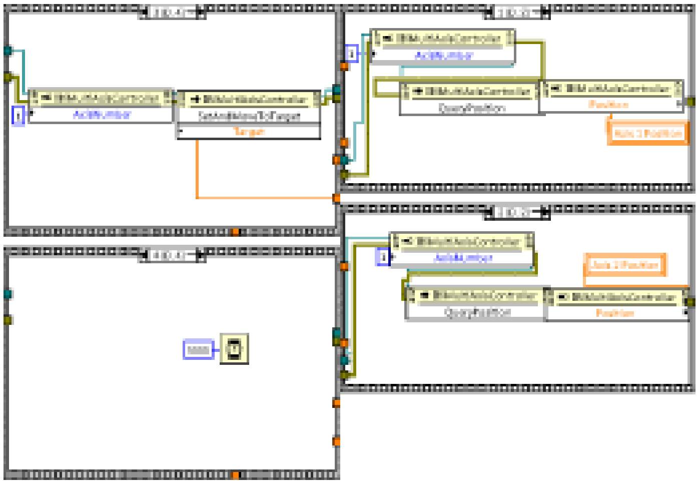
IBMultiAxisController
AxisNumber
SetAndMoveToTarget
Target
QueryPosition
Position
Axis 1 Position
Axis 2 Position

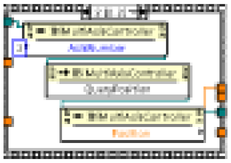
IBMultiAxisController
AxisNumber
IBMultiAxisController
QueryPosition
IBMultiAxisController
Position

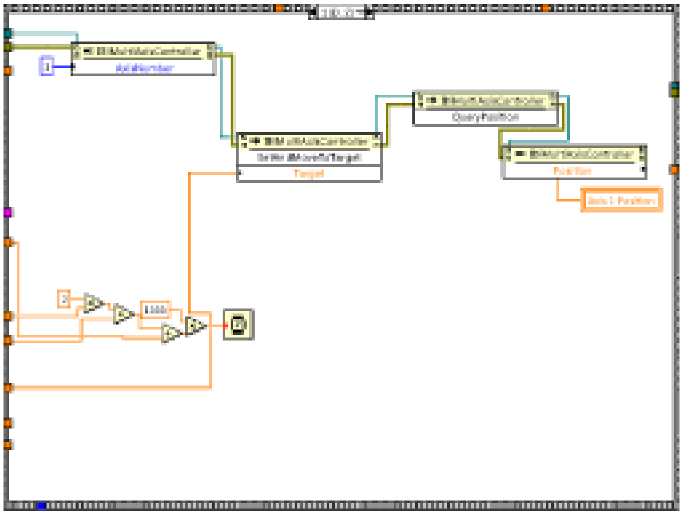
IBMultiAxisController
AxisNumber
IBMultiAxisController
Target
IBMultiAxisController
QueryPosition
IBMultiAxisController
Position
Axis 1 Position

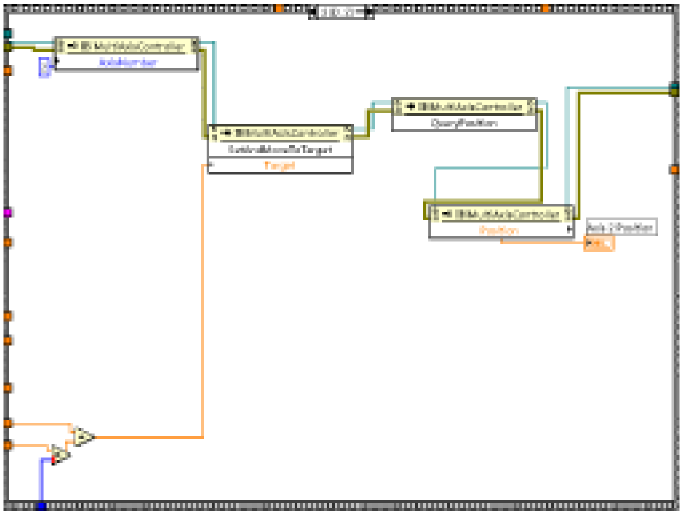
IBMultiAxisController
AxisNumber
IBMultiAxisController
Target
IBMultiAxisController
QueryPosition
IBMultiAxisController
Position
Axis 2 Position

4. CdSe nanocrystals

Synthesis of CdSe Nanocrystals. A multi-neck flask containing 43 g of TOPO and 500 µL of dimethyl cadmium was placed on a heating mantle with the temperature controller set to 360 ^oC. A thermocouple was inserted into a side joint with a Teflon Swagelock adapter and a septum onto the other side joint. The center joint contained a condenser holding dried ice. When the TOPO melted the coring solution, prepared of 1 g of selenium in 100 mL of TBP was rapidly injected into the multi-neck flask. The temperature of the solution immediately dropped and the thermocouple temperature was reset to 265 ^oC. The cores were than grown to the desired size, by adding the selenium in TBP coring solution. The progression of the reaction was observed by taking 1 mL aliquots and observing the wavelength of the peak in the ultraviolet-visible spectrum. An absorption peak at 555 nm correlates to a 3.2 nm crystal.[35] The TOPO solvent was removed by adding methanol. The mixture was centrifuged and the supernatant decanted. This procedure was repeated with octanol and then again with methanol to recover the nanocrystals.

CdSe Nanocrystal Synthesis and Characterization: Semiconductor nanocrystals will be used for the initial luminescence research. The size of the nanocrystal can be controlled by the initial reaction conditions, solution composition and growth time. The size of the nanocrystal is characterized by an ultraviolet-visible spectrum. In the figure below, the larger set of nanocrystals has an absorbance peak at a wavelength of 610 nm, while the smaller set peaks at a wavelength of 565 nanometers.

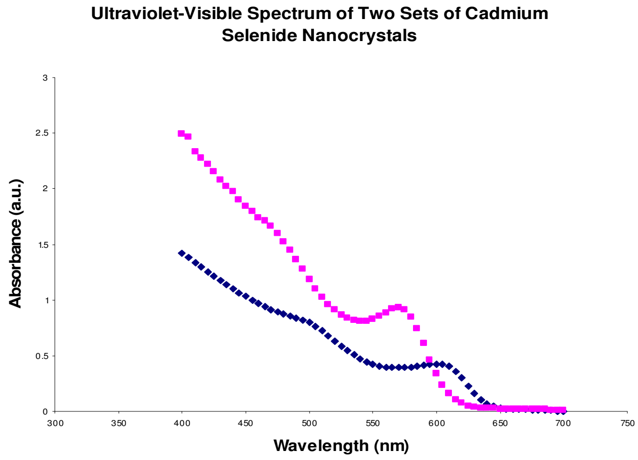

Ultraviolet – Visible spectrum of two different sets of synthesized nanocrystals.

5. Capillary Electrophoresis of Au-tiopronin MPCs

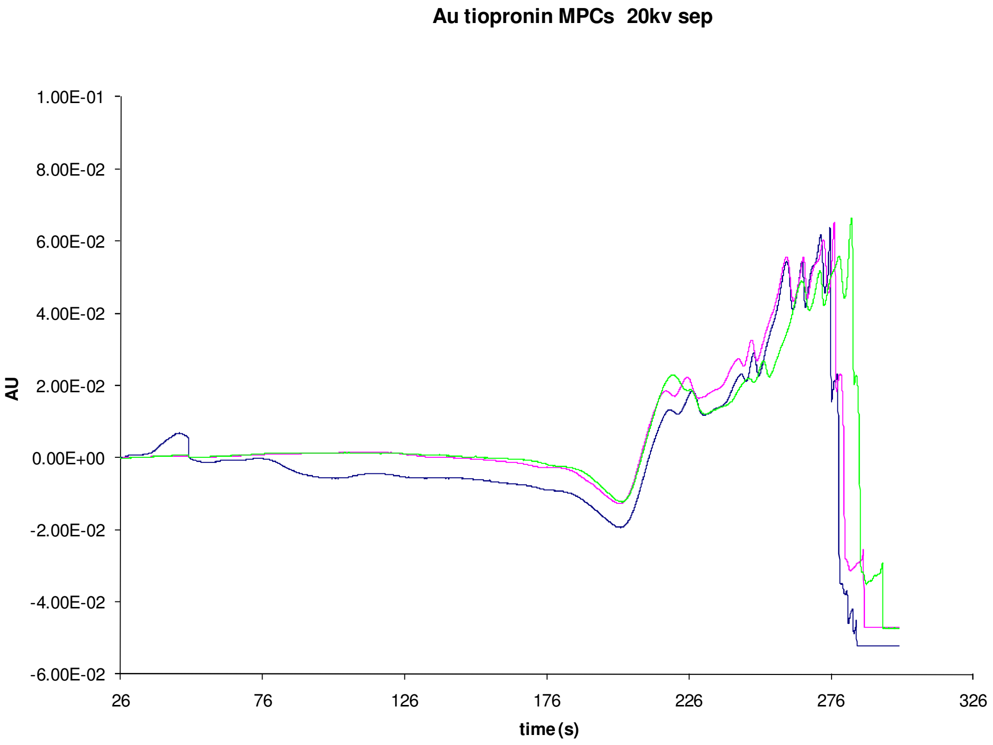

VITAE

Education

2002-Present Ph.D. Studies in Analytical Chemistry, Vanderbilt University, Nashville, TN (expected graduation date: May 2010)

1998-2000 M.S. in Physical Chemistry, University of California - Irvine

1994-1998 B.S. in Chemistry, State University of New York at Binghamton

Research and Work Experience

2002-present **Graduate Research Assistant with Prof. David E. Cliffel**
Vanderbilt University, Nashville, TN

- Received the Vanderbilt Institute of Nanoscience and Engineering Fellowship
- Performed the surface characterization of photoreduced platinum on oriented Photosystem I adsorbed onto self-assembled monolayers via atomic force microscopy and X-ray photoelectron spectroscopy with potential implications in catalysis and photovoltaics
- Characterized the respiratory syncytial virus (RSV) immunosensor by atomic force microscopy for the practical development of a rapid and cheap RSV immunosensor
- Designed, constructed and programmed in LabVIEW the computer interface for capillary electrophoresis lithographic instrumentation with applications in nanopatterning
- Programmed real-time 3D imaging software in LabVIEW for use as a scanning electrochemical microscope
- Synthesized CdSe nanoparticles in a drybox for use in photovoltaic devices to be manufactured by spincoating

2000-2001 **Research Assistant at Burstein Technologies**
Irvine, California

- Managed microscopy facilities, including the atomic force microscope and optical microscopes
- Developed assays for novel compact disk platform including surface modification and polymer adhesion to be used as blood diagnostic tests

1998-2000 **Graduate Research Assistant with Prof. Reginald M. Penner**

University of California - Irvine
- Electrodeposited metal clusters on the nanometer scale for use in nanoscale metal alloys
- Electrodeposited carbon fibers onto metal clusters as a platform for highly conductive materials

Publications

"Fundamentals", In *Handbook of Electrochemistry*; Zoski, C., Ed.; Ciobanu, M.; Wilburn, J.P.; Krim, M.L.; Cliffel, D.E. Elsevier: Amsterdam, 2007.

"Surface Characterization of Platinized Photosystem I Oriented and Bound to a Au-Modified Substrate", Krim, M.L.; Ciobanu, M.; Schmidt, B.W.; Faulkner, C.J.; and Cliffel D.E. (In preparation, to be submitted to *Thin Solid Films)*.

"Immunosensor Development for the Detection of Respiratory Syncytial Virus on the Quartz Crystal Microbalance Platform ", Zhang, Z.; Krim, M.L.; Bentzen, E. L.; Turner, B.; Cliffel, D.E. (In preparation, to be submitted to *Biosensors and Bioelectronics)*.

Presentations

“Plant Power: Electrochemical Energy Conversion Using Photosystem I” Cliffel D. E.; Ciobanu, M; Jennings G. K.; Xun, Y.; Krim, M. 234th ACS National Meeting, Boston, MA August 2007, Oral

"Platinization of Photosystem I Bound and Oriented", Krim, M.L.; Ciobanu, M.; Cliffel, D.E. 212th Meeting of The Electrochemical Society, Washington, D.C., October 2007, Poster.

"Capillary Electrophoresis Lithography", Krim, M.L.; Cliffel, D.E. 210th Meeting of The Electrochemical Society, Cancun, Mexico, November 2006, Oral.

"Capillary Electrophoresis Lithography", Krim, M.L.; Cliffel, D.E. 56th Meeting of Pittcon, Orlando, Florida 2006, Poster.

"Capillary Electrophoresis Lithography", Krim, M.L.; Cliffel, D.E. 55th Meeting of Pittcon, Orlando, Florida 2005, Poster.

"Capillary Electrophoresis of Monolayer Protected Clusters", Krim, M.L.; Cliffel, D.E. VINSE NanoDay, Nashville, TN, October, 2005, Poster.

"Scanning Capillary Electrophoresis Lithography", Krim, M.L.; Cliffel, D.E. VINSE Nano Forum, Nashville, TN, October, 2004, Poster.